Experimental and modeling studies of motor network excitability of neonatal rat spinal cord *in vitro*

Thesis submitted for the degree of "Doctor Philosophiae"

S.I.S.S.A. – Neurobiology Sector

Candidate:

Konstantin Ostroumov

Supervisor:

Prof. Andrea Nistri

Table of contents

Note

During my PhD years in S.I.S.S.A., I took part in the following studies:

Sharifullina E, **Ostroumov K**, Nistri A (2004). Activation of group I metabotropic glutamate receptors enhances efficacy of glutamatergic inputs to neonatal rat hypoglossal motoneurons in vitro. *Eur J Neurosci* **20**, 1245-1254.

Sharifullina E, **Ostroumov K**, Nistri A (2005). Metabotropic glutamate receptor activity induces a novel oscillatory pattern in neonatal rat hypoglossal motoneurones. *J Physiol* **563,** 139-159.

Nistri A, **Ostroumov K**, Sharifullina E, Taccola G (2006). Tuning and playing a motor rhythm: how metabotropic glutamate receptors orchestrate generation of motor patterns in the mammalian central nervous system. *J Physiol* **572,** 323-334.

Ostroumov K, Grandolfo M, Nistri A (2006). The effects induced by the sulphonylurea glibenclamide on the neonatal rat spinal cord indicate a novel mechanism to control neuronal excitability and inhibitory neurotransmission. (accepted to *Br J Pharmacol*).

All the work reported here arises solely from my own experiments, data analysis or modeling, unless otherwise stated. In particular, experiments concerning RT-PCR, Western-blot and Immunostaining were carried out by Dr. M. Grandolfo. Results published with Dr. Shariullina E., in which I am co-author, are not presented in this thesis.

Acknowledgements

I would like to deeply thank Prof. Andrea Nistri for his careful supervision and mentoring during all these years. His dedication to neuroscience and trust in me were fundamental for my work in this field. I would like to thank Dr. Micaela Grandolfo for her work with me. I would also like to thank Dr. Giuliano Taccola for his teaching from the very beginning. My gratitude goes to my teachers from whom I have learned many things, which are not possible simply to list. I would like to thank Dr. Elina Sharifullina just for being close and patience. Thank you to all my family and friends for support and concern, which make my work and live much more pleasant and meaningful.

Abstract

The present study has investigated certain mechanisms that control network excitability in the neonatal rat spinal cord *in vitro*, by means of intracellular recordings from single motoneurons, extracellular recordings from ventral roots, whole-cell clamp recordings from interneurons and modeling of electrical behavior of single motoneurons.

Sulphonylurea drugs have been used to investigate the role of ATP sensitive K^+ channels (K_{ATP}) in controlling the excitability of central neurons (Crepel *et al.*, 1993; Mironov *et al.*, 1998). In certain brain areas, which possess intrinsic electrical rhythmicity like the brainstem respiratory centers and associated nuclei, K_{ATP} channels pace the frequency of bursting and the duration of single bursts (Pierrefiche *et al.*, 1996; Sharifullina *et al.*, 2005). Because this mechanism relies on cyclic intracellular consumption and neosynthesis of ATP, it represents a powerful process to link neuronal electrical discharges to metabolic activity.

In the spinal cord, inherent rhythmicity can be readily observed in locomotor networks which express a stable pattern of regular electrical discharges (Kiehn & Butt, 2003). Since we have previously shown that the ATP-dependent Na^+-K^+ pump is a major controller of spinal network bursting (Rozzo *et al.*, 2002), we wondered whether periodic changes in intracellular ATP might control the activity of K_{ATP} conductances and thus limit neuronal excitability. One simple functional test for this possibility was to apply a K_{ATP} channel blocker like glibenclamide (Bryan *et al.*, 2004) and to monitor resultant changes in network responses. This approach soon led us to unexpected results, which raised the issue of a novel mechanism to control spinal network excitability. Because sulphanylurea drugs are also efficient blockers of cystic fibrosis transmembrane conductance regulator (CFTR), a membrane protein involved in Cl^- transport, it seemed interesting to explore the hypothesis that the neonatal rat spinal cord could express this proteins whose function might be expected to regulate Cl^- dependent transmission operated by GABA and glycine. Application of glibenclamide (or tolbutamide), or the CFTR inhibitors (DPC or thiazolidinone $CFTR_{inh}$-172) led to membrane potential hyperpolarization, input resistance increase and larger spike overshoot. These data were accompanied by a negative shift in the reversal potential of the GABA and glycine mediated effects. RT-PCR analysis and Western blotting showed CFTR

gene function and protein expression in support of a functional role of CFTR to control Cl^- homeostasis and neuronal excitability. Indeed, glibenclamide affected generation of spinal reflexes and rhythmic bursting. The present data allow us to formulate a new basis for the role of GABA and glycine as inhibitory neurotransmitters at an early postnatal stage of development.

The effects of CFTR channel blockers were further examined by means of modeling the electrical behavior of motoneurons. To this end a 3D structure of motoneurons was simulated using a stochastic algorithm the design which was based on known morphological parameters. Discrete surface distribution of voltage-sensitive ion channels and passive membrane changes enabled simulation of experimental findings. The model suggested a somatic localization of CFTR channels providing hypothetical possibility of colocalization with GABA/glycine receptors and thus regulation of their functionality by Cl^- homeostasis regulation.

Introduction

The list of the brain areas containing neuronal networks involved in the motor activity is quite vast and includes the brain stem, motor cortex, cerebellum and basal ganglia. The description of these areas and their role in control or generation of motor patterns is reviewed in the specialized textbooks (Kandel *et al.*, 2000; Martin *et al.*, 2001; Mori *et al.*, 2004).

The present study focused on the investigation of spinal circuits involved in the generation of motor activity. Thus, this introduction deals with spinal motoneurons which were at first termed "final common pathway" (Sherrington, 1906; Clarac, 2005b), spinal networks responsible for hard-wired reflexes (Fitzgerald, 1985; Kudo & Yamada, 1987) and the spinal central pattern generator (CPG) and its excitatory networks which can (independently from higher centres and sensory feedbacks) coordinate motor outputs (Butt *et al.*, 2002; Kiehn & Butt, 2003; Clarac *et al.*, 2004; Kiehn, 2006).

1. Anatomical overview of the spinal cord

1.1 Organization of the neonatal rat spinal cord

The spinal cord is divided into spinal cord segments from which pairs (right and left) of spinal nerves emerge. The segments are organized into four regions named after the surrounding vertebrae: cervical (seven bones, eight segments), thoracic (twelve bones, thirteen segments), lumbar (six vertebrae, six segments) and sacral (one bone, four segments). The cervical bones are designed to allow flexion, extension, bending and turning of the head, while cervical spinal segments receive sensory information from the neck, shoulders or forelimbs and innervate these regions. The motion that occurs in the thoracic spine is mostly rotation; thoracic segments supply muscles of the chest and back that help in breathing and posture supply. The main motions of the lumbar area are bending forward or to the side and extending backwards; the lumbosacral spinal cord innervates hindlimbs and tail receiving sensations from the hindlimbs, tail and lower abdomen. Spinal segments and spinal nerves are routinely identified by their region, e.g., 5th lumbar (L_5) spinal segment.

In quadrupeds and bipeds, hindlimbs are mostly used in relatively stereotyped motor patterns such as walking, locomotion, galloping, while forelimbs participate in a wide range of voluntary tasks which are supported by a more complex organization of innervating networks and are under the influence of a direct cortical-motoneuronal system (review Dietz, 2002). This fact provides the reason why the lumbar spinal cord is preferred to the study of stereotyped motor patters and reflexes (see also Shik & Orlovsky, 1976). In the following sections I briefly introduce the lumbar spinal cord organization and function.

1.2 Laminar (cytoarchitectonic) organization of the rat spinal cord

A cross section of the spinal cord reveals outer and inner parts of the spinal cord. Under light microscope, the more dense inner part (gray matter) sharply contrasts with the outer one (white matter). The outer part contains ascending and descending tracts that run parallel along the longitudinal direction of the cord. The gray matter has a butterfly-like appearance, with the two dorsal horns, an intermediate region and two ventral horns and is mostly filled up by neurons, glia and neuropile.

The cytoarchitectonic laminar scheme of the cat spinal cord gray matter proposed by Rexed (1952) is a common reference map to identify topography in spinal cord coronal sections for anatomists (Mirnics K & Koerber HR, 1995b; Rivero-Melian, 1996) and physiologists (Fitzgerald *et al.*, 1991; Kjaerulff *et al.*, 1994; Levinsson *et al.*, 2002; Kiehn & Butt, 2003). Molander and colleagues (1984) examined the applicability of Rexed's principles to the description of the lower thoracic and lumborsacral segments of the neonatal and adult rat spinal cord. The cytoarchitectonic organization of the rat spinal cord was found to be basically similar to that of the cat. Moreover, the laminar organization of the newborn rat spinal cord differs from the adult one simply by less distinct borderlines between laminae, especially in the superficial dorsal horn. Figure 1 shows the laminar cytoarchitectonic scheme of the L_5 rat spinal cord segment. It should be emphasized, however, that, in practice, borders are not as distinct in an individual section as might be concluded from this figure.

Figure 1. *Laminar (cytoarchitectonic) organization of the rat spinal cord (modified from Molander et al., 1984)*

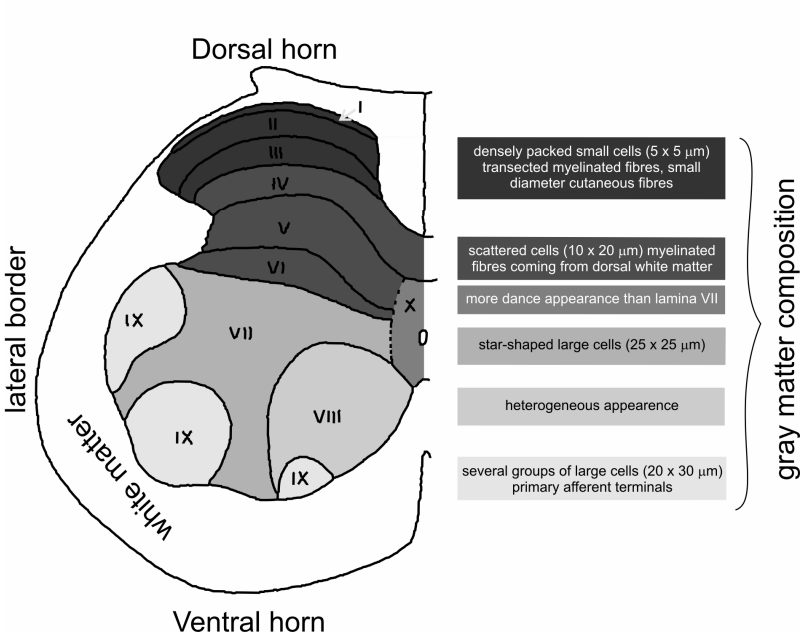

1.3 Spinal motoneuron development up to the second postnatal week

In the lumbar region of the rat spinal cord during neurogenesis, motoneurons are the earliest neurons to appear as they can be detected on day 12 of gestation (E12) and, by E14, a few of them are already clustered. The whole process of neurogenesis in the lumbar region takes 5 days (from E11 to E16; Nornes & Das, 1972; 1974). Like in other areas of the brain, embryogenesis is a dynamic process comprising concurrent neuro-genesis and neuro-degeneration within the same region. Significant loss of motoneurons occurs between E15 and the first postnatal day (P1), after which no further loss is observed (Oppenheim, 1986; for review Oppenheim, 1991). Hence, at birth, the newborn rat has virtually a fully developed spatial distribution of motoneurons throughout the lumbar segments of the spinal cord, though motoneurons are subjected to further developmental pruning and evolution.

Although earlier studies indicate that motoneurons innervating fast motor units and slow motor units (see below) differ in size and complexity (Lüscher & Clamann, 1992; Westbury, 1982), there is little information about the developmental stage

when morphological differences became clearly visible. Likewise, most studies on the neonatal rats have considered motoneurons as a homogeneous population, or have focused on motoneurons specifically innervating one group of the muscles. For instance, histological changes within the tibialis anterior motoneuron pool (between P8 and P30) were studied by Westerga and Gramsbergen (1992), and postnatal (P1-9) changes in the somatodendritic morphology of rat ankle flexor motoneurons have been investigated by Dekkers *et al.* (1994). Important conclusions are that, at P7, most of the growth-associated appendages (filopodias) disappear from the soma and proximal dendrites, and the soma size distribution of motoneurons remains largely unimodal until P20 (the arborization pattern of dendrites of tibialis anterior motoneurons is basically multipolar). The major differences between these motoneurons are the bimodal distribution of soma sizes at P20, and the elongation of dendritic trees to the longitudinal bundles after P16. Thus, during the first two postnatal weeks, it is not possible to morphologically distinguish morphologically various classes of motoneuron. Motoneurons innervating rat hindlimb extensor muscles are usually less mature at birth than flexor one in terms of their electrical properties (Vinay *et al*., 2000).

1.4 Motoneuronal pools

Knowledge of the origin and distribution of the motor supply to a muscle is of particular importance not just in order to conduct electrophysiological experiments, but also to understand the organization of spinal reflexes and motion. The spatial distribution of motoneurons innervating hindlimbs throughout the lumbar segments of the rat spinal cord has been studied extensively by using retrograde transport of horseradish peroxidase (HRP) or fluorescent dyes (Nicolopoulos-Stournaras & Iles, 1983; Peyronnard & Charron, 1983; Crockett *et al*., 1987; Kerai *et al*., 1995; Kobbert C & Thanos S, 2000). Because this distribution in the lumbar region appears to be finalized in a few days after birth (see above), data obtained from the adult species can be applied to neonates. The motor neurons supplying a single muscle are somatotopically organized in a discrete longitudinal column in the lateral or intermediate ventral horn. The columns extend through up to three adjacent segments and their longitudinal location varies by as much as one segment

in different animals. The stereotaxic map has been constructed by Nicolopoulos-Stournaras & Iles (1983).

1.5 Motor units

The efferent fibres, formed by the axons of the spinal motoneurons, leave the spinal cord through ventral roots (VR) to control particular muscle groups. First signs of axonal outgrowths can be detected as early as E13-14 (Nornes & Das, 1972) and end-plate potentials can be recorded in some myotubes at E14 (Dennis *et al.*, 1981). The number of inputs per myofiber increases until E18, and then begins to decline before birth, reaching its adult value of one input per myofiber within the second postnatal week (Dennis *et al.*, 1981). Peyronnard and Charron (1983) indicate that the number of myelinated fibres and motoneurons supplying L_4 ventral roots in the adult rat is equal to 1842 and 1568, respectively. The difference between these two numbers reflects staining techniques error (Nicolopoulos-Stournaras & Iles, 1983).
Motor axons seldom branch on their way to muscle (except central axonal branches that make contacts on Renshaw cells and other motoneurons), and therefore innervate only one muscle. However, they do branch numerous times intramuscularly to innervate tens to hundreds of muscle fibers. The combination of a motoneuron plus all of the muscle fibers it innervates is called a motor unit (Sanes & Lichtman, 1999).
In adult vertabrates, two different types of skeletal muscle exist, slowly contracting twitch muscles and more rapidly contracting fast muscles. The set of muscle fibers innervated by any single motoneuron are of the same type. Thus, by activating certain motoneurons, it is possible to generate agonist and antagonist actions for different motor tasks. Figure 2 classifies different types of motoneurons by the type of motor units they constitute (Clarac, 2005b). The description of selective innervation of fibres in developing rat muscles has changed numerous times during last few decades. Multiple molecular pathways (for review see Thompson et al. 1987; Glover, 2000; Jessell, 2000; Koo & Plaff, 2002; Pricea & Briscoe, 2004) together with functional interaction between motor axons and muscles (for review see Koo & Plaff, 2002) regulate the development and organization of the motor supply.

1.6 Afferent nerves and afferent projections to the rat spinal cord

Each spinal nerve is connected to the spinal cord by means of dorsal (DR) and ventral (see above) roots. DRs are composed of afferent fibres and deliver mechano, thermal and noxious information into the spinal cord and higher brain regions. The dorsal afferents originated from the dorsal root ganglia (DRG). The central DRG projections grow into the thoracic and lumbar cord starting from E15-E17 (Fitzgerald *et al.*, 1991; Mirnics K & Koerber HR, 1995b). Large diameter fibres enter the cord first; non-myelinated small diameter fibres appear in the cord later, around the time of birth (E19-21) (Snider *et al.*, 1992; Fitzgerald & Jennings, 1999; Mirnics K & Koerber HR, 1995b). Because the peripheral nerves are relatively slow in myelinating the afferent input volley increases in conduction velocity over the early postnatal week. Two waves of input volleys are clearly visible even at birth (Fitzgerald, 1985). The peripheral nerve endings (peripheral DRG projections) reach the hindlimbs and make contacts in the skin from E13 onward (Mirnics K & Koerber HR, 1995a).

The afferent and efferent fibres are usually classified on the basis of fibre diameter and conduction velocity. The Roman numeral classification system (Table 1 top) is used for afferent fibres, while the letter system combines both efferent and afferent fibres (Table 1 bottom).

In terms of sensory information provided to the dorsal horn, projections were reviewed by Light (1988) who concluded that the dorsal horn receives integrated afferent inputs from innocuous primary afferents and information is then relayed primarily by neurons in laminae III-VI. These neurons project to the medulla and the cervical spinal cord. Nociceptive input is integrated and relayed by neurons in laminae I, II and V which project to the reticular formation and thalamus. However, it should be noted that in the adult Aβ afferents are restricted to laminae III and IV but in the neonate their terminals extend dorsally right up into laminae I and II (Snider *et al.*, 1992; Fitzgerald *et al.*, 1994; Fitzgerald & Jennings, 1999). This neonatal pattern is followed by a gradual withdrawal from the superficial laminae over the first three weeks (Fitzgerald *et al.*, 1994). Moreover, by labelling sensory axons with different lipid-soluble tracers, it was found that the somatotopic organization of the cutaneous afferent projection, which remains confined to the dorsal horn, is already present at the time DR axons first penetrate into the gray matter (Silos-Santiago *et al.*, 1995).

Figure 2*. Different types of motoneurons and their respective role*

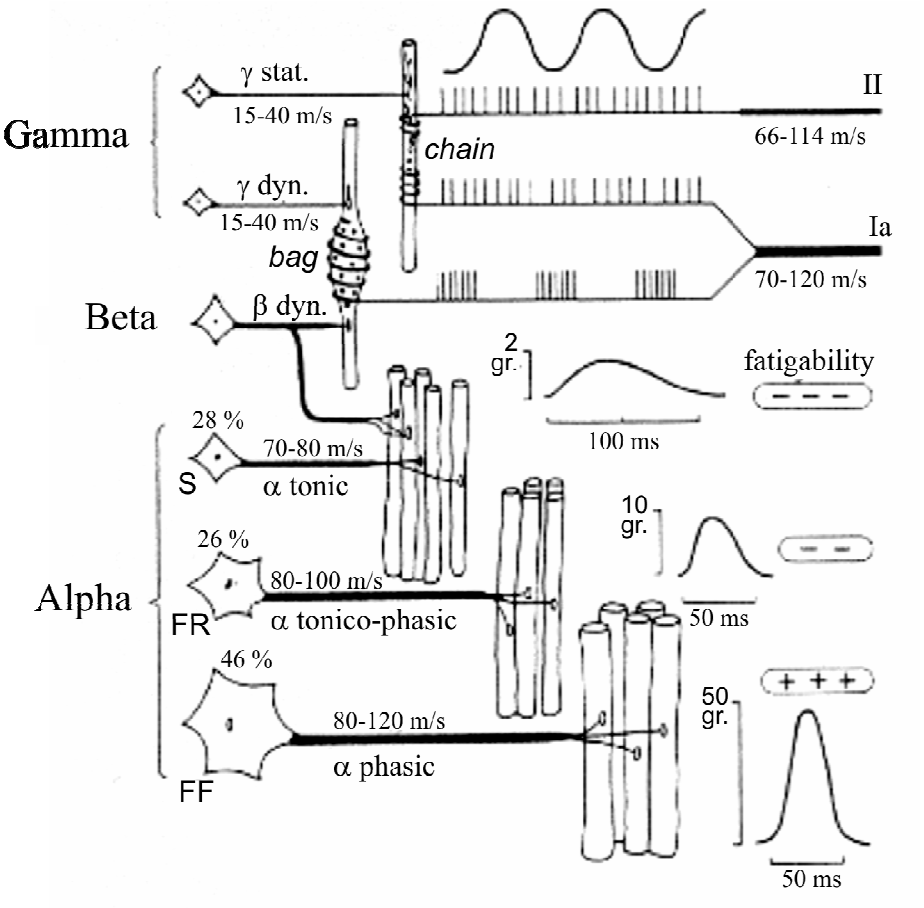

The alpha motoneurons constitute different types of motor units with slow fibres (S), fast fatigue-resistant (FR) and fast fatigue fibres (FF). In the muscle spindles, the static gamma motoneurons stimulate the chain fibres and the dynamic gamma motoneurons stimulate the bag fibres (modified from Clarac, 2005b).

Table 1*. Roman numerical classification system for afferent fibres (modified from Mann, 2006)*

type of fibre	*diameter, µm*	*myelination*	*conduction velocity, m/s*	*general function*
Ia	12–20	yes	70–120	muscle spindle primary endings
Ib	11–19	yes	66–114	Golgi tendon organs
II	5–12	yes	20–50	touch, kinesthesia, muscle spindle secondary endings
III	1–5	yes	4–20	pain, crude touch, pressure, temperature
IV	0.1–2	no	0.2–3	pain, pressure, touch,temperature

Letter classification system for afferent and efferent fibres

type of fibre	*diameter, µm*	*myelination*	*conduction velocity, m/s*	*general function*
A-α	13–22	yes	70–120	alpha-motoneurons, muscle spindle primary endings, Golgi tendon organs, touch
A-β	8–13	yes	40–70	touch, kinesthesia, muscle spindle secondary endings
A-γ	4–8	yes	15–40	touch, pressure, gamma-motoneurons
A-δ	1–4	yes	5–15	pain, crude touch, pressure, temperature
B	1–3	yes	3–14	preganglionic autonomic
C	0.1–1	no	0.2–2	pain, touch, pressure, temperature, postganglionic autonomic

The projections into the lamina IX cell groups are characterized by somatotopic organization, even though an overlap exists. The densest primary afferent projection from each projecting nerve is to its homonymous motoneurons in adult

rats (Rivero-Melian, 1996). The development of the interaction between muscle spindle afferents (Ia fibers) and their target motoneurons was studied in details by Snider and collaborators (1992) for the cervical and lumbar spinal segments. Surprisingly, it was found that, although, dendrites from motor pools innervating limb muscles project in the path of incoming Ia afferents, they do not guide afferents to appropriate motor pools. The Ia afferents pass over the distal dendrites and grow all the way to the border between gray and developing white matter. A significant amount of terminal branching and bouton formation is in the vicinity of motoneuron's somata and proximal regions of the dendritic arbors. Few boutons are found near dendrites that project dorsal to the motor pools. It should be mentioned, however, that at the time Ia afferents reach the grey matter and initially intersect the dendrites (E17) of motoneurons (without contacting them), the most distal dendrites can be already found as far as the intermediate zone of L_5 (laminae V-VI; Snider *et al.*, 1992). The time for the beginning of the dense branching and bouton formation in the area of the motor pools is between E17.5-E19.5 (Kudo & Yamada, 1987).

1.7 Renshaw cells

Perhaps, one of the most studied cell types in the spinal cord after motoneurons is the Renshaw cell (see review by Hultborn, 2006). There are two reasons for this fact: firstly, Renshaw cells remain one of the few examples in the CNS where nicotinic AChRs are known to underlie rapid synaptic transmission (Dourado & Sargent, 2002); secondly, these cells probably control the output of the motor output stage (Hultborn, 2006). Renshaw cells are found in the most mediolateral region of the ventral horn (lamina VII; Alvarez *et al.*, 1999); where they receive a high density of relatively large cholinergic inputs presumably from central axonal branches of motoneurons. The majority of inputs from motoneurons are distributed over distal dendrites (Alvarez *et al.*, 1999).

Recent studies (Mentis *et al.*, 2005; Nishimaru *et al.*, 2005) revealed new mechanisms in the control of the Renshaw cells: motoneurons, in addition to acetylcholine, release glutamate that activates NMDA and AMPA/kainate receptors on Renshaw cells.

***Figure 3**. Recurrent inhibition modulates the input-output relationship of motoneurons*

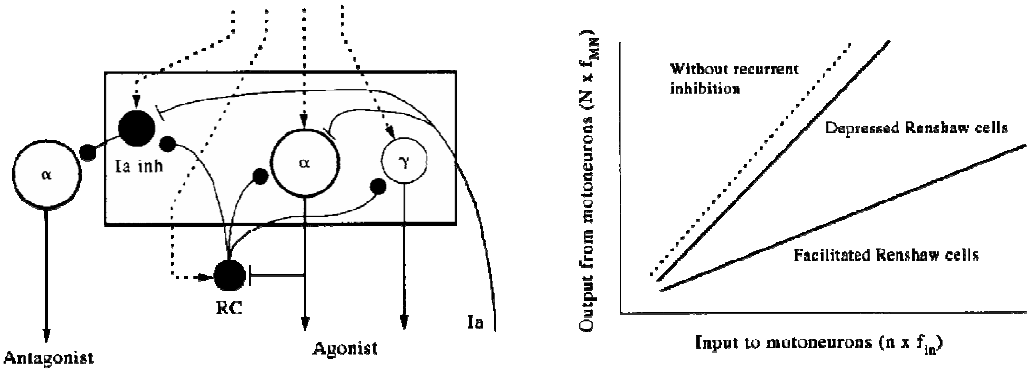

On the left, superimposed rectangle encased elements which constitute 'motor output stage' operating as a functional unit due to common activity patterns effected by the same inputs (dashed lines). α- and γ-motoneurons innervate an agonist muscle and α-motoneuron alone innervates Renshaw cell (RC). Reciprocal ('corresponding') Ia inhibitory interneurons ($I_{a\ inh}$) receive group Ia afferent input from that muscle (or close synergist) and inhibit antagonist motoneurons. RC inhibits all the cells in the 'motor output stage' in order not to disturb balance of activity when changing their sensitivity in response to modulating inputs. On the right, scheme illustrates the effects of changing recurrent inhibition on the input-output relationship of the motoneurons. The motor output is described roughly as a product of the number of active motoneurons, N, and their average firing rate, f_{MN}. Similarly, the excitatory synaptic input to the motor pool is the product of number of active presynaptic fibres, n, and their average firing rate, f_{in} (modified from Windhorst, 1996).

In turn, the Renshaw cells monosynaptically inhibit motoneurons, in a strychnine and bicuculline-sensitive manner (Marchetti *et al.*, 2002; Hultborn, 2006). In cats it was shown that this "recurrent inhibition" is stronger between motor nuclei innervating close synergists and it is especially prominent inside the homonymous motor nucleus. The recurrent inhibition was never seen between motor nuclei innervating direct antagonists (review Hultborn, 2006; see Figure 3).

1.8 Commissural interneurons

Another important subgroup of spinal neurons is the broad family of commissural interneurons (CIN). Their presence and correct wiring is important for generation of rhythmic activity and left-right coordination in the spinal cord (see below; for review Butt *et al.*, 2002; Kiehn & Butt, 2003; Kullander *et al.*, 2003; Kiehn, 2006). CINs are traditionally classified according to localization and morphology in the rat spinal cord (Silos-Santiago & Snider, 1992; Silos-Santiago & Snider, 1994; Butt *et al.*, 2002).

Embryonic development of CINs in the thoracic rat spinal cord has been studied by Silos-Santiago and Snider (1992) using lipid-soluble fluorescent dye labeling. This study revealed a large number (18 different types at E19) of classes of CIN within the dorsal horn, intermediate zone and ventral horn of the embryonic rat spinal cord. By E15, commissural cells are near their final location and exhibit characteristic morphology. The number of primary dendrites is set at this age and further growth occurs by elongation and branching of existing dendrites. An interesting feature in the organization of CINs is their tendency to form small clusters at an early stage of development; the significance of this clustering is, however, unclear.

Kiehn and collaborators have used morphological principles to characterize CINs in the lumbar spinal cord. Their classification is based on the direction of axonal projections to the contralateral hemicord (Eide *et al.*, 1999; Tran & Phelps, 2000; reviewed by Butt *et al.*, 2002). Like the thoracic CINs, lumbar CINs are clustered in groups located in the dorsal, intermediate or ventromedial zones of the spinal cord. However, in the lumbar cord this organization can be explained on the basis of the direction of axonal projections. CINs with ascending (aCINs) and CINs with descending (dCINs) axons occupy different but overlapping domains within the transverse plane. The aCINs are clustered into four recognizable groups, while the dCINs are clustered into two recognizable groups (Eide *et al.*, 1999). These long range projection interneurons send their axons up to seven spinal segments in both rostral (aCINs) and caudal (dCINs) directions. Bifurcating (adCINs; 17 % of all CINs) and short projecting (sCIN; 20 % of all CINs) subpopulations are also present in the lumbar spinal cord (Butt *et al.*, 2002).

A study of the synaptic targets of commissural interneurons by Birinyi and colleagues (2003) shows that commissural interneurons may establish monosynaptic contacts with motoneurons on the opposite side of the spinal cord. Furthermore, direct reciprocal connections between commissural interneurons on the two sides of the spinal cord may also exist.

1.9 Summary of the spinal cord organization

The anatomical organization of the lumbar spinal region should be considered as the basic material for understanding such topics like spinal reflexes and locomotion.

The present introduction has deliberately left out long-projection neurons and descending tracts because the signals they relay are concerned with modulation and control of movements from higher centres.

Summarizing the morphological organization of the spinal cord it can be concluded that: 1, lumbar spinal circuits are in most cases subjected to quite precise somatotopic organization; 2, external sensory afferents provide massive inputs to all spinal laminae; 3, motor efferents are organized into functional groups; 4, complex wiring of intraspinal circuits can provide whole range of left-right, intra- and inter-segmental modulations as indicated by the function of CINs and Renshaw cells; 5, all this knowledge is extremely important but makes sense only if morphological data are integrated into the range of physiologically important behaviors, such as reflexes and locomotion.

2. Spinal reflexes. Development in rats

The spinal reflexes have been regarded as one of the most fundamental neural mechanisms for at least four centuries starting from Descartes and Willis. Their role in the development of psychology, physiology and neuroscience is hard to be overestimated. Apparent simple organization, reproducibility and popular principle of stimulus-response reactions laid the foundations for the most influential past behaviouristic theories. These theories rejected all non-measurable explanations of behaviour and replaced voluntary movements with operants: conscious arbitrary acts which have became associated with arbitrary stimuli through learning and arbitrary reinforcement (Prochazka *et al*., 2000; Clarac, 2005a, b). However, despite so many years of studies of reflexes, there is still no commonly recognized definition of them (Prochazka *et al*., 2000). In the past spinal reflexes were thought to be "hard-wired". Using a few simple examples of spinal reflexes, I will try to link anatomical structures to functional activity and describe input-output circuits of a particular kind. Nevertheless these circuits remain context-dependent, phase-dependent as well as multifunctional, and therefore they are not hard-wired.

2.1 Stretch reflex and monosynaptic reflexes

The stretch reflex (also called the "myotatic reflex") is the simplest spinal reflex. An example of which is the tendon jerk reflex or tendon tap reflex. This is the reflex elicited by tapping the tendon just below the knee. Sherrington and Liddell described the myotatic reflex in 1924 and 1925 in a decerebrate cat. When the knee extensor muscle (quadriceps) was suddenly lengthened, they observed a great increase in the muscle force developing after a very short latency. When the muscle nerve was cut, a similar stretching movement induced only a residual force due to elastic deformation of the muscle. The difference between the two tensions corresponds to the reflex response. Two components can be distinguished in this myotatic reaction; a fast, phasic component due to the brief lengthening, and a tonic one corresponding to the maintained stretch. The second part of the reflex mainly occurred in the slow extensor leg muscles providing the forces required to resist gravity.

The H-reflex, described by Paul Hoffmann (hence the name), in 1910 is evoked by electrical stimulation of Ia afferents and is analogous to the mechanically induced spinal stretch reflex because mimics mechanical activation of muscle-spindle fibres.

Development of the stretch reflex was investigated in the rat by Kudo & Yamada (1985) using the isolated spinal cord-hind limb preparation. Their main findings are: 1, stretch reflex response in the triceps surae muscle first appears at E19.5, at the same time as when Ia afferents contact spinal motoneurons (see above); 2, stretch reflex is evoked by monosynaptic transmission from the primary (Ia) afferents to the motoneurons; 3, homonymous excitatory postsynaptic potentials (EPSPs) are significantly larger than heteronymous EPSPs, reflecting somatotopic organization of the afferents input to the motoneuronal pools. The characteristic property of the stretch reflex in the neonatal rat is the lack of the tonic response to the ramp-and-hold stretch of the triceps surae. This fact was explained by the properties of the immature presynaptic terminals, such as depletion of the available store of transmitter, a failure of invasion of sensory impulses into every terminal or decrease in the probability of transmitter release at high repetitive rates (see discussion in Kudo & Yamada, 1985). Lev-Tov and Pinco (1992) have studied prolonged synaptic depression in the neonatal rat (P6-P8) using an isolated spinal cord preparation. No change in the GABA-ergic fast transmission or in the passive properties of the motoneurons (as branch-point blockade) are involved in the

prolonged depression. Confirming the proposal made by Kudo & Yamada (1985), these authors have suggested that depression of synaptic potentials in the neonatal rat reflects decreased transmitter output from the activated afferent terminals.

Several investigators have further studied monosynaptic reflexes and their development using the isolated spinal cord of fetal and neonatal rats (Saito, 1979; Fitzgerald *et al.*, 1987; Kudo & Yamada, 1987). It is concluded that monosynaptic reflexes in the isolated spinal cord can be recorded first form the L_4 VR at E18.5 following L_4 DR stimulation (Kudo & Yamada, 1987). Intersegmental polysynaptic responses (evoked by stimulation of the neighbour DR) are most prominent at E16.5-E17.5 and then are reduced in size near birth, reflecting the development of inhibitory transmission (Saito, 1979). Comparison of *in vivo* and *in vitro* recordings shows that appearance of VR reflexes is similar in both condtions (Fitzgerald *et al.*, 1987).

To the best of my knowledge, coordination between antagonistic muscles during stretch reflex in the rat has not been studied. In the cat contracting the extensor muscle during such a reflex leads to relaxation of its flexor antagonists. This type of antagonist muscle coordination is known as reciprocal innervation and involves a disynaptic pathway. In 1946, Lloyd clearly described the 'myotatic unit': each muscle is commanded by motor units which elicit the contractions, while a parallel structure controls the muscle spindles via the gamma motoneurons (Figure 2). The large-diameter Ia afferents facilitate the activity of the motoneurons of the stretched muscle and the 'homonymous' muscles (synergistic muscles) monosynaptically, whereas they inhibit the motoneurons of the antagonist muscles disynaptically (reciprocal inhibition; see Figure 3 left, panel). The Golgi tendon organs, which signal muscle tension when it contracts, send afferent messages to the spinal cord via different large fibres, the Ib afferents, which inhibit the homonymous muscles disynaptically and facilitate the antagonist muscles.

2.2 Polysynaptic reflexes

The best examples of the polysynaptic reflexes are those involved in the motor system activation with a protective aim, such as the flexion reflex, a nocifensive reflex, or a withdrawal reflex. The strength of the reflex depends upon the strength of the stimulus. A weak pinch produces flexion of the foot; a slightly stronger one,

flexion of both the foot and the leg; and a very strong one, flexion of foot, leg, and even hip.

Polysynaptic reflexes, which can be recorded from the VRs after DR stimulation in the isolated spinal cord preparation, are the first evoked discharges to appear (E15.5). The reflex response at that time consists of a prolonged depolarization of the VRs later downsized by the development of more mature neuronal networks and inhibitory mechanisms (Saito, 1979). Two days later (E17) pinching the hindlimb evokes a clear withdrawal reflex in the rat (see references in Fitzgerald 1985). Moreover, mechanical, thermal and electrical skin stimulation can clearly evoke hindlimb reflexes on the first day after birth (Fitzgerald & Gibson, 1984). Although withdrawal reflexes are seen at early stages, specific C-fibre evoked reflexes produced by chemical skin irritants do not occur until P10-P11 (Fitzgerald & Gibson, 1984). Thus, it has been proposed that in the neonatal spinal cord nociceptive pathways can be activated by low- or high-intensity stimuli: hence, neonatal A-fibres can evoke excitatory synaptic processes normally restricted to C-fibre input in adults (Fitzgerald & Jennings, 1999).

Development of protective reactions is tightly related to development of cutaneous afferent fibre inputs and receptive field organization. Perhaps the strongest impact on the investigation of cutaneous fields in rat was contributed by Maria Fitzgerald and colleagues. Recording *in vivo* from the lumbar spinal cord of rat fetuses still in contact with their mother revealed the ability to transmit cutaneous sensory information to the brain two days after (E19) the development of peripheral afferent receptive fields (E17) (Fitzgerald, 1991). Seventy five percent of all dorsal horn cells respond to only one (A or C) afferent input volley (P0-P3), showing lack of convergence of afferent inputs to neonatal dorsal horn cells (somatotopic organization). By day P14-15 51% of cells have only A inputs, and 49% share both A and C inputs, with no cells having exclusively C inputs. Although hyper excitability characterises most of dorsal horn cells during first week of life, fading of responses on repeated stimulation is also present (Fitzgerald, 1985). This habituation is probably due to immaturity of cell properties, because there is no failure of afferent input volleys (Fitzgerald, 1985).

Like for other sensory projections to the central nervous system, such as visual and thalamo-cortical ones, development of primary mechanoreceptive fields within the spinal cord is an activity-dependent process requiring NMDA receptor activation. In the rats treated from birth with the NMDA antagonist MK801, cutaneous

mechanoreceptive fields and A-fibre evoked responses are significally enhanced, while C-fibre evoked responses are unaffected. This effect may be due to prevention of the reorganization of A-fibre terminals: postnatal withdrawal of A-fibre primary afferents to deeper laminae does not occur in treated animals, although cell density in the dorsal horn is apparently unaffected (Beggs *et al.*, 2002).

2.3 Organization of inputs to spinal interneuron population and reconfiguration of spinal interneuronal system

Laminae V-VII interneurons are classified into four categories ('phasic', 'repetitive', 'single' and 'slow') based on their firing patterns in response to depolarizing current steps (Szucs *et al.*, 2003). Such a classification in conjunction with the morphological correlation and distribution of neurons may predict different signal processing characteristic of different components of motor neural assemblies (for electrophysiological classifications of the cells in different spinal laminae see references in Szucs *et al.*, 2003).

Another classification is based on the projection directions and clustering (see above; Silos-Santiago & Snider, 1992; Silos-Santiago & Snider, 1994; Eide *et al.*, 1999). Traditionally interneurons are classified on the base of their characteristic connections. Renshaw cells, for example, are distinguished from other interneurons by their specific cholinergic inputs from motoneurons (see above). Figure 3 (left) shows the neuronal circuit underlying spinal recurrent inhibition of motoneurons innervating skeletal muscles. In addition to the excitatory inputs from motoneurons and interneurons, Renshaw cells receive spinal and suprasegmental inhibitory inputs. This inhibition counteracts the excitatory inputs resulting from the motor discharges. The right panel of figure 3 illustrates the effects of changing recurrent inhibition on input-output characteristics of motoneurons. Input-dependent modulation of Renshaw cells activity significantly changes the motor output stage (Windhorst, 1996; Hultborn, 2006).

Edgley (2001) and Jankowska (2001) have reviewed the organization of inputs to spinal interneurons, their multifunctional character and purpose-dependent reconfiguration. While discussing subgroups of interneurons on the basis of characteristic inputs, Edgley suggested the existence of a modular organization of the spinal cord. In other words, the α- and γ-motoneurons that innervate an agonist

muscle, the Renshaw cells getting inputs from these motoneurons and Ia reciprocal inhibitory interneurons constitute one functional modular unit (on Figure 3 'motor output stage' plus Renshaw cell).

Motoneurons were recognized by Sherrington as the "final common pathway": however their reciprocal contacts, their interactions with Renshaw cells and complexity of transmitter release process rise doubts about them being the simplest element in the module. The multifunctional character of spinal interneurones was demonstrated by showing that certain neurons operate for different functions and that they may be incorporated into a number of larger networks. Jankowska (2001) describes five types of reconfiguration of spinal interneuronal networks (see Figure 1 in Jankowska, 2001) by mechanisms like presynaptic inhibition (Kremer & Lev-Tov, 1998; Vinay *et al.*, 1999; Rudomin, 1999) and target specific modulatory actions of monoamines. One of her important conclusions is: "since spinal interneurones are involved in several functions, the names used to denote them may appear to be misleading. Clearly none of the interneurones called Ia, or Ib, or group II are interposed in pathways from only one kind of afferent, and the same is true for interneurones interposed in pathways from cutaneous afferents or nociceptors".

2.4 Summary of spinal reflexes and functional organization of spinal cord

Spinal cord circuits responsible for purely sensory defined motor outputs are composed by a defined number of motoneurons and interneurons which are present at birth (some interneurons die after birth, but their number is not large; reviewed by Lowrie & Lawson, 2000). Moreover, certain inputs and interconnections are already established. Nevertheless, the system does not work following strictly defined rules, it works in a goal-directed manner. Each single element can be changed depending on the goal, starting from the primary afferent terminals to the integrative properties of motoneurons. Furthermore, multiple levels of functionality can exist by using the same elements and connections.

When trying to analyze this kind of system, relations are neither linear nor exponential and unexpected responses may emerge (see recent Vervaeke *et al.*, 2006). However, it is possible to define morphologically fixed modules, whose activity and behavior can be described. One objective of the present study was to

find appropriate tools to analyze such basic elements, taking as an example spinal motoneurons. The next sections will deal with rhythmic motor activity like locomotion, in which the command to hindlimb motoneurons is generated in the lumbar spinal cord by a group of cells known as spinal central pattern generator (spinal CPG).

3. Locomotion and locomotor related spinal networks

Shik and Orlovsky (1976), reviewing the neurophysiology of locomotor automatism, termed locomotion as "the movement of terrestrial animals on the firm flat surface along a direct line, maintaining equilibrium and using the whole range of normal velocities and gaits". This consideration allows using as models animals with partially destroyed or fully removed brain structures.

The sequence of joint movements is fixed and does not depend on the speed of locomotion, but their parameters of the step (duration, amplitude of the joint movements) can vary. The basic pattern of the limb stepping movement can be divided into two phases: the stance phase during which the limb is in contact with the ground and moves backward in relation to the body, and the swing phase, when the limb is elevated and protracted forward.

3.1 Development and localization of locomotor CPG in rats

Locomotor speed is controlled in two possible ways: by varying propulsive forces developed by limb muscles associated with an increase in the amplitudes of the joint movements, or by changing the frequency of stepping (stance duration). Experimental data obtained from mesencephalic cats (reviewed by Shik & Orlovsky, 1976) suggest that muscle forces are directly controlled by the brain, whereas the frequency of stepping is controlled by spinal locomotor networks.

The spinal origin of locomotor the rhythm has been proved by investigations using isolated preparations, lesions, pharmacological and electrophysiological techniques (only recent reviews Kiehn & Butt, 2003; Clarac *et al.*, 2004; Nistri *et al.*, 2006; Kiehn, 2006).

Much of the pattern and timing of such complex, rhythmic, coordinated muscles activities as locomotion in mammals is attributed to the spinal cord network called

central pattern generator (CPG). In the 60s-70s it was discovered that most rhythmic motor systems could generate patterned activities in the absence of afferent feedback. During the 80s it became evident that CPGs are capable of generating a variety of patterns depending on the conditions, especially in the presence of different neuromodulatory substances (for review Pearson, 2000; Dietz, 2003). When compared to the recent knowledge about the CPG in the nonmammalian vertebrates species (Orlovsky *et al*., 1999), our understanding of locomotor CPGs in mammals remains, however, limited (Clarac *et al*., 2004; Kiehn, 2006; Nistri *et al*., 2006).

One of the most intriguing questions addressed in recent studies of the spinal CPG is its neuronal composition. In the next few paragraphs I'll try to overview recent data regarding spinal CPG development and location. It should be noted that most experiments have been done on the isolated thoracic/lumbar spinal cord preparation of fetal or neonatal rats. In this preparation, alternating bursting between left and right VRs of the same segment and between ipsilateral roots of segments innervating antagonistic muscles (L2/L3 supply activity of flexor muscles, while L5 predominantly innervates extensor muscles) can be induced by bath application of neuro-active substances, like N-methyl-D-aspartate (NMDA), acetylcholine, 5-hydroxytryptamine (serotonin or 5-HT), dopamine and noradrenaline (for references see Nishimaru & Kudo, 2000). The locomotor-like activity can be also evoked by high frequency stimulation of one DR (Marchetti *et al*., 2001a) or by elevation of the extracellular K^+ concentration (Bracci *et al*., 1998).

During embryonic life, three stages of development of rhythmic activity evoked by NMDA or/and 5-HT can be identified. At the first stage (E14.5-E16.5), the rhythm is synchronous between all roots, at E18.5 left and right VRs of the L2/L3 segments produce anti phase signals, while L5 VRs burst in synchrony with ipsilateral L2/L3 VRs. Two days later the whole range of pattern alternation characteristic of the newborn or adult is established. This temporal development of locomotor activity probably mirrors development of segmental and intersegmental CIN projections (see above) and the time dependent maturation of inhibitory transmission (notice similarities to the development of polysynaptic reflexes). Formatting of CPG for locomotion in the rat has been reviewed by Nishimaru and Kudo (2000).

The localization of the locomotor CPG in rats has been recently reviewed by Kiehn (2006). Briefly, the rhythmogenic capacity is located ventrally in the cord (laminae

VII, VIII and X) and is distributed over the lumbar spinal cord and, at least in the rodent, into the lower thoracic level, with a greater capacity to generate a rhythm in rostral than in caudal segments. This conclusion is based on lesion studies and is supported by activity-labeling and electrophysiological studies. Thus, the CPG organization is composed of multiple distributed rhythm generating modules, instead of one rhythm-generating core localized in the upper lumbar cord. The stereotyped pattern of limb movement in locomotion indicates that individual joints are not controlled by the nervous system as elementary units, rather the limb is controlled as a whole (Shik & Orlovsky, 1976).

3.2 Left-right coordination during fictive locomotion and its development

The circuit responsible for the left-right coordination in rats is probably the only one successfully studied at cellular level. Deep understanding of left-right alternation mechanism was obtained by means of different technical approaches. Various interneurons (divided on the basis of axonal projections and introduced earlier) appear to play a deterministic role in left-right coordination (reviews Butt *et al.*, 2002; Butt & Kiehn, 2003; Kiehn, 2006).

Nishimaru and colleagues (1996) described spontaneous synchronized bursts in both right and left VRs which were insensitive to glutamate antagonists from E14.5 to E15.5. Only at E17.5 did these antagonists completely blocked them. It was concluded that glycine and GABA generate the earliest spontaneous motor activity of the fetus and both these transmitters function transiently as excitatory transmitters in the embryonic spinal cord (Nishimaru *et al.*, 1996; Kudo & Nishimaru, 1998). At the same time, a synchronous rhythm can be activated by NMDA and 5-HP; sporadic left-right alternation appears only at E18.5 and fictive-locomotion later at E20.5. The main conclusion is that the switch from the excitatory action of glycine and GABA to an inhibitory one determines the time of left-right alternation appearance (confirmed by calcium imaging and split bath experiments; Nakayama *et al.*, 2002). These observations also suggest that neuronal networks possessing predominantly excitatory connections can generate synchronous rhythmic motor activity in the absence of synaptic inhibition (Kudo & Nishimaru, 1998).

3.3 Disinhibited activity in the isolated spinal cord of the neonatal rat

Block of inhibitory synaptic mechanisms in P3-P13 rats shows that inhibitory inter- and intrasegemental interneurons are not needed to produce purely excitatory rhythmic activity in the isolated lumbar spinal cord. Such activity induced by pharmacological block of inhibition is termed disinhibited activity and is of particular interest because it exhibits highly regular rhythmic bursts (frequency ~2 per min, duration ~7 s), which arise spontaneously and lasts for many hours (Bracci *et al.*, 1996a; Bracci *et al.*, 1997). Thus, a disinhibited network is able not only to generate bursts but also to control its duration and periodicity. Each burst has a characteristic structure comprising a rapid depolarization followed by large-amplitude oscillations (Bracci *et al.*, 1996a,b; this study), so it is different from, for example, irregular bursting induced by block of GABAergic transmission *per se*, which comprise individual events fused together (Bracci *et al.*, 1996a; this study) or from activity induced by block of certain K^+ conductances (Taccola & Nistri, 2004, 2006).

Another important feature of disinhibited activity is that it appears synchronously in all lumbar motoneuronal pools and has network origin, because burst frequency, duration, and intraburst oscillation time course are independent of motoneuron membrane potential. Furthermore, bursts and oscillation amplitude are membrane potential dependent and under voltage-clamp conditions invert polarity near 0 mV confirming the synaptic origin of this activity. Further confirmation of the network origin has been obtained by its block by the voltage-sensitive Na^+ channels antagonist tetrodotoxin or the voltage-sensitive Ca^{2+} channel blocker Cd^{2+} (Bracci *et al.*, 1996a).

All these experiments suggest the existence of excitatory networks that are responsible for rhythm generation in the rat spinal cord and exclude an independent, half-center organization for flexor and extensor muscle activity. The relation of disinhibited rhythm to the locomotor activity is of particular interest and has been studied using segmental isolation (split-bath) and lesion experiments (Bracci *et al.*, 1996b; Beato & Nistri, 1999). Isolation experiments revealed strong synergy between disinhibited rhythm and locomotor pattern. This synergy is expressed in the presence of typical alternation between locomotor-like patterns

generated during each interburst interval even in the absence of 5-HT and/or NMDA, despite the presence of strychnine and bicuculline in the caudal area (5-HT and/or NMDA applied to the isolated rostral region). Lesion studies have shown that networks generating disinhibited rhythm and locomotor patterns are similarly located in the anterior quadrant of the spinal cord (Bracci *et al.* 1996b; Kjaerulff & Kiehn, 1996). It is interesting to note that, while the intraburst structure of disinhibited bursts is preserved only in a circuitry comprising either both ventral horns or one side of the spinal cord with more than two segments (Bracci *et al.* 1996b), one side of the cord containing only L4 and L5 VRs can produce alternating rhythmic activity in flexor (tibialis anterior) and extensor (gastrocnemius) muscles after application of NMDA (Nishimaru & Kudo, 2000).

3.4 Role of cell metabolism in the control of neuronal excitability.

K_{ATP} channels

Although the riluzole sensitive persistent Na^+ current (I_{NaP}) apparently paces disinhibited bursting in spinal cord organotipic cultures (Darbon *et al.*, 2004), this effect has not confirmed using isolated spinal cord preparations. Only in a minority of preparations did riluzole completely block disinhibited activity, while in others it just increased interburst intervals (G. Taccola, personal communication). While these findings do not exclude the involvement of I_{NaP} in generation of disinhibited activity, they suggest additional mechanisms are responsible for control of bursting.

Since Na/K pump antagonists like strophanthidin or ouabain disrupt rhythmic bursting (Ballerini *et al.*, 1997; Rozzo *et al.*, 2002), it was proposed that the operation of the electrogenic Na^+ pump of premotoneurons is a crucial element for rhythmic bursting. Nevertheless, after about 1 hour of pump block, the network surprisingly resumes spontaneous bursting (Rozzo *et al.*, 2002). This pattern, recorded from lumbar VRs, is synchronous in the both sides, of irregular periodicity, and lasts for ≥12 hours.

The analysis of distribution and correlation of strophanthidin burst parameters reveals a strong correlation of burst duration with burst amplitude and with length of the preceding pause (Rozzo *et al.*, 2002), suggesting an activity-dependent mechanism for burst termination and a stochastic nature of burst onset. The same

conclusions have come from experimental and modeling investigations of expression and self-regulation of spontaneous activity in the developing chick spinal cord (Tabak *et al.*, 2000; Tabak *et al.*, 2001). The search for the activity-dependent mechanism, which can be activated during long-lasting electrical activity of spinal interneurons, led to the idea of metabolic regulation of spinal cord excitability. Such a metabolic regulation can be provided by cyclic activation of ATP dependent K^+ channels (K_{ATP}), a known link between the cell metabolic state and its excitability (see reviews by Bryan *et al.*, 2004; Minami *et al.*, 2004; Yamada & Inagaki, 2005; Nichols, 2006). These channels couplecellular metabolism to electrical activity by opening when the intracellular ATP/ADP ratio decreases and by closing as the ratio increases.

The activity of K_{ATP} channels has been intensively studied in pancreatic β-cells. When glucose rises, cell metabolism is stimulated, raising the ratio of ATP to ADP to close K_{ATP} channels. This process depolarizes the cell and opens Ca^{2+} channels, causing intracellular Ca^{2+} increase and insulin secretion. Insensitivity of K_{ATP} to ATP inhibition causes maintained hyperpolarization and decreased insulin secretion, which is one of the pathogenetic factors of diabetes mellitus (Figure 4a; Ashcroft, 2005; Nichols, 2006).

K_{ATP} channels are formed by the unique combination of two dissimilar proteins. One, Kir6, is a member of the Kir channel family; the other, SUR (for sulphonylurea receptor), is a member of the ATP-binding cassette (ABC) protein family. ATP inhibition results from interaction with the Kir6 subunits, whereas the ADP activation reflects interaction with SUR subunits. Figure 4b shows subunit organization of the K_{ATP} channels.

The two prime candidates for formation of functional K_{ATP} channel in the brain are the Kir6.2 subunit of the K^+ channel family plus the SUR1 element of the glibenclamide-sensitive sulfonylurea receptor (Aguilar-Bryan & Bryan, 1999). Although Kir 6.2 subunits are moderately expressed in the adult rat spinal cord (Thomzig *et al.*, 2005), their expression in the developing spinal cord is unknown.

***Figure 4**. The K_{ATP} channel structure and function in pancreatic β-cells*

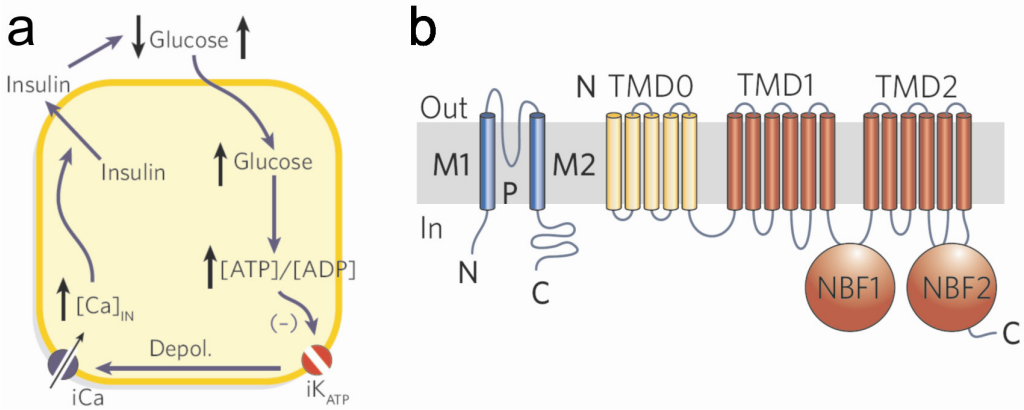

a, when glucose rises in the pancreatic β-cell, metabolism is stimulated, raising the ratio of ATP/ADP. This closes K_{ATP} channels, which depolarize the cell, opening Ca^{2+} channels, snd causing intracellular Ca^{2+} to rise, to trigger insulin secretion. Insensitivity of K_{ATP} to ATP inhibition will cause maintained hyperpolarization and decreased insulin secretion. b, inward rectifier K^+ channel Kir6 subunits generate the channel pore and sulphonylurea receptor (SUR) subunits generate the regulatory subunit. TMD, transmembrane domain; NBF, nucleotide-binding fold; M1, M2, transmembrane helices; P, pore. (modified from Nichols, 2006).

Experiments on brainstem respiratory centers have revealed a dynamic activation of K_{ATP} channels in rhythmically active neurons. K_{ATP} channels are periodically activated in synchrony with each respiratory cycle (Pierrefiche *et al.*, 1996; Haller *et al.*, 2001), reflecting activity-dependent fluctuations in the ATP concentration within submembrane domains. In these studies such sulphonylureas as glibenclamide (50 μM) and tolbutamide (500 μM) were used to block K_{ATP} channels, via their binding to SUR1 (reviewed by Bryan *et al.*, 2004). This process therefore provides an important mechanism to modulate rhythmic motor discharges and to continuously adjust them in response to changes in environmental conditions. Whether the similar mechanism operates in the spinal cord remains an unexplored question.

Aims of the present study

This study includes two approaches to the investigating the function of spinal cord networks.

i. Since the ATP-dependent Na^+-K^+ pump is a major controller of spinal network bursting (Rozzo *et al.*, 2002), I wondered whether periodic changes in intracellular ATP might control the activity of K_{ATP} conductances and thus limit neuronal excitability. One simple functional test for this possibility is to apply a K_{ATP} channel blocker like glibenclamide (Bryan *et al.*, 2004) and to monitor resultant changes in network responses. This approach soon led me to unexpected results which raised the issue of a novel mechanism to control spinal network excitability. Furthermore, these data allowed me to provide a new basis to interpret the role of GABA and glycine as inhibitory neurotransmitters at an early postnatal stage of development.

ii. The goal of the second part of present study is to construct a model of a rat spinal motoneuron built on the basis of available morphological data. This model comprises, in 3D, the developmental changes in the morphology occurring during first postnatal week and may be useful to simulate electrical properties of motoneurons, including the novel experimental data obtained in the present thesis.

Methods

1. Tissue preparation and drugs

1.1 Spinal cord tissue preparation

The spinal cord, from low cervical segments to *conus medullaris*, was isolated from neonatal Wistar rats (4 to 8 postnatal days old, P4-P8). Animals were firstly anaesthetized with an intraperitoneal injection of urethane (0.2 ml ip of a 10% wt/vol solution). As soon as the animal lost the withdrawal reflex, it was rapidly decapitated with scissors. The forelimbs and the ventral part of the chest were removed and the animal was eviscerated in order to expose the ventral side of the vertebral column. The remaining skin was also removed and the body was washed in cooled (4° C) oxygenated (95% O_2- 5% CO_2) artificial cerebrospinal fluid (ACSF; see composition below) and fixed by pins with the ventral side upon to the sylgard bottom of a Petri dish containing ACSF at the same temperature. The solution contained in the dish was continuously oxygenated. A complete laminectomy was performed in the rostrocaudal direction under the microscope. Meningeal tissue was removed from the ventral side, while DRs and VRs were cut as close as possible to the dorsal root ganglia. Remaining meningeal tissue present on the dorsal side of the spinal cord was also removed. For motoneuron studies the spinal cord was hemisected sagitally.

For slice preparations a tissue block containing the lumbar spinal cord, obtained as described before but using dissection ACSF solution (see below), was fixed (with insect pins) onto an agar block inside a Vibratome chamber filled with ice-cold oxygenated ACSF. Slice thickness varied from 200 to 300 μm. Slices were first transferred to an incubation chamber for 1 h at 32° C under continuous oxygenation and subsequently maintained at room temperature for at least 1 h before use.

1.2 Recording chamber for the isolated spinal cord experiments

After dissection, the whole spinal cord was pinned (ventral part upwards) to the sylgard bottom of a recording chamber made of plexiglass (internal volume ~3 ml)

and was continuously perfused with ACSF. The hemisected spinal cord was pinned with its medial side upwards. Perfusion was fed by a peristaltic pump that delivered oxygenated ACSF to the recording chamber, via a small tubing, parallel to the rostrocaudal axis of the spinal cord and ACSF outflow was drained via a small channel. Constant flow rate was ensured by a flow spacer places between the pump and the chamber to damp fast oscillations in the fluid level. Flux was maintained between 5 and 7 ml/min. All neurochemicals were applied via the perfusion system. The time necessary to completely exchange the solution in the bath was estimated using ACSF stained with phenol red and found to be less then 3 minutes.

1.3 Recording chamber for the whole cell-patch experiments and identification of the cells

Spinal cord slices after the incubation were placed in the small recording chamber and fixed by a fine nylon net glued to a horse-shaped platinum wire and continuously perfused (2-3 ml/min) with recording oxygenated ACSF solution (see below). Drugs were applied in two different ways: either bath-applied via the extracellular solution (for a minimum of 5-10 min to reach apparent equilibrium conditions), or via fast, focal pressure pulses. For the latter method, a thin-walled glass micropipette was pulled in the same way as a patch pipette using a two stage puller (3P-A, List Medical, Germany) in order to obtain a DC resistance of 5-6 MΩ. The pipette was filled with 4-aminobutanoic acid (GABA; diluted to the final concentration of 500 μM in the external recording solution), and positioned approximately 20-50 μm away from the soma of the recorded cell, under microscopic control. The final position was chosen following two criteria: reproducibility of evoked electrical responses and lack of the mechanical influence on the cell's surface. The puffer pipette was connected to a Pneumatic Picopump (WPI, Saratosa, FL, USA); and, pulses duration ranged from 10 to 20 ms (4-8 p.s.i. pressure).

Motoneurons were identified using an upright microscope and infrared video camera as the largest cells (≥ 20 μm soma diameters) located in the most ventral laminae of the slice (laminae IX; see also Takahashi, 1990). Interneurons were identified as small cells (≤15 μm soma diameter) lying ventrally close to the central canal (lamina X).

1.4 Extracellular, intracellular solutions and drugs

1.4.1 Extracellular solution for spinal cord isolation, maintenance and recordings (whole spinal cord recordings)

Composition for both dissection and recording was (in mM): NaCl 113, KCl 4.5, $MgCl_27H_2O$ 1, $CaCl_2$ 2, NaH_2PO_4 1, $NaHCO_3$ 25 and glucose 11, gased with 95% O_2- 5% CO_2, pH 7.4. All experiments were performed at room temperature.

1.4.2 Intracellular solution for sharp electrode current-clamp recordings

Sharp electrodes were filled with 2 M $KMeSO_4$. For recording of recurrent inhibitory post synaptic potentials (rIPSPs) 20 mM QX-314 was added to minimize Na^+-dependent spikes and stabilize cell membrane potential.

1.4.3 Intracellular solution for sharp electrode voltage-clamp recordings

Sharp electrodes were filled with 2 M Cs_2SO_4 plus 20 mM QX-314.

1.4.4 Extracellular solutions for slice preparation, maintenance and recordings

The solution used for spinal cord isolation, slice cutting and maintenance contained (in mM): NaCl 130, KCl 3, NaH_2PO_4 1.5, $CaCl_2$ 1, $MgCl_2$ 5, $NaHCO_3$ 25, glucose 11 (pH 7.4 adjusted with NaOH; 290-310 mosmol l^{-1}). The extracellular solution used to perfuse slices during recording contained (in mM): NaCl 130, KCl 3, NaH_2PO_4 1.5, $CaCl_2$ 1.5, $MgCl_2$ 1, $NaHCO_3$ 25, glucose 11 (pH 7.4 adjusted with NaOH; 290-310 mosmol l^{-1}).

1.4.5 Intracellular solutions for whole-cell patch clamp recordings

Patch electrodes were filled with (in mM) KCl 130, NaCl 5, $MgCl_2$ 2, $CaCl_2$ 0.1, HEPES 10, EGTA 5, ATP-Mg 2, GTP-Na 1, QX-314 0.5 (pH 7.2 with KOH; 280–300 mosmol l^{-1}). For some recording from spinal interneurons, the stable cAMP analogue 8-bromo-cAMP (400 μM) was added to the intracellular solution.

1.4.6 Intracellular solutions with low Cl^- concentration for whole-cell patch clamp recordings to investigate changes in the Cl^- reversal potential

Patch electrodes were filled with (in mM) Cs-methylsulfonate 109, CsCl 8, $MgCl_2$ 2, NaCl 8, HEPES 10, EGTA 1, ATP-Mg 4, Na_3GTP 0.3, QX-314 0.5 (pH 7.2 with CsOH; 280–300 mosmol l^{-1}).

1.4.7 Drugs and reagents

For electrophysiological experiments we used bicuculline methiodide, strychnine hydrochloride, 4-hydroxyquinoline-2-carboxylic acid (kynurenic acid), GABA, cesium sulphate, Cs-methylsulfonate, lidocaine N-ethyl bromide (QX-314), diphenylamine-2,2′-dicarboxylic acid (DPC) and tolbutamide purchased from Sigma (Sigma-Aldrich,Milan, Italy). Potassium methyl sulphate was purchased from Fluka (Buchs, Switzerland). Glibenclamide were purchased from Tocris (Tocris Bioscience, Ellisville, Missouri, USA). CFTRinh-172 (3-[(3-Trifluoromethyl)phenyl]-5-[(4-carboxyphenyl)methylene]-2-thioxo-4-thiazolidinone) was purchased from Calbiochem (Darmstadt, Germany). Stock solutions of the agents (usually at concentrations 10^3 higher than the final ones) were made in distilled water and frozen in small aliquots (≤ 1 ml volume). The final concentration was obtained by dissolving an amount of the stock into the ACSF. Concentration of the drugs that were dissolved in dimethylsulphoxide (DMSO) was such that DMSO concentration in bath was <0.02 %.

For Western blotting experiments, the protease inhibitors cocktail was purchased from Roshe (F. Hoffmann-La Roche Ltd, Basel, Switzerland). Bicinchoninic acid assay was purchased from Sigma (Sigma-Aldrich, St. Louis, MO, USA). 3-8 % Nu-PAGE Novex was purchased from Invitrogen (Invitrogen S.R.L, San Giuliano Milanese, Italy). Anti-CFTR antibody was purchased from Alomone (Alomone Labs Ltd., Jerusalem, Israel).

2. Recording techniques

2.1 Extracellular ventral root recordings

Ventral roots recordings were performed with miniature monopolar suction electrodes made from heat pulled glass capillaries. Electrode tips were fire polished and the size of their tip was selected to (a) allow entry of the entire VR and (b) provide a tight fit of the VR. Roots were sucked into the electrode by applying

gentle negative pressure with a syringe connected to the apical end of the pipette. When the root was entirely inside the electrode, further negative pressure was delicately applied in order to obtain a seal between the tip of the pipette and the ventral surface of the spinal cord. Electrical contact was achieved by filling the pipette with ACSF solution and connected via Ag/Ag-Cl micropellet (Harvard Apparatus, UK) to a custom made low-noise DC coupled amplifier or DAM 50 (World Precision Instruments, FL, USL) differential amplifier, using bipolar suction electrodes.

Signals were also displayed on-line on a Gould chart recorder, digitized and recorded on VHS tape for further off-line analysis.

2.2 Intracellular recordings

Intracellular recording from motoneurons was performed with sharp glass electrodes filled with intracellular solution (see above) and connected via 0.1x headstage (Axon instruments) to an amplifier (Axoclamp 2A, Axon Instruments). Electrode resistance varied between 50 and 90 MΩ for $KMeSO_4$-filled electrodes and between 60 and 120 MΩ for Cs_2SO_4-filled ones.

As the sharp electrode was lowered into the ventral spinal cord, the following stimulation protocol (delivered at a frequency of 2 Hz) allowed motoneurons to be identified: a negative current step (10 ms, 0.5 nA) for monitoring electrode resistance, followed, with a 50 ms lag, by a pulse stimulus (0.1 ms duration) applied to the ipsilateral homologous VR (antidromic stimulation).

When the electrode was in proximity to the motor nucleus, antidromic stimulation evoked a short latency (~2 ms) biphasic field potential due to a synchronous motoneuron firing (Fulton & Walton, 1986), while the increase in the electrode resistance was used as a sign that the tip of the electrode was in contact with the membrane of the electrode. At this stage, the "clear" command of the amplifier was applied, in order to facilitate penetration into the membrane.

Current-clamp experiments were performed in bridge mode. After motoneuron impalement, VR stimulation elicited at short latency (<2 ms) all-or-none overshooting antidromic action potential (Fulton & Walton, 1986). Only cells in which this kind of response could be consistently elicited were considered for analysis.

Electrode capacitance was compensated (in Discontinuous Current Clamp mode (DCC) at 1.5-2.0 Hz sample rate). Motoneuron input resistance was constantly monitored by injecting a negative current pulse (20-50 ms); it was then calculated as the ratio between the steady state hyperpolarization induced by injection of the pulse and the amplitude of the current injected. Bridge balance was routinely monitored and compensated whenever necessary. To monitor voltage-dependence of single cell responses, current-voltage (I-V) cures were performed. In this case, successive hyperpolarizing (-0.1 to 0.9 nA, with 0.1-0.2 nA intervals) and depolarizing (0.1-0.9 nA; upper value was limited by action potential appearance) current steps, were delivered at 0.2-0.5 Hz.

Single-electrode voltage-clamp experiments were performed in single electrode voltage clamp (SEVC) mode at a sampling frequency of ≥2 kHz and gain ≥0.8 nA/mV using an Axoclamp 2A amplifier unit. The signal decay from the headstage was monitored continuously to ensure that correct level of capacitance compensation was maintained and that sampling occurred only after the full decay of the voltage transient. The sharp electrode contained Cs^{2+} and QX-314 to decrease K^+ leakage currents and block voltage-activated Na^+ currents, respectively. Before switching to SEVC configuration motoneurons were identified as described before.

To explore the Cl^- reversal potential (E_{Cl^-}) of motoneurons, inhibitory postsynaptic currents (IPSCs) were evoked by antidromic stimulation (0.05 Hz) at various holding potentials in the presence of kynurenic acid and averaged. E_{Cl^-} was calculated by extrapolation from plots of synaptic charge versus holding potential as sharp electrode recording in voltage clamp limited the amount of current that could be applied into the cell.

2.3 Electrical stimulation

Miniature bipolar suction electrodes were used in order to deliver single or repetitive electrical stimuli to either dorsal roots or VRs. Such electrodes were made from the thin (1.5 mm diameter) glass capillaries and contained a silver wire inside and another one wound around. Electrode tip diameter was chosen to closely fit the root to be stimulated. Square electrical pulses (0.1-0.2 ms duration, 0.5-10 V amplitude) were applied via a Digitimer D100 (Digitimer Ltd., England) or Grass

S88 (Grass Medical Instruments, Mass., USA) stimulator to isolated stimulator units connected to either VRs in order to antidromic stimulate motoneurons, or to DRs to activate afferent fibers. For each preparation, the intensity of stimuli delivered to DRs was expressed in terms of threshold (Th), defined as the minimum intensity able to elicit a detectable response in the homolateral VR.

2.4 Recurrent post-synaptic potential recording

In several experiments, it was necessary to record the Renshaw cell mediated recurrent inhibitory postsynaptic potentials (rIPSPs) or currents (rIPSCs). Although sharp electrodes allow only limited diffusion of the intacellular solution into the cell (especially when compared to the whole cell patch clamp technique), $KMeSO_4$- and $CsSO_4$-filled electrodes were nevertheless used to avoid any disruption of the Cl^--mediated rIPSPs or rIPSCs, respectively. Furthermore, in order to avoid interference of the rIPSP (rIPSC) measurement by the antidromic action potential afterhyperpolarization, motoneuron spike was blocked by adding the sodium channel blocker QX-314 to the intracellular solution. To block glutamatergic component of the antidromically evoked postsynaptic responses (Marchetti *et al.*, 2002) kynurenic acid (3 mM), the glutamate channel antagonist, was added to the extracellular solution. At the final stage of some experiments strychnine (2 μM) and bicuculline (20 μM) were added to verify glycinergic and GABAergic origin of recorded responses (see also Marchetti *et al.*, 2002). Figure 5 shows schematic representation of the recurrent inhibitory pathways in the spinal cord (left) and rIPSPs graded with VR stimuli intensity (right). The rIPSPs are positive going at resting membrane potential of -70 mV because of the less negative reversal potential for Cl^- at this age.

2.5 Experimental configurations

Intracellular recordings from single motoneurons were obtained from lumbar (L2-L5) segments. Two extracellular electrodes were used to deliver antidromic stimuli to the VR and orthodromic stimuli to the DR homolateral to the motoneurons, respectively. In these experiments the spinal cord was rotated in the chamber with

Figure 5. *Glycine and GABA mediated synaptic potentials in the spinal cord*

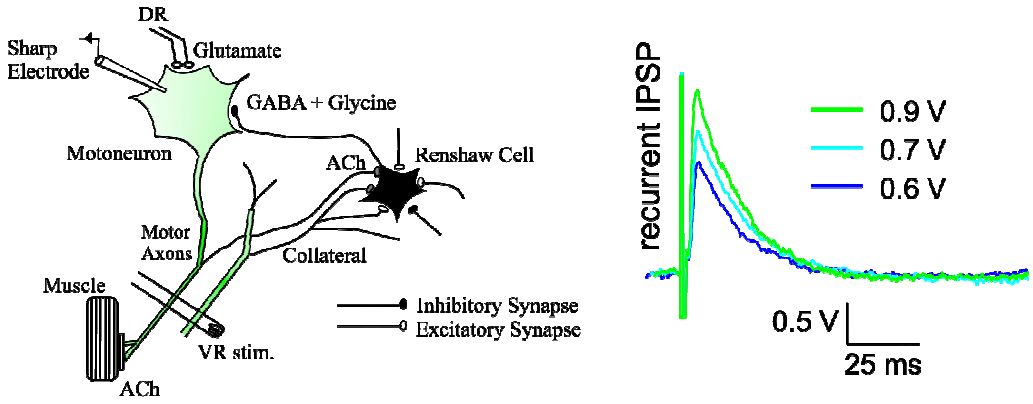

Left, schematic representation of the recurrent inhibitory pathways in the spinal cord. Only one motoneuron is shown together with one Renshaw cell. Transmitters used by different synapses are also indicated. ACh, acetylcholine. Right, rIPSP amplitudes are graded with the intensity of the VR delivered stimuli.

respect to the intracellular electrode that allowed the ventralateral part to be more accessible to the microelectrode. The sharp electrode was lowered vertically into the tissue by means of a micromanipulator. Extracellular recordings were usually performed from VR homolateral to the stimulated DR.The mono- or polysynaptic origin of extracellularly recorded VR responses evoked by weak (1 x Th) or strong (>1 x Th) DR stimulation, respectively, was verified by simultaneous intracellular recording from motoneuron and extracellular recording from the corresponding VR. Figure 6a shows a schematic representation of experimental configuration. A DAM 50 differential amplifier (gain 1000; DC mode; A-B input) was used together with bipolar suction recording electrode to record VR activity; an Axoclamp 2A amplifier was used for intracellular recording. Superimposed intracellular and extracellular responses to different DR stimuli are shown in Figure 6c. DC-coupled VR recording is a suitable method to detect fast firing activity (Figure 6b) and also slower membrane potential variations of the population of motoneurons from which the recording is made (Figure 6d). Under these conditions, firing activity usually appears as a biphasic signal, and slow polarization changes that take place simultaneously in a large population of motoneurons, preserve the same polarity as the one observed with the intracellular technique.

Figure 6. *DC-coupled VR recording technique*

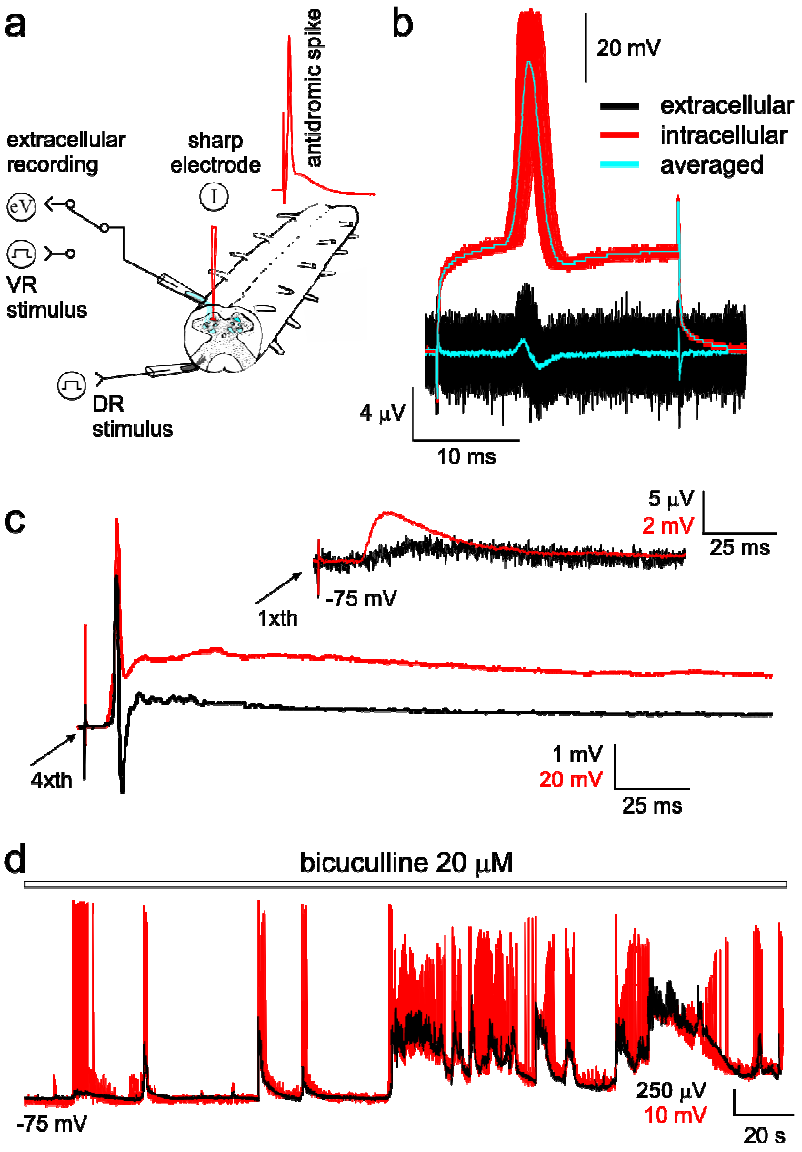

a, schematic representation of the intact spinal cord in vitro, during simultaneous intracellular recording from motoneuron and extracellular recording from VR of the same segment and homolaterally to motoneuron. Motoneuron was identified by the presence of the antidromic spike, following VR stimulation (shown in red). b, injection of depolarizing current (+1.2 nA) into antidromically identified motoneuron recorded at -70 mV evoked single spike on the top of the voltage response (red, averaged spikes are shown in blue). Simultaneously recorded activity of the VR revealed that firing activity appears as a biphasic signal during DC-coupled VR recording (black, averaged responses are shown in blue). c, DR stimulation with low (1x Th) or strong (4x Th) pulses evoked mono- or polysynaptic responses recorded both intracellularly and extracellularly. Note that during strong stimulation two phases of response can be separated: a fast one due to summation of monosynaptic fast responses and a slow one due to polysynaptic long lasting responses (the same color legend as for b; decay phase of polysynaptic responses is truncated). d, application of GABAergic transmission antagonist bicuculline (20 µM) evoked irregular bursts of motoneuron membrane potential, often comprising individual events fused together (red). Black trace represents DC-coupled recording of the VR activity. Note that slow polarization changes mirror slow membrane potential changes that took place simultaneously in a large population of motoneurons.

2.6 Viability of the spinal cord

After dissection, the viability of the spinal cord was ascertained before any further testing. In healthy preparations, single pulse stimulation (0.1-0.2 ms, 0.5-2 V) delivered to one DR elicited a reflex response from the ipsilateral VR at the same segmental level. If this response was absent, the preparation was discarded. Spinal cord preparations could usually be maintained *in vitro* for >12 hours without apparent sign of rundown of electrophysiological properties. Reliability of single cell recording was continuously monitored by checking input resistance to antidromic stimulation. These recording could be kept stable for several hours.

2.7 Patch clamp recording

Recording was performed at room temperature. The conventional whole-cell patch clamp technique (Hamill *et al.*, 1981) was employed. Briefly, a small heat-polished glass pipette, pulled from thin-walled borosilicate glass capillaries (Hingelberg, Germany) with a two-stage puller to a DC resistance 3-5 MΩ, was pressed against the cell membrane. Gentle suction, applied to the pipette interior, led to the formation of an electrical seal with resistance in the order of 2-10 GΩ (giga-seal). After the giga-seal formation, additional suction applied to the pipette interior led to membrane rupture, and direct low resistance access to the cell interior.

An L/M EPC-7 patch clamp Amplifier (List Medical, Germany) was used for voltage clamp experiments. Cells were clamped at -60, -65 mV holding potential (V_h) and series resistance (5-25 MΩ) was routinely monitored, without any compensation. Voltage pulse generation and data acquisition were performed with a PC using pClamp 9.2 software (Axon Instruments Inc.). All recorded currents were filtered at 3 kHz and sampled at 5-10 kHz.

While identification of spinal motoneurons was described previously (Takahashi, 1990), identification of spinal interneurons in the present study was based on their specific localization and non-linear response to the slow ramp change of the Vh. Figure 7a shows one characteristic current-voltage curve. Moreover, resting membrane potential was usually around -55 mV, capacitance 66±11 pF and input resistance 881±390 MΩ (n=40). To explore the Cl^- reversal potential (E_{Cl^-}) of motoneurons, GABA responses were evoked by puffer application of GABA via a closely positioned pipette (see above; scheme on Figure 7b) at various holding

Figure 7. *Identification of interneurons and their responses to puffer application of GABA*

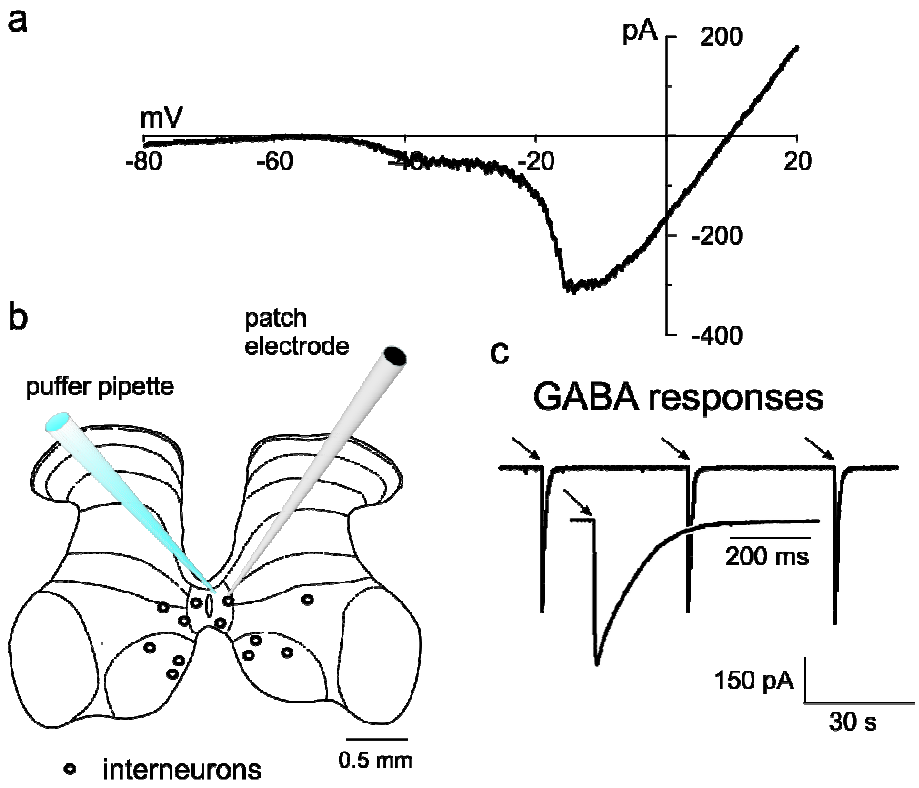

a, characteristic I/V response of spinal interneuron located ventrolaterally to the central canal. b, localization of recorded interneurons and experimental configuration; puffer pipette used for focal application of GABA and patch electode are shown. c, time interval before subsequent application of GABA was chosen to avoid desensitization of GABA receptors (arrows represent time of GABA application). Insert represents GABA response on expanded time scale.

potentials in the presence of kynurenic acid. To avoid desensitization of GABA-evoked responses, the time before subsequent agonist application was carefully chosen (usually >40 s; Figure 7c). Amplitude and charge transfer of GABA evoked responses were measured at various membrane potentials around reversal and were used to estimate changes in E_{Cl^-} (Dzhala *et al.*, 2005).

Junction potential was calculated using Junction Potential Calculator (Clampex 9.2) for both intacellular solutions that have been used. For solution containing high intracellular Cl^- concentration, junction potential value is equal to 10 mV (see also Marchetti et al., 2002), while for solution containing low Cl^- it is equal to 14 mV. All potential values were thus corrected off-line by subtracting this value.

3. Data analysis

3.1 Analysis of single cell recording

Measurements of spike parameters such as overshoot, spike rise time, inflection point and time to peak were performed off line by averaging at least 20 spikes. Measurement of motoneuron input resistance was carried out by averaging at least ten traces in which a hyperpolarizing step was delivered through the recording electrode. Input resistance was then calculated as the ratio between the averaged voltage response and the applied current (usually 0.1-0.2 nA). Similar measurements were performed to generate I-V curves, in which the averaged voltage responses to hyperpolarizing and depolarizing steps were plotted against amplitude of injected current.

In case of recurrent depolarizing responses measurement, at least ten responses were averaged and measured in terms of peak amplitude and area.

For the whole cell patch-clamp recordings input resistance was calculated by measuring the current response to 5 or10 mV hyperpolarizing steps (from V_h), from the slope of the linear part of the I/V relation obtained applying a slowly rising voltage signal (ramp test: from -80 to +20 mV, 41.7 mV/s).

3.2 Linear statistic analysis

Data were expressed as mean ± S.E.M., with "n" as the number of experiments used to calculate the mean and S.E.M. Before assessing statistical differences between groups, a normality test (Kolmagorov-Smirnov test) was performed to select parametric or non-parametric tests. For comparison between two groups of normally distributed data Student's *t*-test (paired or unpaired) for was used. Turkey-test and ANOVA were used for non-parametric values. Accepted level of significance was p=0.05.

3.3 Analysis of disinhibited rhythm

During disinhibited rhythm, bursts appeared as episodes of sustained membrane depolarization. Burst period was defined as the time between the onsets of two

consecutive bursts. Burst duration was calculated from the onset of the burst to the time point when the membrane potential crossed a curtain threshold, set at 5-10 times the standard deviation of the baseline noise (measured over 0.5-1 s during the quiescent period immediately before the onset of a burst), depending on signal-to-noise ratio conditions. Intraburst oscillation period was measured as the peak-to-peak time interval.

4. Molecular biology

4.1 Western blot

The flow chart in Figure 8 shows the protocol for immunoblotting of lumbar spinal cord and lung samples. The anti-CFTR antibody (Ab; 1: 300) against aminoacid residues 1468-1480 of the human CFTR (accession # P13569) was used with HRP-conjugated goat anti rabbit IgG 1:2000 (1 h).

4.2 RT-PCR

Total RNA was isolated from rat lumbar spinal cord and lung following the Invitrogen protocol based on Trizol extraction as schematized in Figure 8.

Figure 8.

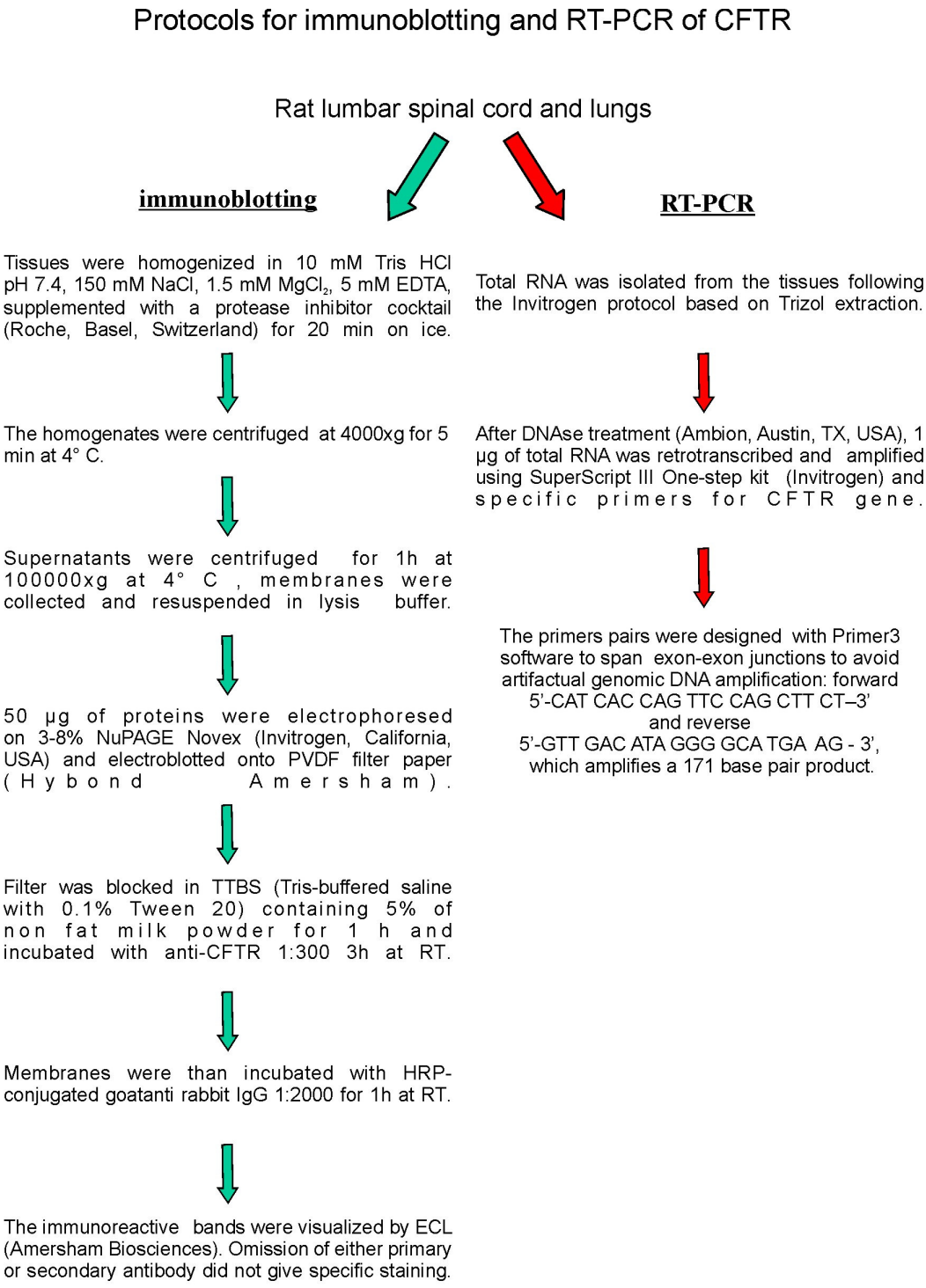
Protocols for immunoblotting and RT-PCR of CFTR
Rat lumbar spinal cord and lungs
immunoblotting
RT-PCR
Tissues were homogenized in 10 mM Tris HCl pH 7.4, 150 mM NaCl, 1.5 mM MgCl2, 5 mM EDTA, supplemented with a protease inhibitor cocktail (Roche, Basel, Switzerland) for 20 min on ice.
The homogenates were centrifuged at 4000xg for 5 min at 4° C.
Supernatants were centrifuged for 1h at 100000xg at 4° C , membranes were collected and resuspended in lysis buffer.
50 µg of proteins were electrophoresed on 3-8% NuPAGE Novex (Invitrogen, California, USA) and electroblotted onto PVDF filter paper (Hybond Amersham).
Filter was blocked in TTBS (Tris-buffered saline with 0.1% Tween 20) containing 5% of non fat milk powder for 1 h and incubated with anti-CFTR 1:300 3h at RT.
Membranes were than incubated with HRP-conjugated goatanti rabbit IgG 1:2000 for 1h at RT.
The immunoreactive bands were visualized by ECL (Amersham Biosciences). Omission of either primary or secondary antibody did not give specific staining.
Total RNA was isolated from the tissues following the Invitrogen protocol based on Trizol extraction.
After DNAse treatment (Ambion, Austin, TX, USA), 1 µg of total RNA was retrotranscribed and amplified using SuperScript III One-step kit (Invitrogen) and specific primers for CFTR gene.
The primers pairs were designed with Primer3 software to span exon-exon junctions to avoid artifactual genomic DNA amplification: forward 5'-CAT CAC CAG TTC CAG CTT CT–3' and reverse 5'-GTT GAC ATA GGG GCA TGA AG - 3', which amplifies a 171 base pair product.

5. Modeling of motoneuron structure

5.1 Model of motoneuron soma

For an appropriate soma reconstruction I chose soma representation as an ellipse rotated around its major axis (prolate spheroid). This representation has been used by Thurbon *et al.* (1998) to measure the membrane surface area. The data could not been simply introduced into the commonly used software NEURON (Hines & Carnavale, 1997) to calculate cell properties because this program represents the neuron geometry in terms of cylindrical sections. Hence, to preserve the exact volume and the membrane surface area of the soma after translation of the morphology to NEURON, the radius and the height of the equivalent cylinder were recalculated (31.61±4.74 and 16.08±2.42 μm respectively; s.d. values were calculated as a 15% of corresponding values).

5.2 Model of the axon

The axon was simulated as a series of cylindrical compartments (0.1, 0.1 and 10 μm length for the axon hillock, the initial segment and the axon itself, respectively) attached to the soma surface. This simulation was done following Luscher and Larkum (1998), because of the lack of anatomical data regarding the precise structure of a single motoneuron axon.

5.3 Model of proximal dendrites

For the purpose of reconstructing dendrites, these were represented as cylindrical segments without tapering because the original morphological studies provide only the mean diameter measured as a mean between the beginning and the end of the dendrite (Dekkers *et al.*, 1994; Thurbon *et al.*, 1998). Two points in space were used to characterize the position of the dendrite in 3D (six coordinates with 0 at the center of the soma). The source point for each proximal dendrite was placed on the surface of the soma.

5.4 Model of distal dendrites

Like the case of proximal dendrites, all other dendrites were simulated as cylinders with a fixed diameter ending whenever there was a deviation or bifurcation. The end point of a dendrite was chosen in space so that the angle between the parent and the sibling dendrites was >90 degrees. The length of dendrite was the second parameter, which limited the choice of the end point. Actual length parameters are given in the Results.

5.5 Computer simulation and analysis

The morphology of the motoneuron was modeled using MATLAB version 7.0 Release14 (The MathWorks, Inc.). The choice of each model parameters was based on the experimental mean and standard deviation values and was obtained by a standard MATLAB *randn* function generating a random distribution with a specific mean and standard deviation. In the absence of experimental data for some parameters, the choice was made on the basis of the presumable minimal and maximal values and the *rand* function was used to generate a uniform distribution of random numbers on a specified interval. Linear regression analysis was carried out with Origin 6.1 (OriginLab Corporation, Northampton, MA, USA). The Spearman's rank correlation test was used to assess statistical significance of correlation between data groups.

5.6 Simulation of electrical behavior of modeled motoneuron

Electrical behavior of modeled motoneurons was examined by exporting motoneuron morphology and voltage-sensitive current distributions into NEURON simulation environment. While simulating the electrical behavior of the motoneuron was not the aim of the present simulation, voltage-dependent ionic currents necessary for spike generation were introduced into the model to test its validity using the NEURON simulation environment (simulation step 25 μs). Following the experimental and modeling studies of Na^+, K_A and K_{dr} currents by Safronov *et al.* (1995; 2000), these currents were described using standard Hodgkin and Huxley equations (see Safronov *et al.*, 2000).

Results

1 Experimental results

1.1 Effect of glibenclamide on bicuculline evoked spontaneous activity

I first tested if glibenclamide sensitive K_{ATP} conductances could modulate bursting appearing after pharmacological antagonism by bicuculline of GABA-mediated inhibition. Bicuculline methiodide (20 μM) was applied to spinal cord preparations at a concentration fully blocking $GABA_A$ receptors (Bracci *et al.*, 1996a; Bracci *et al.*, 1996b) and too low to produce block of apamin-sensitive small-conductance K^+ channels (Johnson & Seutin, 1997; Johansson *et al.*, 2001). Bicuculline elicited spontaneous irregular activity in fifteen of fifteen preparations (Figure 9a top trace). Often a few discharges coalesced together to make up a single burst (see Bracci *et al.*, 1996a). Spontaneous activity evoked by bicuculline was characterized by changeable area, amplitude, duration of single events and inter-event interval (IEI). Each of these parameters was characterized by relatively large coefficient of variation (CV; Figure 9c). In accordance with previous data (Bracci *et al.*, 1996a) recordings performed simultaneously from two VRs revealed synchronization between different VRs (n=3; not shown).

After one hour application of bicuculline, application of the K_{ATP} channel antagonist glibenclamide (50 μM; the same concentration used for studying K_{ATP} channels in the brainstem, Pierrefiche *et al.*, 1996) significantly increased area, amplitude and duration of single spontaneous events with simultaneous increase of their IEI (Figure 9a lower trace). Figure 9b shows histograms summarizing glibenclamide effects on bicuculline evoked spontaneous activity (n=8, $p<0.05$). Surprisingly, in addition to increased spontaneous activity, glibenclamide transformed spontaneous events into a more regular pattern. Figure 9c compares CVs of area, amplitude, duration of single event and IEI in control and after glibenclamide application. All values of CVs were significantly attenuated; however, the effects on the single event parameters were

***Figure 9**. Effect of glibenclamide on bicuculline induced spontaneous activity*

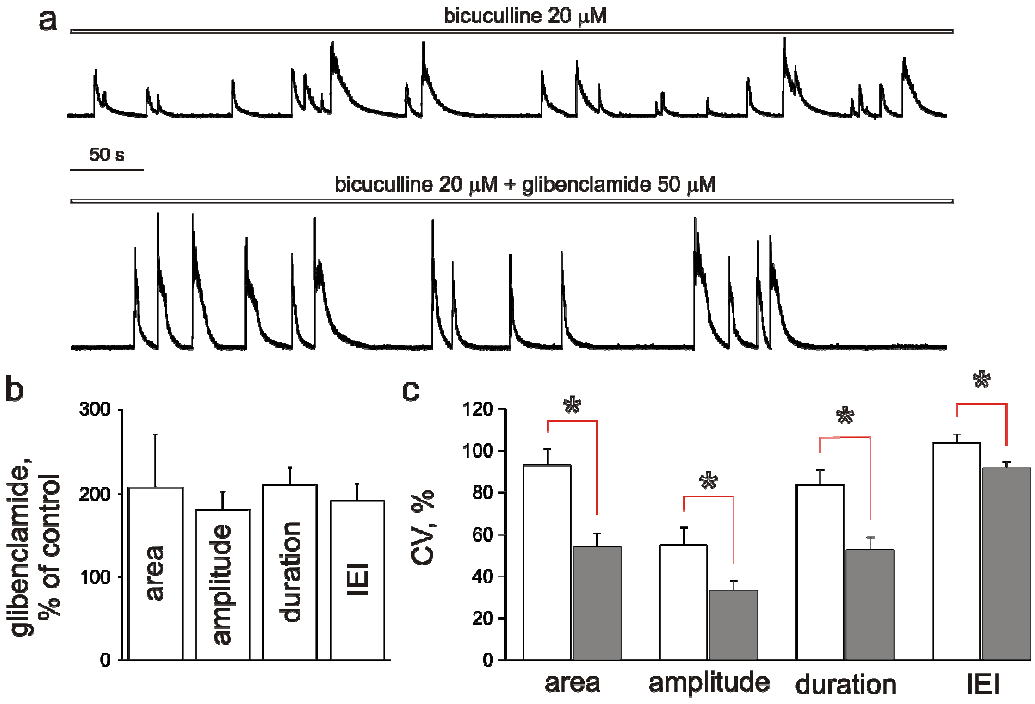

a, spontaneous activity induced by bicuculline is changed after 20 minutes of application of K_{ATP} channel blocker glibenclamide into more organized patterns. b, this effect is accompanied by significant increased size of spontaneous events and prolonged inter event intervals. c, coefficients of variation of events area, amplitude and duration as well as of inter signal intervals were significantly decreased by glibenclamide (filled bars) comparing to bicuculline alone (open bars).

higher than on the IEI. A similar effect on bicuculline induced spontaneous activity was obtained by application of another K_{ATP} channel blocker namely tolbutamide (500 μM; n=3; data not shown). While concentrations of glibenclamide in the submicromolar were ineffective, a higher concentration of glibenclamide (100 μM) applied after 50 μM did not produce effects significantly larger than 50 μM (n=5; not shown). The effects of glibenclamide and tolbutamide could not be reversed after half an hour washing with ACSF plus bicuculline. All together, these data showed that glibenclamide or tolbutamide made bicuculline evoked spontaneous activity less irregular and single events more homogeneous.

1.2 Effect of glibenclamide on the disinhibited activity

Disinhibited bursting arises from full pharmacological block of GABA and glycine mediated synaptic inhibition (Bracci *et al.*, 1996a, b). Single bursts are long, complex events endowed with oscillatory activity, during which a strong activation of K_{ATP} conductances might be expected. For these reasons, I tested glibenclamide effects on such a paradigm.

When bicuculline and strychnine were coapplied, a regular pattern of spontaneous synchronous bursts (cycle period ~30 s) developed in VRs (Figure 10a top trace) after an irregular phase lasting 10-15 minutes (not shown). Each event was composed by fast depolarization, often followed by less depolarized plateau (lasting around 1.5 s) after which large rhythmic oscillations appeared. This type of spontaneous activity is termed disinhibited bursting (Bracci *et al.*, 1996a, b; Bracci *et al.*, 1997). Glibenclamide applied after full development of disinhibited activity increased the amplitude of single bursts and the inter event interval and made disinhibited bursts less regular (Figure 10a low trace). The onset of action of glibenclamide was usually delayed for 20-30 minutes. The histograms in Figure 10b-d summarize action of glibenclamide on the bicuculline and strychnine evoked activity. The same effect was observed using tolbutamide (500 μM, not shown; n=3).

Figure 11a compares (expanded in time scale) a single spontaneous burst before (left) and after glibenclamide application (right). Glibenclamide significantly decreased the number of oscillations within the single burst (Figure 11b), while the average frequency of oscillations or the plateau duration was not changed. Moreover, the probability of detecting double bursts (doublets) with the second burst starting before the full termination of the preceding one (red example in Figure 11a) was increased (histograms in Figure 11d). Thus, the effects of glibenclamide on disinhibited activity could be summarized as a disinhibited rhythm perturbation with increased probability to transform a single burst into a doublet. The same effects were seen after application of tolbutamide 500 μM (not shown). However, rhythmicity of disinhibited activity and composition if single events could be restored by application of NMDA (5 μM) or increased extracellular concentration of KCl (7.5 mM from usual 4.5 mM). Figure 12 shows two traces representing the action of these depolarizing substances.

Figure 10. *Effect of glibenclamide on strychnine and bicuculline evoked rhythmic activity*

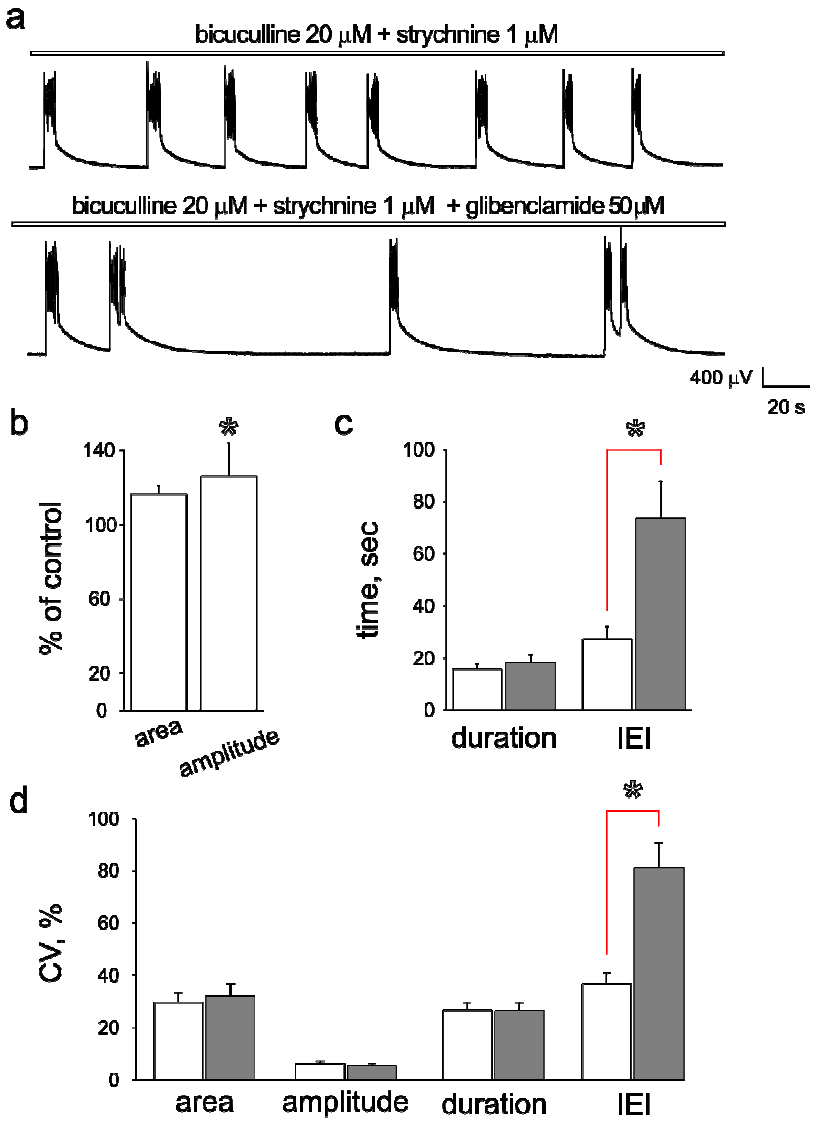

Application of 50 μM glibenclamide perturbed regular rhythmic activity evoked by bicuculline and strychnine (a). Amplitude and area (b) of single burst and inter event interval were significantly increased by glibenclamide (c), while duration of the burst was unchanged (c). Although variability of the area, amplitude and duration of disinhibited bursts was preserved after glibenclamide application, the inter event intervals coefficient of variability was significantly increased (d). Open bars-control; filled bars-glibenclamide.

Figure 11. *Effect of glibenclamide on single disinhibited burst*

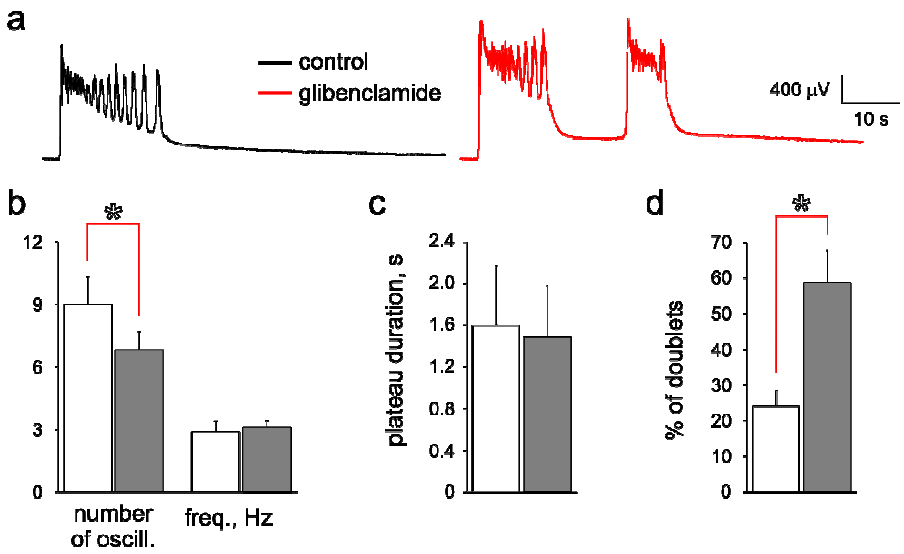

a, control (black) and glibenclamide transformed (red) single disinhibited bursts recorded from VR. Although glibenclamide decreased number of oscillations (b) and increased probability to detect doublets (d), it did not change frequency of interburst oscillations (b) and duration of the initial plateau phase of each single burst (c).

Figure 12. *NMDA and high extracellular KCl restored regular rhythmicity disturbed by glibenclamide*

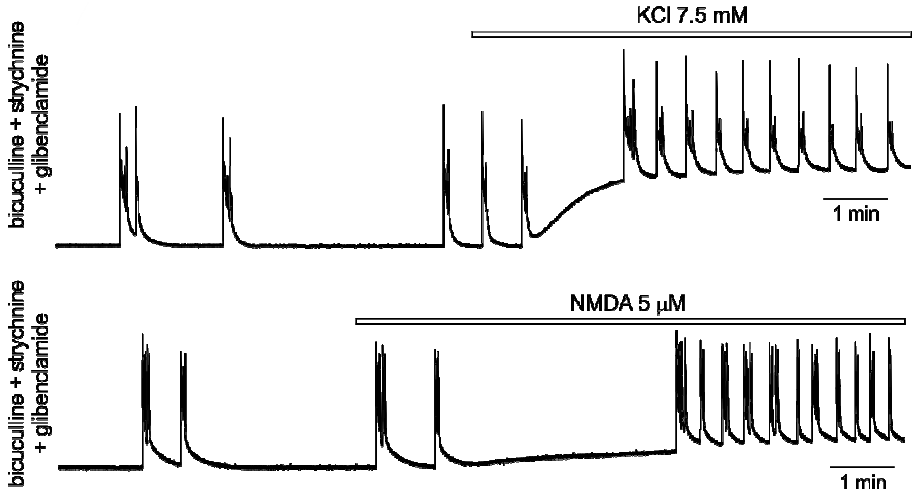

Trace on the top shows effect of higher extracellular KCl (7.5 mM from 4.5 mM) concentration on the disinhibited rhythm after glibenclamide. Note depolarizing effect of higher KCl concentration and highly periodic occurrence of bursting on the plateau phase of this depolarization. Effect similar to high KCl was obtained by bath application of NMDA (5 µM). Depolarization produced by NMDA restored disinhibited rhythmicity.

1.3 DR evoked responses

After studying the glibenclamide effect on the properties of the disinhibited activity and obtaining surprising results which did not readily accord with the action of glibenclamide as the K^+ channel blocker, we examined if glibenclamide had any effects on standard synaptic transmission evoked by electrical stimulation of a single DR. Although concentrations of glibenclamide in the submicromolar range were ineffective (not shown), averaged monosynaptic and polysynaptic responses evoked by weak (1 x Th) or strong (>1 x Th) DR stimulation (Marchetti *et al.*, 2001a) were enhanced by 50 μM glibenclamide as exemplified in Figure 13a (monosynaptic responses are depicted in the inset). The drug was applied for 20 min to ensure steady state effects after tissue equilibration as shown in Figure 13b in which changes in the polysynaptic response area and peak are plotted versus time (glibenclamide application indicated by horizontal bar). Figure 13c quantifies the facilitating effects of 50 μM glibenclamide on the size of mono and polysynaptic responses. Although the largest increment was observed for responses to weak stimuli, all responses were significantly increased, regardless of the stimulus intensity. Lower concentrations (1-10 μM) of glibenclamide were ineffective (5±10 % change in response amplitude; $p>0.05$; $n=4$).

Figure 14a shows VR response to the high frequency (1 Hz) strong stimulation (4x Th) of a single DR in control (black) and after developed action of glibenclamide (red). As shown in Figure 14b, glibenclamide significantly increased cumulative response, but at the same time speeded up decay time.

Since the effects of glibenclamide implied changes in network activity, we next investigated spinal network output following changes in excitability due to application of neurotransmitter agents (Kerkut & Bagust, 1995). Thus, we recorded VR DC depolarizations evoked by NMDA (20 μM), AMPA (20 μM), GABA (500 μM) or glycine (500 μM) on the same preparations. Figure 15 shows that depolarizations to NMDA or AMPA (bottom example in panel a) were significantly increased, whereas depolarizations to GABA (top example in panel a) or glycine were significantly depressed (histograms in Figure 15b summarize these effects of glibenclamide).

Figure 13. *Glibenclamide enhances spinal circuit excitability*

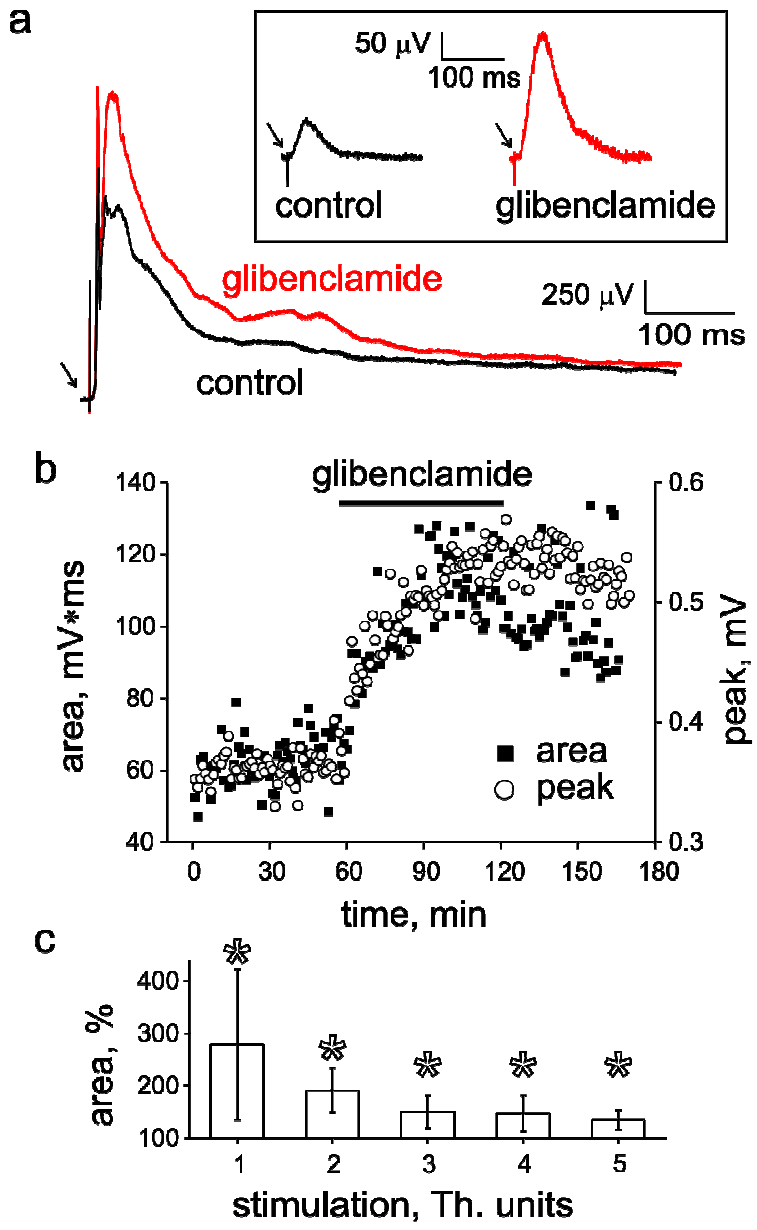

a, monosynaptic (inset) and polysynaptic responses evoked by weak (1 x Th) or strong (4 x Th) DR stimulation, respectively, and recorded from a lumbar VR are increased after 20 min application of 50 µM glibenclamide. Responses are averages of 5-50 events. b, time-course of glibenclamide evoked increase in area and peak amplitude of polysynaptic reflexes. Note that 20 min exposure was adequate for observing steady state effects. c, histograms plotting VR reflex area (% of control) for different DR stimulus intensities in the presence of glibenclamide (50 µM). For each one of the stimulation intensities (n=8 preparations), a significant ($p<0.05$) increase in response area was observed.

Figure14. *Glibenclamide increases cumulative depolarization amplitude while speeds up decay time*

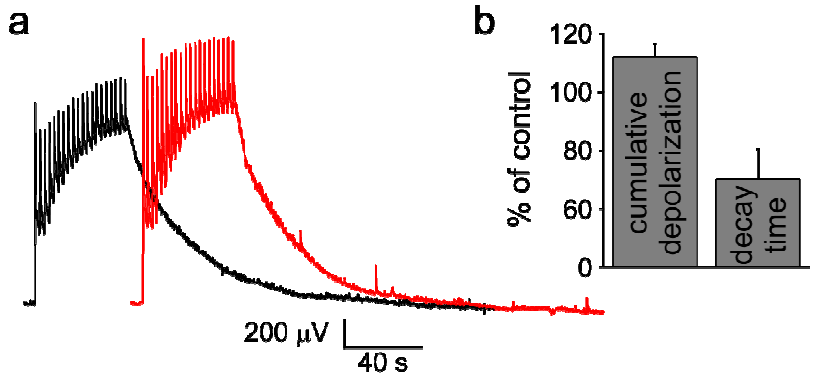

a, cumulative response recorded from VR and elicited by high frequency (1 Hz) strong (4x Th) DR stimulation in control (black) and after application of glibenclamide 50 µM (red). Histograms (b) summarize effect of glibenclamide on the cumulative depolarization amplitude and decay time of the signal (n=8; all changes are significant, $p<0.05$).

Figure 15. *Contrasting effects of glibenclamide on depolarization evoked by excitatory and inhibitory substances*

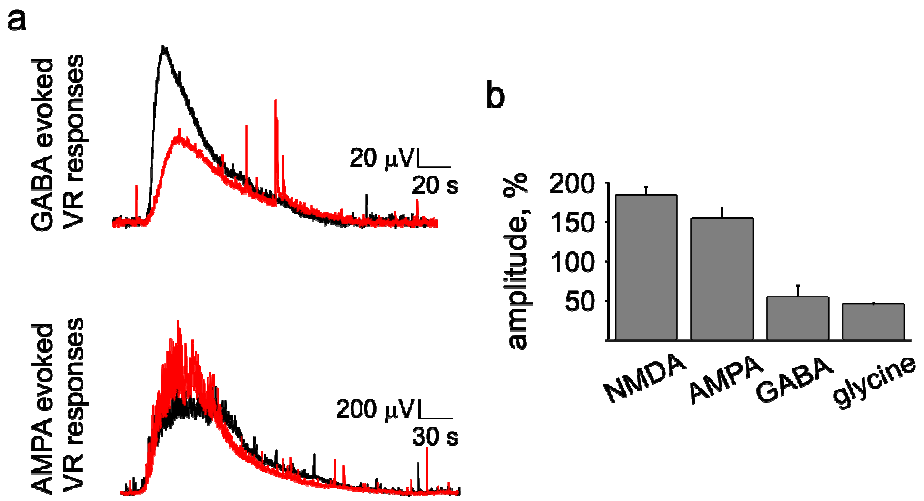

a top, in black depolarization of the VR recorded after bath application of 500 µM GABA in control is attenuated after application of 50 µM glibenclamide (red). In the bottom of panel a, examples of the depolarization evoked by bath application of NMDA in control (black) and in 50 µM glibenclamide solution (red) are shown. Histograms (b) of VR depolarization amplitude (as % of control) evoked by 25 s bath application of NMDA (20 µM) or AMPA (20 µM) which was significantly ($p<0.05$) enhanced by glibenclamide, while GABA (500 µM) or glycine (500 µM) evoked depolarizations were significantly depressed ($p<0.05$; n=5).

1.4 Motoneuron electrophysiology

The glibenclamide-dependent changes in synaptic transmission and the differential alterations in responses to excitatory or inhibitory amino acid agonists suggested a complex modulation of transmitter receptor function which was further explored with intracellular recording from single motoneurons. In particular, while monitoring effects from the same cell, it was possible to compare changes in the EPSP induced by DR stimulation with changes in the recurrent IPSP evoked by antidromic stimulation of the corresponding VR (Marchetti *et al*., 2002; Marchetti *et al*., 2005). This protocol allowed gaining detailed information on the properties of excitatory and inhibitory neurotransmission on motoneurons.

Figure 16a shows that, on a single motoneuron, glibenclamide depressed the recurrent IPSP, whereas it enhanced the monosynaptic EPSP elicited by low-threshold DR stimulation. This contrasting condition is quantified in Figure 16b in which the large potentiation of the EPSP stood against the significant fall in the IPSP amplitude.

In addition to such changes in synaptic physiology, I also investigated if glibenclamide could alter some basic electrophysiological properties of motoneurons. To this end, pharmacological block of synaptic transmission with kynurenic acid (3 mM), bicuculline (20 μM) and strychnine (1 μM) eliminated contributions by network-distributed glibenclamide-sensitive conductances Under these conditions, as shown in Figure 17a, glibenclamide slowly hyperpolarized the motoneuron membrane potential (on average by 3.0±0.9 mV; n=11; $p<0.007$) with increased input resistance (29±10 %; n=11; $p<0.003$) as exemplified by the larger amplitude of the hyperpolarizing electrotonic potentials evoked by intracellular current pulses (Figure 17b). Analogous results (25±5 % rise in input resistance) were obtained with tolbutamide (500 μM; n=13), a K_{ATP} channel blocker weaker than glibenclamide. Together with membrane hyperpolarization and resistance increase, there was intermittent failure of action potential generation due to membrane hyperpolarization as indicated in Figure 17a.

Figure 18a shows that glibenclamide increased the slope of the voltage/current curve throughout the range of tested membrane potential values. Under the current clamp condition this change is equal to increase in the motoneuron input resistance. The action of glibenclamide was associated with augmented peak amplitude of the spike (3.6±1.1 mV; n=11; $p<0.009$) even when the cell membrane potential was

Figure 16. *Contrasting effects of glibenclamide on motoneuron IPSP and EPSP*

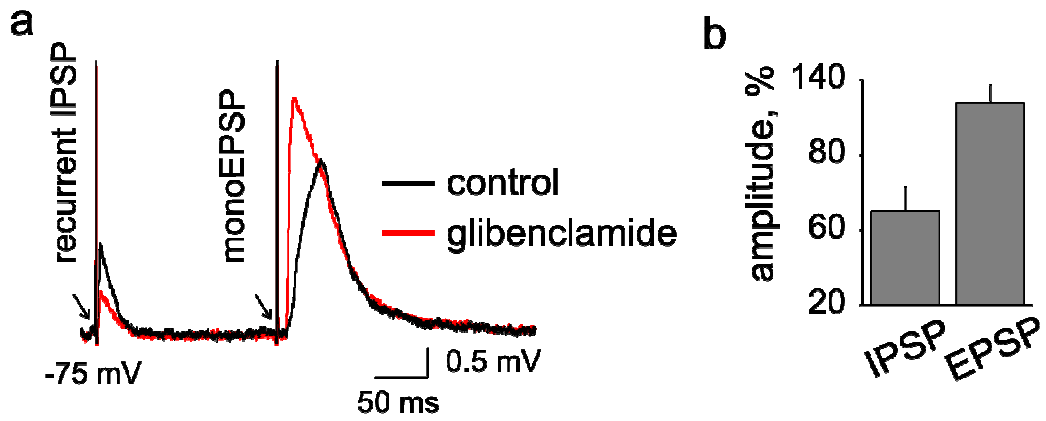

a, intracellular recording from single motoneuron showed opposite changes in recurrent IPSP (evoked by VR stimulation; first response) and monosynaptic EPSP (second response). Value at the start of trace indicates membrane potential, while fast upward deflections are the stimulus artefacts. The EPSP had longer latency because of the longer distance between stimulation site and recorded cell. b, histograms depict average fall in recurrent IPSP amplitude with rise in mono EPSP amplitude ($p<0.05$; $n=8$).

repolarized to control level (Figure 18b). When plotting for the same cell, the spike overshoot and the resistance increase, there was a close correlation (r=0.89) as depicted in Figure 18c. Although Table 2 shows that other spike parameters were unchanged, motoneuron firing was facilitated by glibenclamide as shown by the greater number of spikes fired for the same current pulse (Fig. 18d) and quantified in Figure 18e (n=6).

These data collectively showed a glibenclamide-evoked gradual rise in motoneuron excitability associated with membrane hyperpolarization and spike augmentation which could not be accounted for by a block of spike-dependent K^+ currents. This set of results prompted us to consider a constitutively-active mechanism regulating background conductance.

Figure 17. *Motoneuron hyperpolarization together with increase in antidromic spike overshoot and input resistance following glibenclamide application*

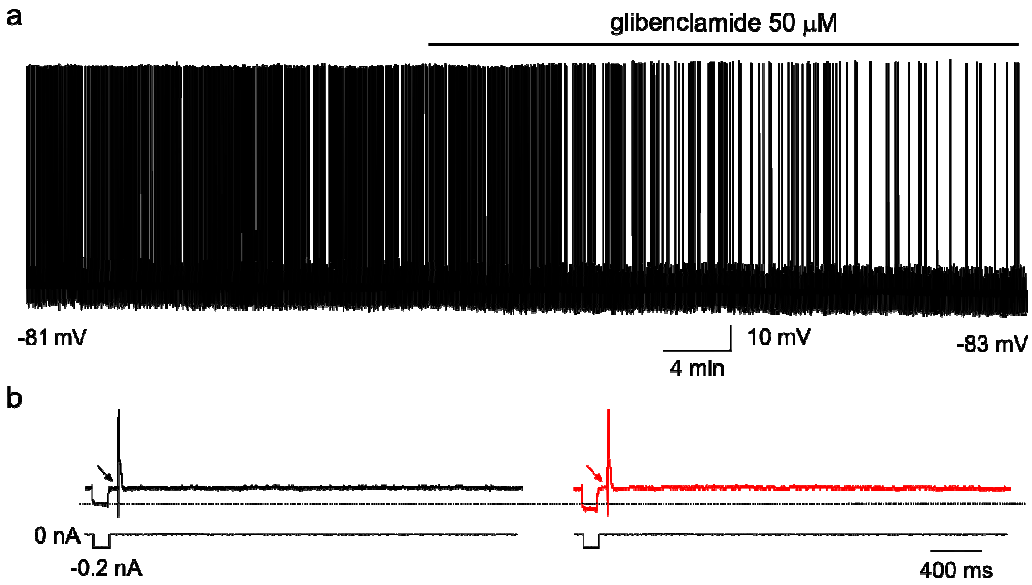

a, intracellular recording from single motoneuron (initial resting potential = -81 mV; large deflections are antidromic spikes) to which glibenclamide was applied as indicated by the horizontal bar. Note gradual membrane hyperpolarization to -83 mV plus increase in spike amplitude and occasional spike failure. b, faster speed traces show electrotonic potentials induced by -0.2 nA pulses to measure input resistance followed by VR stimuli to evoke antidromic spikes (truncated). Note absence of spontaneous synaptic events due to the use of Krebs solution containing synaptic receptor blockers (3 mM kynurenic acid, 2 µM strychnine, 20 µM bicuculline). Voltage calibration as in a.

Figure 18. *Changes in motoneuron properties after application of glibenclamide*

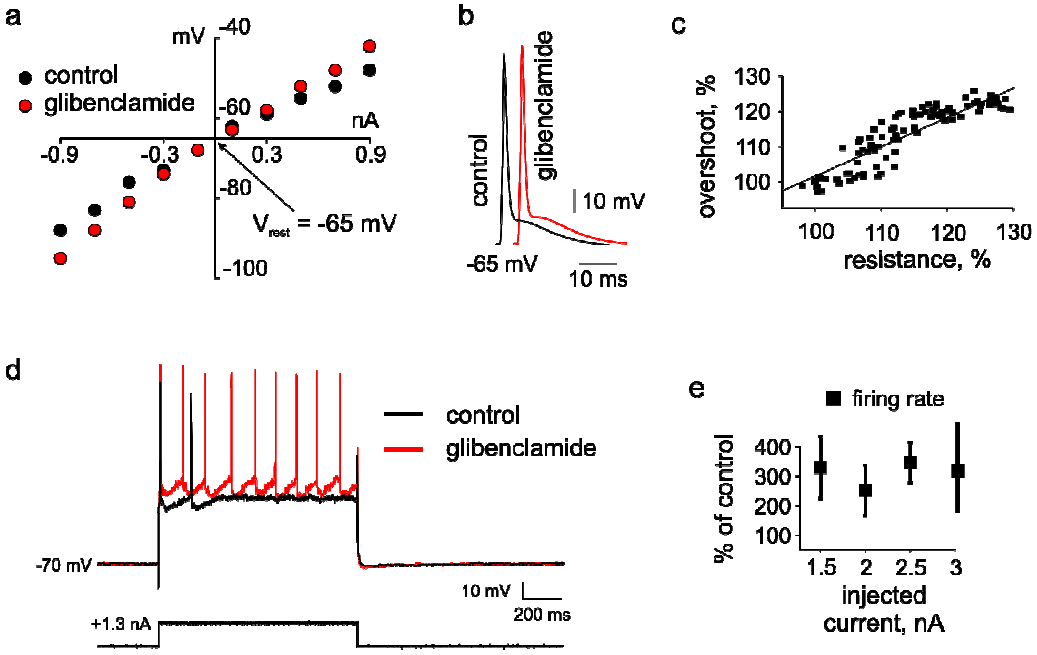

a, voltage/current plot shows increased slope indicating rise in membrane resistance produced by glibenclamide. b, larger spike overshoot in the presence of glibenclamide persisted even after cell repolarization to control membrane potential, while the other spike parameters were unchanged. Value indicates membrane potential. c, strong correlation between rise in overshoot and resistance increase (r=0.89; n=8 cells). Data are expresses as % increment over control. d, superimposed records from the same motoneuron in control or glibenclamide solution. At the same level of membrane potential (-70 mV; 0.2 nA current injected during application of glibenclamide), in control solution the cell fired two action potential in response to intracellular current injection, whereas it generated nine spikes in the presence of glibenclamide. e, plots showing that glibenclamide increased the firing rate (ordinate) of motoneurons during injection of 1 s current pulses of varying amplitude (abscissa). Each data-point shows similar % increment versus control ($p<0.05$; n=6).

Table 2. *Effects of glibenclamide (50 μM) on electrical properties of motoneurons*

parameter	*control*	*glibenclamide*	*P value*
V_{rest}, mV	−72 ± 1.4	−75 ± 1.3	0.007 *
R_{in}, MΩ	21 ± 1.8	25 ± 2.4	0.03 *
overshoot, mV	15 ± 1.2	19 ± 1.1	0.009 *
spike rise time, ms	1.3 ± 0.1	1.3 ± 0.1	0.98
inflection point, mV	−47 ± 1.6	−46 ± 1.5	0.6
time to peak, ms	3.3 ± 0.2	3.5 ± 0.2	0.1
stimulus threshold, V	0.6 ± 0.1	0.6 ± 0.1	0.09

Mean ± S.E.; n =11; V_{rest} = resting membrane potential; R_{in} = input resistance; * = statistically significant difference. Inflection point is measured at the break between initial segment and somatodendritic spike.

Because the excitability of rat spinal neurons is powerfully controlled by the electrogenic Na^+-K^+ pump (Ballerini *et al.*, 1997; Rozzo *et al.*, 2002), and the effects of glibenclamide might have been secondary to K^+ buffering, the potent Na^+-K^+ pump blocker strophanthidin was applied before glibenclamide. Figure 19a shows that strophanthidin evoked motoneuron depolarization (Ballerini *et al.*, 1997; Rozzo *et al.*, 2002) with antidromic spike failure at -51 mV (see inset). This effect was reverted to hyperpolarization to -75 mV (with return of spike generation and emergence of synaptic activity) by subsequent application of glibenclamide. Figure 19b demonstrates that, on average, glibenclamide significantly hyperpolarized the membrane potential despite block of the Na^+-K^+ pump.

Figure 19. *Glibenclamide affects motoneuron excitability even when the Na^+-K^+ pump was pharmacologically blocked*

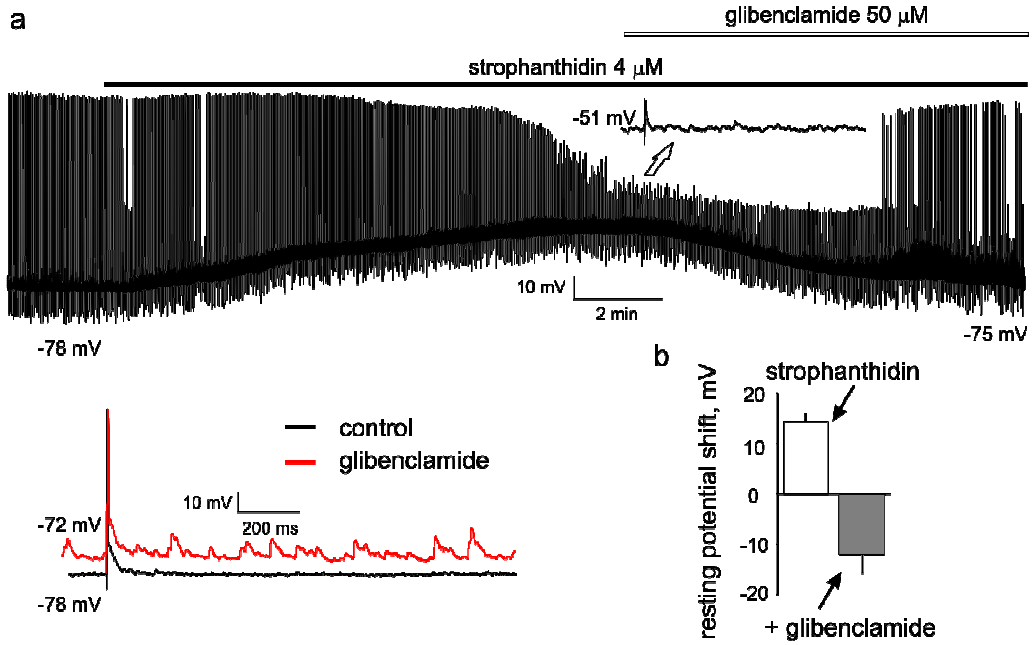

a, top trace shows intracellular recording from motoneuron (resting potential of -78 mV with full antidromic spike; see expanded trace indicated with open arrow) slowly depolarized by strophanthidin to -51 mV with associated spike failure (see inset) because of membrane depolarization. Application of glibenclamide (open bar) repolarized the membrane potential to -75 mV with return of antidromic spike and emergence of spontaneous synaptic events (see bottom a, black control, red glibenclamide). b, histograms showing average change in membrane potential obtained after 20 min application of strophanthidin (with respect to resting membrane potential taken as 0 mV), and 40 min strophanthidin plus 20 min glibenclamide application (with respect to potential attained in the presence of strophanthidin). Both values significantly ($p<0.05$; $n=6$) differ from control. The larger effect of glibenclamide in the presence of strophanthidin might be explained by recovery of voltage-dependent channels from deactivation occurring at -50 mV.

Other important action of glibenclamide is to block the so-called cystic fibrosis transmembrane conductance regulator (CFTR; Sheppard *et al.*, 1992; Schultz *et al.*, 1999), a membrane protein involved in Cl^- transport in a variety of epithelia cells, particularly in the lungs (Sheppard & Welsh, 1999; Nilius & Droogmans, 2003), whereas it is supposed to be minimally expressed in the central nervous system (Mulberg *et al.*, 1994; Hincke *et al.*, 1995). We considered the possibility that glibenclamide might have produced its electrophysiological actions by blocking CFTR rather than K_{ATP} channels. We thus tested if the selective CFTR inhibitor DPC (500 μM; Schultz *et al.*, 1999) mimicked the action of glibenclamide on motoneurons. Figure 20a shows that bath-applied DPC gradually hyperpolarized the

Figure 20. *DPC changes resting and spike properties of motoneurons*

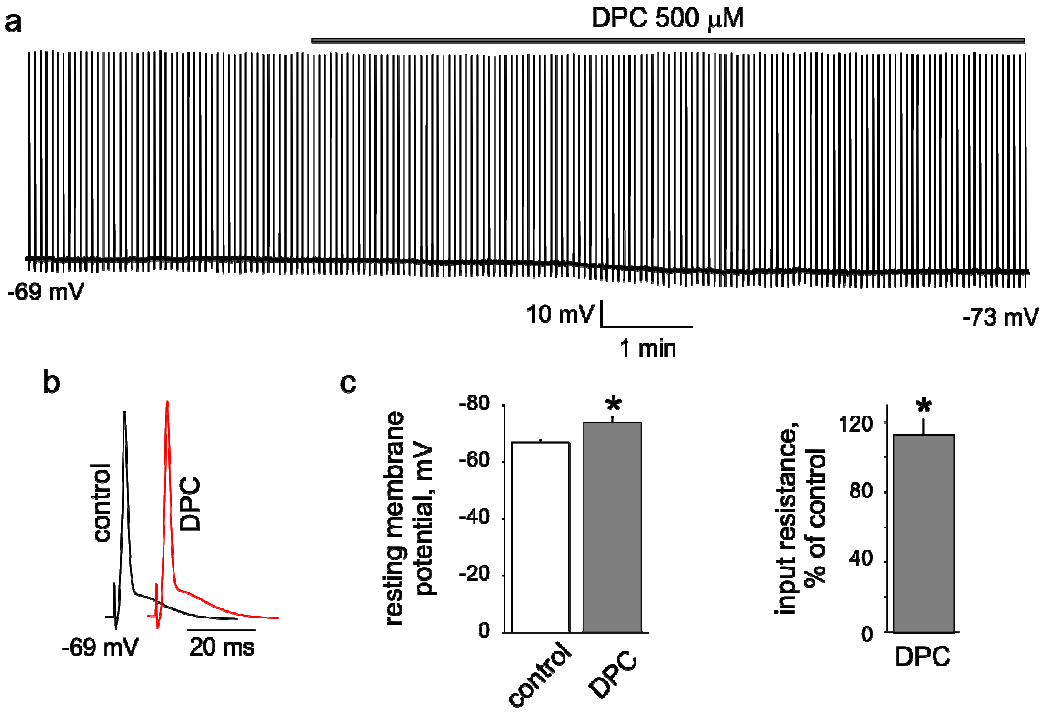

a, continuous intracellular record from motoneuron shows gradual hyperpolarization of membrane potential from -69 to -73 mV following application of DPC. b, antidromic spike of the same motoneuron in control and after applying DPC (each response is an average of >20): for the same level of membrane potential (obtained by injecting 0.3 nA depolarizing current) there is a large increment in the spike peak. c, histograms indicating the hyperpolarization in resting membrane potential (left) and the input resistance increase (right) observed after applying DPC (n=5).

motoneuron membrane potential, an effect accompanied by enhanced height of the antidromic spike (Figure 20b). On average, DPC significantly increased the membrane potential and resistance of motoneurons as indicated in Figure 20c (n=5). These data therefore demonstrated identical action of glibenclamide and DPC on spinal motoneurons.

1.5 Cl^- dependent inhibition

On immature neurons, experimental and theoretical studies show that $GABA_A$ receptors mediate membrane depolarization via increased Cl^- permeability and minimal HCO_3 contribution (Cupello, 2003). Hence, it is possible to use responses evoked by synaptic inhibition or exogenously-applied GABA to estimate if glibenclamide might

Figure 21. *Glibenclamide-evoked change in reversal potential of recurrent IPSCs of motoneurons*

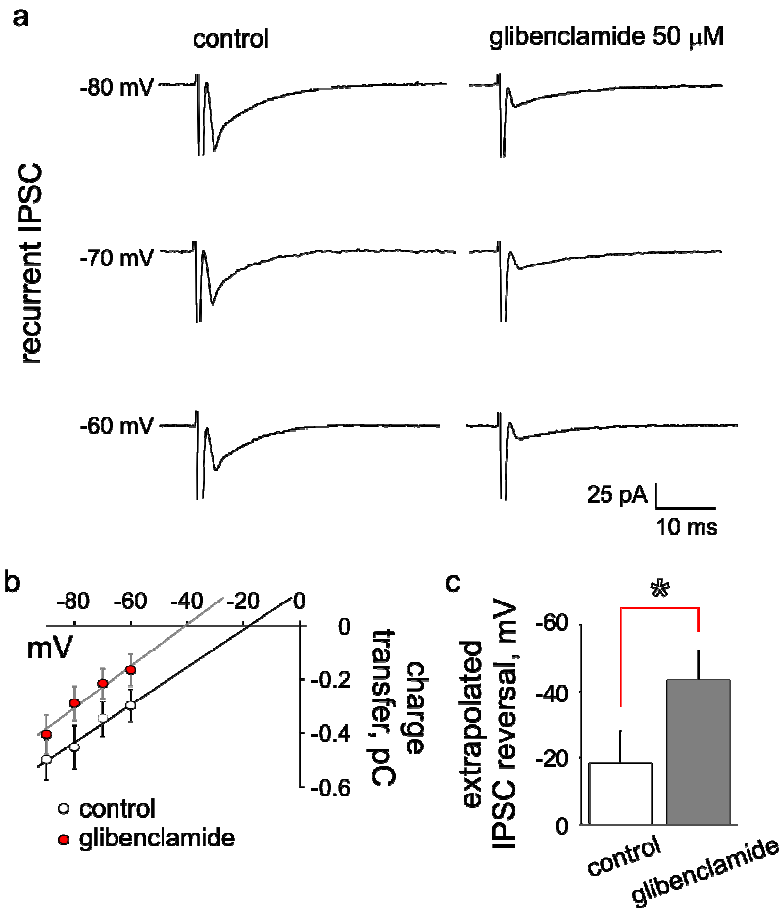

a, examples of recurrent IPSCs (average from 150 responses) at three levels of holding potential under voltage clamp conditions. Note depression of IPSC with glibenclamide application (25 min). b-c, plots show charge transfer/voltage relations for control (open circles) or glibenclamide (filled circles) responses with histograms indicating the negative shift of the extrapolated E_{Cl^-} value ($p<0.05$; n=6).

have changed the E_{Cl^-} and, consequently, neuronal excitability. First, on motoneurons, we used sharp electrode (filled with Cs_2SO_4) voltage clamping (Fisher & Nistri, 1993) to estimate changes in the Renshaw cell-mediated IPSC recorded with sharp electrodes to minimize disturbance to the intracellular ionic milieu. Figure 21a shows that the depression of motoneuron IPSCs by glibenclamide was associated with a significant shift (on average -25±4 mV, n=5) in the extrapolated IPSC reversal potential (see Figure 21b, c). Such a depolarized E_{Cl^-} value can be explained by the early postnatal age of the rats and use of intracellular Cs^+ to block of the K^+ leak currents (Rivera *et al.*, 2005).

The limited current passing ability of sharp microelectrodes constrained the range of membrane potentials to be explored under voltage clamp conditions. Furthermore, the question next arose as to whether the observed changes induced by glibenclamide were cell specific and thus restricted to motoneurons. Lamina X interneurons make monosynaptic contacts on motoneurons and are mainly responsible for synaptic inhibition subserving the rhythmic alternation of motor discharges at intrasegmental level (Birinyi *et al.*, 2003; Kiehn, 2006). Thus, I investigated lamina X interneurons using whole cell patch-clamp configuration. These interneurons make monosynaptic contacts on motoneurons and are responsible for synaptic inhibition subserving the rhythmic alternation of motor discharges (Birinyi *et al.*, 2003). On such interneurons, brief pulses of GABA induced inward currents reversing at -46±1 mV (n=8), which is close to calculated reversal potential. On 4/8 cells glibenclamide produced a small outward current (6±2 pA) at -60 mV, increased the input resistance by 51±20 %, and shifted the GABA reversal potential by -4±1 mV. Figure 22a shows examples of responses to puffer-applied GABA (from -45 to -60 mV potential) in control (left) and after 20 min glibenclamide application (right). The charge transfer plot (Figure 21b) depicts the negative shift in the GABA reversal potential after glibenclamide treatment (see significant change in GABA current reversal in Figure 22c). Collectively, these results suggested that the reduced amplitude of Cl^- mediated IPSPs or GABA-evoked currents was caused by a glibenclamide-dependent perturbation of E_{Cl^-}.

1.6 Activation of CFTR of interneurons

Cystic fibrosis transmembrane conductance regulator is a cyclic AMP activated Cl^- channel, thus I checked activation of this channel in the spinal interneurons by intracellular application of cAMP. On lamina X interneurons (patch-clamped in thin slice preparations), we activated CFTR by including, in the patch solution, the cAMP analogue 8-bromo-cAMP (400 µM; Schultz *et al.*, 1999). As shown by the example of Figure 23a, shortly after patch breakthrough, the interneuron generated a slow inward current which stabilized at -109 pA (calculated from the initial resting current adjusted close to 0 pA by holding membrane potential immediately after establishing whole cell configuration). On average, the 8-bromo-cAMP induced inward

Figure 22. *Glibenclamide-induced changes in GABA-evoked currents recorded from spinal interneurons*

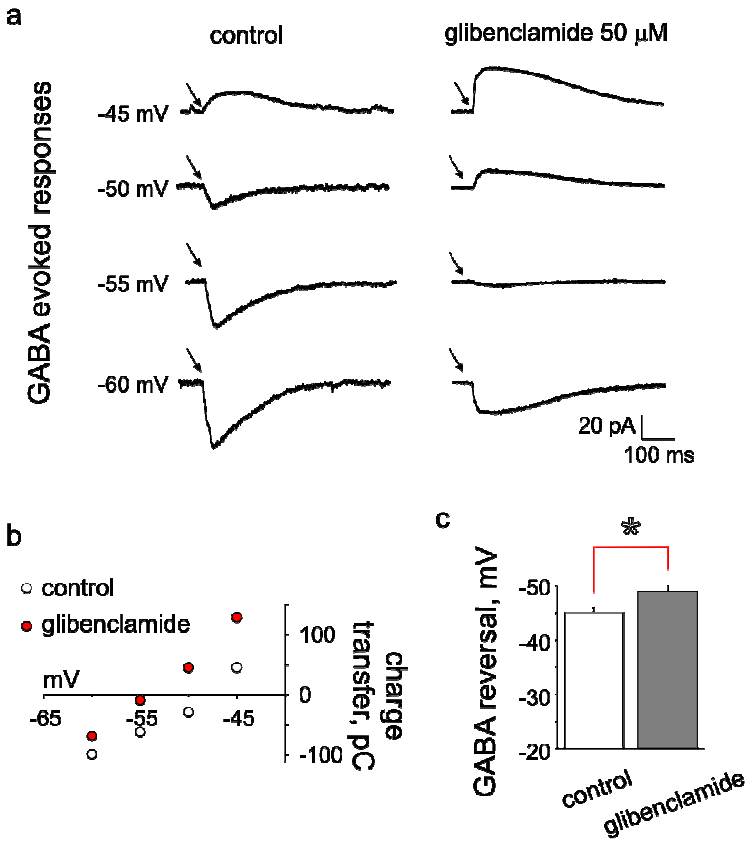

a, examples of membrane currents evoked by puffer applied GABA (arrows) at different holding potentials (from -45 to -60 mV) before (left; control) and after glibenclamide treatment (20 min; right). Prolonged kinetics of the responses is due to the increased input resistance and thus summation of the inputs from distal receptors. b, plot of changes in GABA-evoked charge transfer versus holding potential in control (open circles) and after glibenclamide application (filled circles). Data-points are from the same neuron shown in a. c, histograms showing negative shift in GABA current reversal value in the presence of glibenclamide (n=4; $p<0.05$).

current was -126±25 pA (n=6) associated with an input resistance decrease to 57±12 % of the value recorded immediately after breakthrough. The recently discovered inhibitor of CFTR, namely the thiazolidinone $CFTR_{inh}$ -172 (5 µM; Thiagarajah *et al.*, 2004; Figure 23b), was bath-applied and partly reversed the effect of 8-bromo-cAMP (Figure 23c). On average, with respect to the effects observed in the presence of 8-bromo-cAMP, the outward current evoked by $CFTR_{inh}$ −172 was 66±7 pA (n=5) with a resistance increase (125±11 %); both effects were reversible after 10 min washout.

Figure 23. *The CFTR inhibitor CFTRinh-172 reverses the action of 8-bromo-cAMP on interneuron*

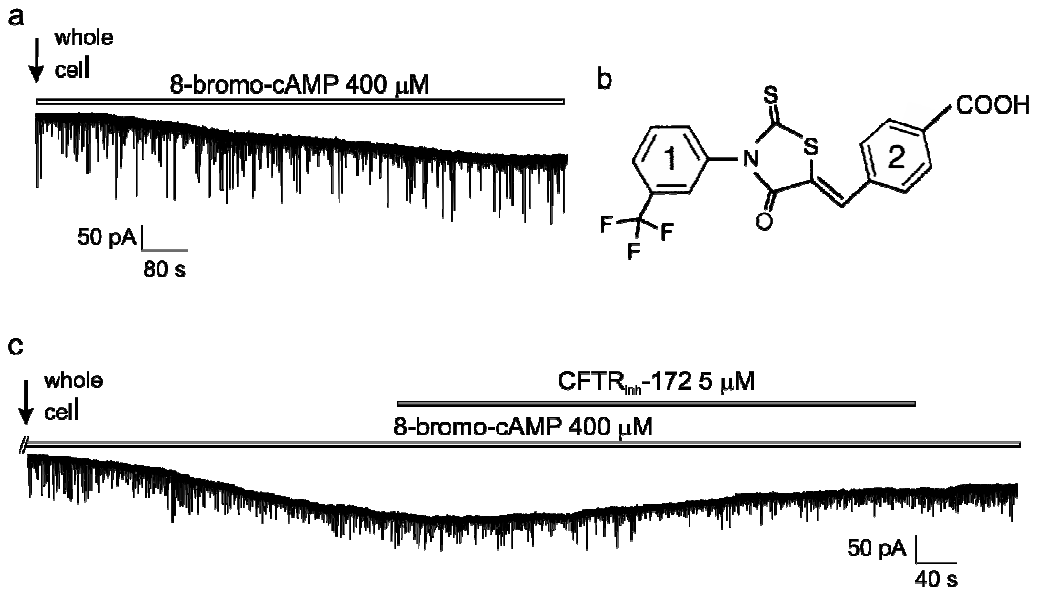

a, voltage clamp trace (under whole cell patch clamp configuration; V_h -60mV) of spinal interneuron recorded with an electrode containing 8-bromo-cAMP. Note that shortly after establishing the whole cell configuration (arrow), there is a slowly developing inward current. b, chemical structure of 2-thioxo-4-thiazolidinone CFTR inhibitor 172 (modified from Ma *et al.,* 2002). c, slowly developing inward current induced by 8-bromo-cAMP is antagonized by CFTRinh-172.

1.7 CFTR in the neonatal rat spinal cord

These experiments used mRNA extracted from rat lung (a tissue enriched in CFTR expression; Jentsch *et al.*, 2002) and lumbar spinal cord which contained a 170 nucleotide-long band (lanes 1 and 2) corresponding to the expected size of the CFTR amplified sequence (Figure 24a). As control for adequate DNA amplification, total mRNA was incubated with actin-specific oligonucleotides (lanes 3 and 4 for spinal cord and lung, respectively). The relative preponderance of CFTR mRNA in the spinal cord versus the lung one was estimated (after normalization with actin) to be 77±3 % of the lung value (n=3).

Membrane fractions of rat lumbar spinal cord or lungs showed strong pattern of CFTR immunoblotting (Figure 24b, lanes 2-3) with bands at 180 kDa and 200 kDa, corresponding to un-glycosilated and glycosilated CFTR (Mulberg *et al.*, 1994; Hincke *et al.*, 1995). Preincubation of the CFTR Ab with its immunogenic antigen

eliminated Western blot signals from lung and spinal membrane fractions (Figure 24b, lanes 4-5). Likewise, no signal was observed with NIH 3T3 cell samples (Figure 24b, lane 1). Densitometric estimates of CFTR expression indicated that the heavier band from lungs was 41±5 % (n=11) of the spinal tissue signal, while the lighter band was less expressed in the spinal cord (10±2 %) than in lungs.

Immunocytochemical staining of rat spinal cord sections with the fluorescent-conjugated anti-CFTR Ab revealed diffuse positivity, particularly intense in the nucleus of neurons (Figure 25), although the nucleus of lung epithelial cells was surprisingly unstained. A BLAST search indicated that the rat epitope recognized by the CFTR Ab had 80 % sequence homology with the nuclear receptor co-repressor 2 (accession # NP035554), a nuclear factor (molecular weight of 270 kDa; van der Laan *et al.*, 2005) that regulates transcription of development-related genes in the rat brain (Martinez de Arrieta *et al.*, 2000). This observation precluded the use of this Ab to map CFTR immunoreactivity in the spinal cord, though it did not invalidate the western blot data as confirmed by the largely different molecular weight and the tests with cell membranes which do not contain this co-repressor (Figure 24b).

The usefulness of the mouse anti-CFTR antibody CF3 was subsequently explored. This antibody recognizes a different epitope of the protein and was tested on sections of the neonatal mouse spinal cord. Again, this CFTR antibody displayed strong non-specificity by cross-reacting with other mouse proteins, precluding the identification of the CFTR neuronal location. Unlike the rat antibody, the mouse one had poor activity even on lung specimens which are the prototypic tissue for CFTR expression. Further enquiries with the antibody manufacturers (Alexis, Lausanne, Switzerland) indicated, to our surprise, that the effectiveness of this antibody had not been tested on tissues, but only on cells in culture or host expression systems for CFTR (Pier *et al.*, 1997). Thus, to the best of our knowledge, it is not currently feasible to perform reliable immunocytochemistry of CFTR expression in the spinal cord of either rat or mouse.

Figure 24. *Presence of CFTR in spinal cord tissue*

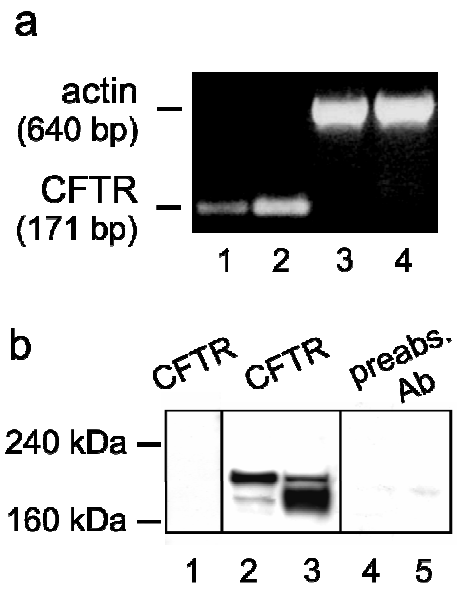

a, RT-PCR analysis for the presence of CFTR mRNA in rat lumbar spinal cord (lane 1) and lung (lane 2). The predicted fragment of 171 bp for CFTR mRNA is present in both lanes. Lanes 3-4 shows mRNA signal for actin from spinal cord and lung, respectively. bp=base pair. b, expression of CFTR protein in membrane extracts from rat lumbar spinal cord (lane 2) and lung (lane 3); NIH 3T3 membranes were used as negative control (lane 1). Peptide-inhibited samples are shown in lanes 4-5 for spinal and lung membranes, respectively.

Figure 25. *Immunofluorescence staining of lumbar spinal sections by neurofilament subunit H (NF-H) and CFTR Abs*

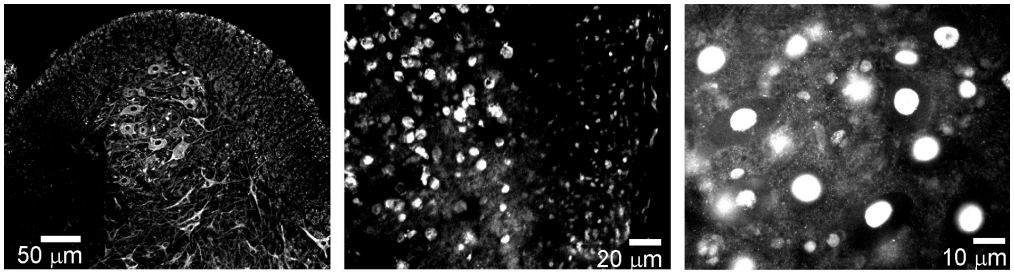

Sections of a ventral horn from lumbar spinal cord were stained with the anti-NF-H Ab SMI32, a widely used marker for spinal motoneurons (left panel). The lateral part of a ventral horn stained with the CFTR Ab shows extensive immunoreactivity (middle panel). Higher magnification (right panel) shows clear, intense nuclear staining by the CFTR Ab in ventral horn neurons.

2 Modeling results

The first part of the present study has shown experimental evidence for the complex regulation of excitability, synaptic inhibition and network activity by CFTR (for the discussion of the potential effect of sulphonylureas on the K_{ATP} channels see Discussion below). The mechanisms of this regulation is partly due to alterations in the E_{Cl^-}, and thus in the ability of GABA (and glycine) to operate as inhibitory neurotransmitter. Although GABA and glycine mediated responses at early stages of development have depolarizing appearance they produce inhibition (Marchetti *et al.*, 2002). It seems important to consider not only conductance of these channels but also dendritic distribution of inhibitory synaptic inputs to understand mechanism of GABA-ergic and glycinergic inhibition during early postnatal life. Previous morphological, electrophysiological and modeling studies revealed that dendrites are electrically and chemically distributed nonlinear units and that this has important consequences for interpreting experimental data and for the role of neurons in information processing (review Segev & London, 2000). Thus development of the morphologically realistic model of the spinal motoneurons is the first step to understand complex behavior of motoneurons which receive hundreds of both excitatory and inhibitory inputs. The second part of my thesis is dedicated to the description of the model which describes 3D structure of the developing spinal motoneurons and permits simulation of their electrical activity.

2.1 Soma

In the most studies the size of the cell body of spinal motoneuron has been obtained from the mean value of two diameters at right angles in a nucleolar section. Such data from six studies are shown, after further analysis, in Table 3. Comparison of the mean soma diameters for different ages and from different sources shows that size did not significantly change after birth. Mean length values of the major and minor axes of elliptical somata are 31.51±8.28 μm and 19.56±5.52 μm, respectively (n=7; Thurbon *et al.*, 1998). Thus, we could calculate the major/minor axis ratio as equal to 1.69±0.57, which is close to 1.44±0.34 obtained by Kerai *et al.* (1995) and to 1.7±0.4 (Dekkers *et al.*, 1994). Numerical values from Thurbon *et al.* (1998) were actually used for motoneuron model construction.

Table 3. *Experimentally measured soma mean diameter (± s.d.) of rat neonatal motoneurons*

1–3 days	*4–6 days*	*7–15 days*	*references*
16.9±1.9 µm	19.6±2.0 µm	23.3±2.5 µm	Fulton and Walton, 1986
21.7±3.0 µm (n=89)	–	–	Takahashi, 1990
17.9±0.6 µm (n=60)	16.6±0.3 µm (n=20)	19.2±3.5 µm (n=16)	Dekkers *et al.*, 1994 [a]
22.7±3.64 µm (n=250)	–	26.0±4.22 µm (n=285)	Kerai *et al.*, 1995 [b, c]
25.3±0.48 µm (n=23)	24.1±5.37 µm (n=45)	24.7±2.32 µm (n=15)	Safronov and Vogel, 1995 [c]
–	–	25.53±6.1 µm (n=7)	Thurbon *et al.*, 1998 [d]

[a] motoneurons innervating *tibialis anterior* and extensor *digitorum longus* muscles
[b] motoneurons innervating *soleus hallucis longus* muscles
[c] in the present study standard error values were transformed to standard deviations using the following equation: $s.d. = s.e. \cdot \sqrt{n}$ where n=number of observations.
[d] in the present study the mean diameter were obtained from length of the major and the minor diameters of soma.

2.2 Axon

Owing to the absence of reliable morphological data for axons of newborn rat spinal motoneurons, Lüscher and Larkum (1998) suggested axon morphology based on the dimension of the axon of neocortical pyramidal cells and scaled diameters to those of neurites measured in cultured motoneurons. The axon hillock (AH) was then 8 µm long and tapered from 3 µm to 0.8 µm that is the diameter of the initial segment (IS). The length of the initial segment was assumed to be 10 µm. The axon proper was represented as a cylinder of 0.8 µm diameter and 500 µm length. These quantitative data were used in my study. To further assess the suitability of such data recalculated from cortical cells, I performed additional calculations starting from data provided from feline spinal motoneurons. In fact, Cullheim and Kellerth (1978) and Kellerth *et al.* (1979) performed the

morphological studies of axons, axons collaterals and serial sections of adult feline α-motoneurons. I scaled the cat α-motoneurons dimensions of AH and IS to the neurites measured for rat spinal motoneurons (Dekkers *et al.*, 1994; Thurbon *et al.*, 1998) to obtain 3 μm diameter and 7.9 μm length for AH, and 1.15 μm diameter and 8.5 μm length for IS.

Hence, two different, albeit indirect ways to express axon morphology quantitatively gave results in close accordance so as to enable the reconstruction of motoneuron axon as shown in Figure 26a, where the reconstructed soma and attached AH, IS and a truncated part of the axon proper are portrayed.

2.3 Proximal dendrites

Three numerical parameters were used to model proximal dendrites: mean base diameter, mean number of proximal dendrites and maximal length of proximal dendrites Data from Dekkers *et al.* (1994) and Thurbon *et al.* (1998) were pooled together to obtain the values of the mean base diameter and the number of proximal dendrites (3.16±1.42 μm and 6.92±1.89, respectively; mean±s.d.; n=13). Note that Dekkers *et al.* (1994) have emphasized the fact that neither the number of stem dendrites nor their mean diameter changed significantly within the period studied (P1-9). I therefore took as 6.92±1.89 the number of proximal dendrites to be entered in the stochastic calculation of motoneuron morphology.

The issue of dendritic diameter offered the additional opportunity to explore the reliability of the literature data and their application to the present model. A positive correlation between the mean soma diameter and the combined diameter of the primary dendrites has been shown by Dekkers *et al.* (1994), confirming the observations made on immature cats (for review see Lüscher and Clamann, 1992) and adult rats (Chen and Wolpaw, 1994). We have re-analyzed morphological data available from Thurbon *et al.*, (1998) to validate their correlation for their reconstructed motoneurons. The results of this analysis (Figure 27a) confirmed a positive correlation between the mean diameter of the soma and combined diameter of the primary dendrites (r=0.86, n=7; $p<0.05$; Spearman's rank correlation test). However, the data pertaining to Fig. 27a relied on a relatively small number of observations. It seemed therefore useful to perform further checks about the correlation between the lumped dendritic diameter and the cell soma. Calculations

indicated in Figure 27b show that a plot of sum of the dendritic base area ("sums of dendritic holes"; each base assumed as a round hole) in a double logarithm scale against the log mean soma diameter had a slope close to 3. This value demonstrate that the combined base area of the proximal dendrites had the correct proportionality with the respect to the somatic volume which is of course expressed as the soma diameter^3 (r=0.82, n=7; $p<0.05$). These calculations, therefore, fully validated the use of data from Thurbon *et al.* (1998) to be entered into my motoneuron model. Note, however, that these numerical values are means ± s.d. Once entered into the motoneuron stochastic model, it was necessary to confirm that the computer simulation did not rely mainly on some outlaying values within the s.d. range. Thus, we obtained the same correlation for our model as those found in Fig. 27a, b (data not shown), indicating that there was no systematic bias in the model operation.

Once proximal dendrite values were obtained, the next question was to decide about their space orientation. Motoneurons with a dendritic tree which expands spherically in 3D exist only in the lumbar and sacral segments of the spinal cord of adult cat (for review Lüscher and Clamann, 1992). Conversely, analysis of motoneuron morphology using reduced spinal cord preparations is restricted by the distortion of the dendritic trees orthogonal to the cutting plane and by the deep location of the cells. Notwithstanding these limitations, most studies emphasize that dendritic trees extend almost radially from the cell body (Dekkers *et al.*, 1994; Westerga and Gramsbergen, 1992). For sake of simplicity, in our study proximal dendrites were allowed to assume, with equal probability, all radial directions. Figure 26b illustrates the reconstructed soma with attached axon (marked by arrow) and proximal dendrites.

Figure 26. *Three main steps in the simulation of the neonatal rat spinal cord morphology*

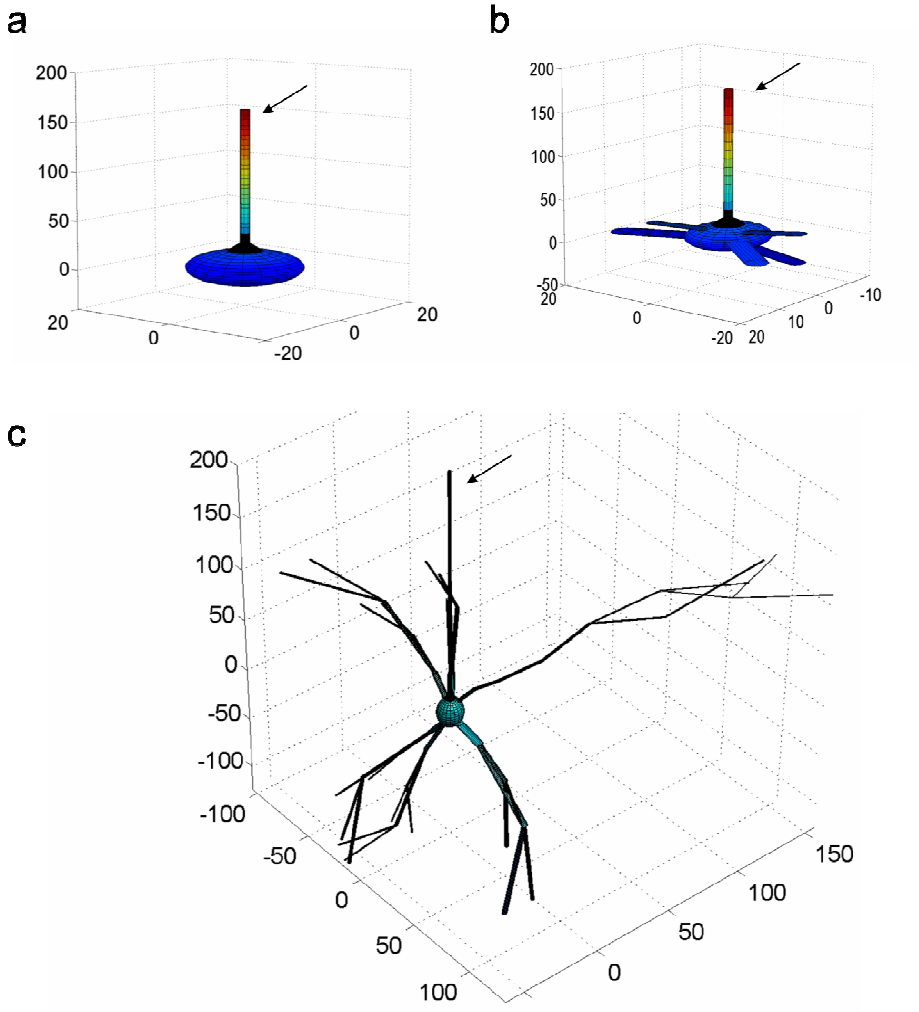

a, soma of the spinal motoneuron was represented as a prolate spheroid. The axon was simulated as a series of cylindrical compartments (0.1, 0.1 and 10 μm length for the axon hillock, the initial segment and the axon itself, respectively) attached to the soma surface. b, proximal dendrites were modeled as a cylindrical compartments and were allowed to grow, with equal probability, in all radial directions. c, final 3D model of the spinal motoneuron obtained by morphology simulation. Arrows show axon in all panels. All scales are in μm.

Figure 27. *Analysis of the experimentally obtained morphological description of the neonatal rat motoneurons*

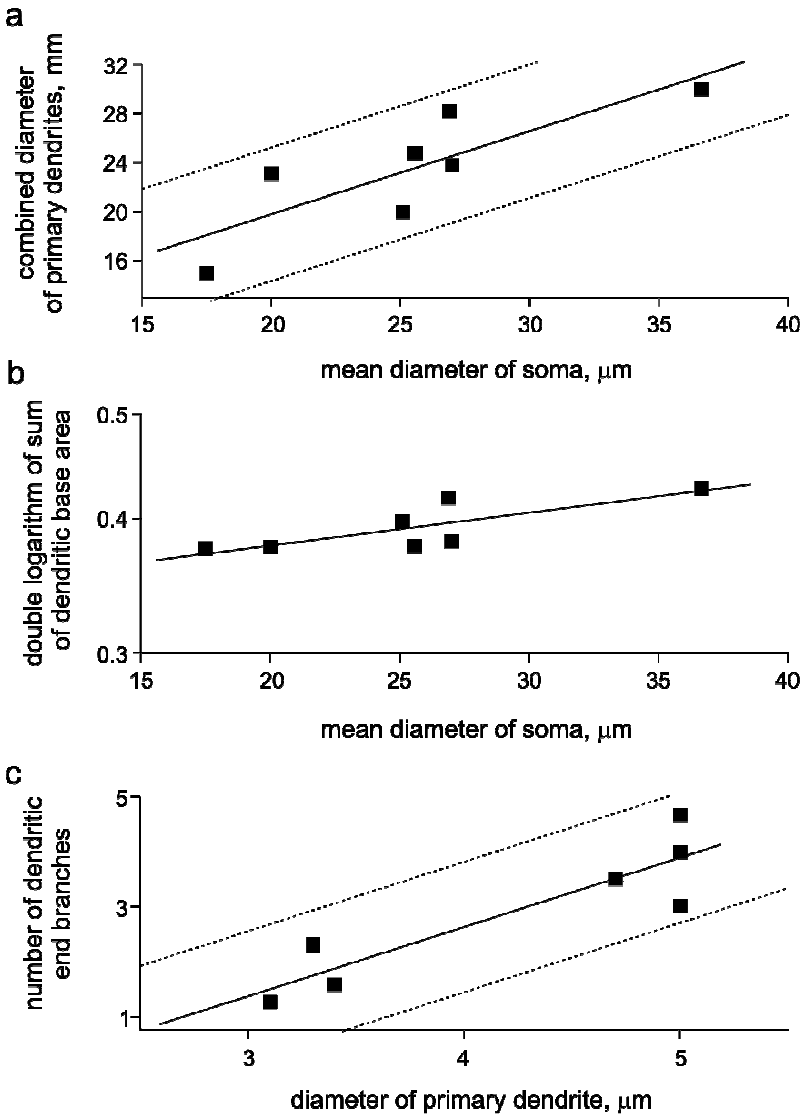

Plot of the sum of the diameters of all primary dendrites arising from each motoneuron against the mean soma diameter, for the 7 motoneurons (a). Solid line represents the linear regression of combined dendritic diameter on soma diameter: the slope is 0.68. Dash lines represent borders limiting the choice of the soma-stem dendrites relation. The plot of the sum of dendritic base area in the double logarithmic scale against the soma diameter is shown in (b), the same motoneurons as in (a). Slope of the regression (solid) line is 2.82. Relationship between diameter of primary dendrite and number of end terminals of dendritic tree arising from this primary dendrite is shown in (c). Dash lines represent boundaries for possible primary dendrite diameter – number of dendritic terminals relation. The result of Spearman's rank correlation test for a, b, c is given in the text (Data from Thurbon *et al*., 1998).

2.4 Distal dendrites

Dendritic trees for each proximal dendrite were constructed individually. At first, the number of sibling dendrites for each parent dendrite was chosen to be two, so each branching point was a bifurcation. This is justified by the fact that, at least for cat motoneurons, trifurcations are ≤ 5 % of all branching points (Brown and Fyffe, 1981; Kernell & Zwaagstra, 1988).

The classical way to represent quantitatively the ratio between the parent dendritic diameter and the sum of the sibling dendritic diameters is the Rall's ratio $\left[(d_{parent,1}^{3/2} + d_{parent,2}^{3/2}) / d_{parent}^{3/2}\right]$ where d is the dendritic diameter and *parent,n* denotes the sibling dendrite of a given parent dendrite. Thurbon *et al.* (1998) have found the mean Rall's ratio for pooled interneurons and motoneurons to be equal to 0.92±0.14 and for motoneurons alone to be 0.89±0.13. Dekkers *et al.* (1994) have calculated mean diameters for proximal and distal dendrites, which are 1.7±0.6 and 0.7±0.1 μm, respectively, unfortunately these numbers can not be used to estimate Rall's ratio, because the exact combinations between diameters of distal dendrites and parent dendrite is unknown. The ratio $d_{sibling} / d_{parent}$ was calculated to be 0.4 from data by Dekkers *et al.* (1994) and, for simulation purposes, expressed, for each sibling dendrite, as $d_{parent} \cdot [0.4 \pm rand(0.6)]$ μm (mean±s.d.). The Rall's ratio from Thurbon *et al.* (1994) was the limiting value of diameter ratio for each branching point.

Further reconstruction of the dendritic tree required two additional characteristics: branching maximal order and number of dendritic terminals. The first one can be obtained from existing data, while the second one relates to the diameter of the 1st-order dendrite. Pooled data from Dekkers *et al.* (1994) and Thurbon *et al.* (1998) give a value for branching maximal order equal to 5.1±1.3 (n=13). Again, these data were subjected to validation prior to the application to our model. Thus, a number of studies have reported a close relation between area (diameter) of proximal dendrite and complexity of the dendritic tree arising from it (for review see Lüscher & Clamann, 1992). We have re-analyzed data published by Thurbon *et al.* (1998) to check the relation between number of dendritic terminals and diameter of the proximal dendrite. Because Figure 27c confirms this relation (r=0.85, n=7; P<0.05), the ratio can be used

Table 4. *Comparison of experimental and simulated morphological characteristics*

parameter	*pooled experimental data*	*model (n=25)*
A_D, μm^2	6825±1918 *	8713±1990
A_S, μm^2	1788±893	1557±483
A_D/A_S	4.3±2.3	6±2
bmo	5.1±1.3 *	5±1
n-Prox	6.3±1.8	6.1±1.3
n-End	15.1±3.9	27.8±9
l-Tot, μm	2634±676 *	2447±842

* n=13, for not marked n=7.
Mean values ±s.*d.* A_D, dendritic membrane surface area; A_S, somatic membrane surface area; bmo, branching maximal order; n-Prox, number of stem dendrites; n-End, number of dendritic terminals; l-Tot, total dendritic path length.

to limit the choice of constructed dendritic tree (dash lines represent boundaries for possible proximal diameter–number of dendritic terminals combinations). Figures 28a shows an example of how I could reconstruct a dendritic arborization using the data mentioned above. On the basis of this approach I could then build a 3D model of a motoneuron as indicated in Fig. 26c. The numerical values used for this simulation and provided by the model are listed in Table 4. Figure 28c shows example of the dendrogram of the motoneuron obtained using previously described technique.

Figure 28*. Three dimensional reconstruction of dendritic arborization. Relative complexity and dendrogram of simulated motoneurons morphology*

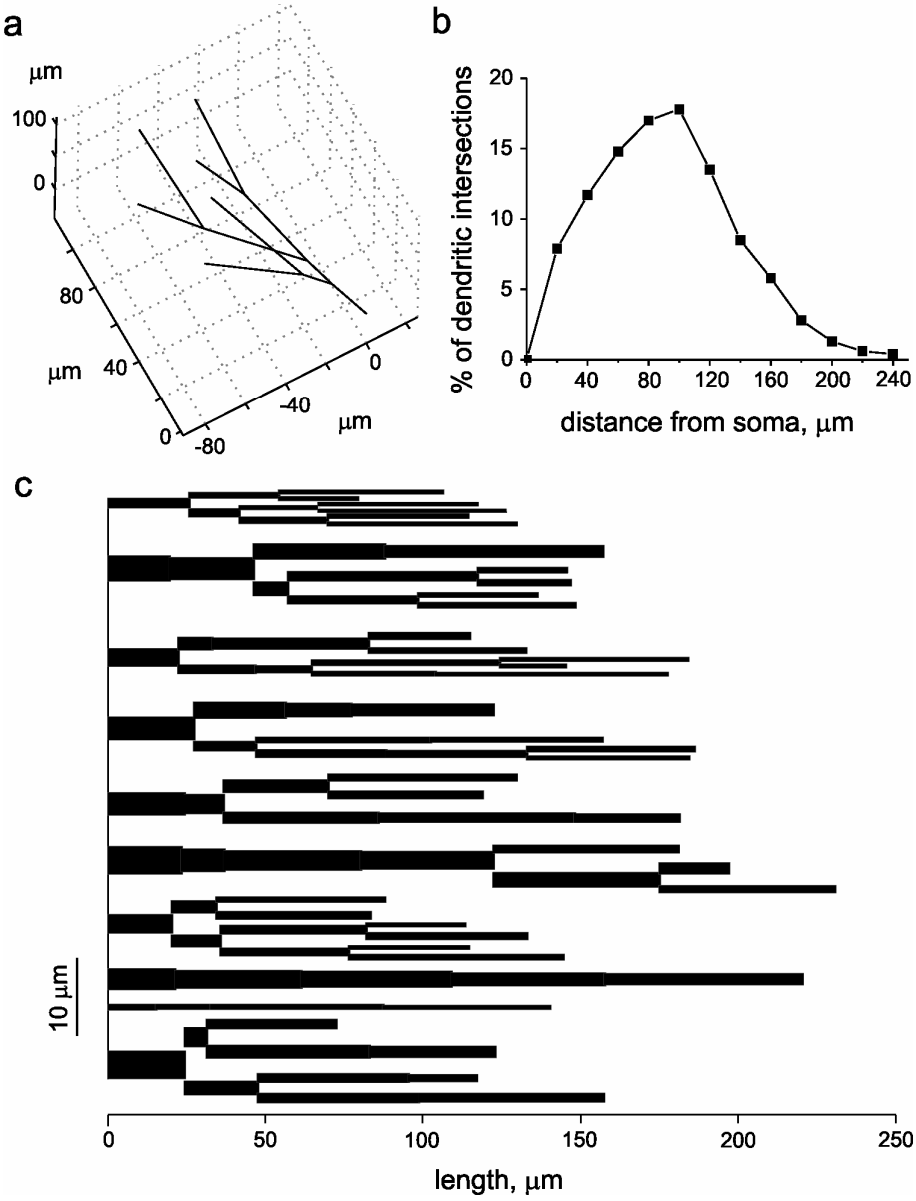

a, three dimensional representation of the dendritic branch arborization. Relative complexity graph expresses the number of dendrites piercing a sphere at a certain distance from the soma as a percent of total number of dendrites (b). Dendrogram of the single motoneuron obtained by the simulation is shown in c.

2.5 Motoneuron complexity defines synaptic input topography

To understand the issue of neuronal integration of multiple signals, Lüscher and Clamann (1992) have explored one property of motoneurons, namely their "complexity" taken to indicate the distribution and extension of dendritic branches.

In their representation the motoneuron is at the center of sphere, the diameter of which varies with defined steps. With this spatial approximation it becomes then possible to calculate how many dendrites pierce the sphere's surface at a certain distance from the soma. "Relative complexity" then expresses the number of dendrites piercing the sphere at a certain distance from the soma as a percent of total number of dendrites. This type of "complexity" can thus express the motoneuron topography available to distribution of afferent inputs (Luscher & Clamann 1992).

Dekkers *et al.* (1994) used a Sholl diagram to characterize the extent of dendritic outgrowth as a function of distance from the soma. This type of analysis represents an approach to defining relative complexity of spinal motoneurons, although performed in a 2D space. At both P2 and P9, the greatest number of dendritic intersections occur at ~80 μm from the soma, and the maximal dendritic length is in the range of 220-240 μm. Dekkers's *et al.* measurements were therefore used to constrain our 3D representation of the motoneuron. One drawback was the lack of experimental data on the actual length of proximal and distal dendrites. The maximal length for the proximal dendrites was assumed to be 25 μm. All distal dendrites were divided into the three groups. The first group contains the most distal dendrites, and half of the total number of distal dendrites was included in this group; the maximal length of these dendrites was assumed to be 40 μm. The second group contains distal dendrites lying most closely to the soma; this group includes 30% of the total number of distal dendrites and their maximum length was chosen to be 70 μm. The third group contains "middle lying" dendrites with maximal length 85 μm and represents 20% of all dendrites. Accurate tuning of three lengths allowed modelling the motoneuron with a given relative complexity. However, it should be noted that this division was made to closely simulate dendritic structures and did not reflect any experimentally obtained morphological peculiarities. Table 5 summarizes the experimental and calculated parameters to express the plot (see Fig. 28b) of calculated relative complexity (in 3D) for a sample of 25 model motoneurons. The peak relative complexity was between around 80-100 μm in accordance with Dekkers's *et al.* data.

Table 5. *Distribution of the voltage-gated conductances through the motoneuron surface*

	INa, S/cm^2	IK_A, S/cm^2	IK_{dr}, S/cm^2
Soma	0.113	0.218	0.029
Proximal	0.003	0	0.001
Distal	0.003	0	0.001
AH	0.7	0	0.11
IS	0.7	0	0.11
Proper	0.012	0	0.04

Densities of somatic conductances were taken from Safronov *et al.* (2000). Distribution of IK_{dr} is the same as in Dai *et al.* (2002). Proximal and distal dendrites contain INa following Lüscher & Larkum (1998). The same reference was used to define INa in axon hillock (AH), IS (initial segment) and axon proper.

2.6 Examples of electrical activity generation

While simulation of the complex electrical behavior of the spinal motoneurons requires simulation of the different ionic currents (Booth *et al.*, 1997; Dai *et al.*, 2002;), action potential can be generated on the base of three voltage-dependent conductances, namely, Na^+, transient K^+ (K_A) and delayed-rectifier K^+ (K_{dr}) distributed through the surface (Lüscher & Larkum, 1998; Safronov *et al.*, 2000). After exporting motoneuronal morphology shown on Figure 29a and conductances distribution for these three currents (Table 6) into NEURON I simulated action potential generation by application of the current steps in the motoneuron soma and most distal axonal segment. Passive properties of the motoneurons membrane were defined following Thurbon *et al.* (1998) and were equal for all compartments. Thus specific membrane capacitance (C_m) was 2.4 μF/cm², membrane resistance was (R_m) 5.3 kΩ cm² and axial resistance (R_a) was 87 Ω cm. The resting membrane potential was mostly determined by reversal potential of uniformly distributed leakage current (-70 mV). Figure 29b shows voltage responses to the current pulses injected into the soma (open arrow), while graph represents current/voltage plot. Calculated input resistance for this example is 78 MΩ what is close to one obtained experimentally (Thurbon *et al.*, 1998). Note, however, that this value was measured

using two electrodes voltage patch-clamp and that is why it is different from the results of the present study. By application of the graded current steps (0.1 ms duration) to the most distal axonal segment (close arrow Figure 29a) it was possible to evoke initial segments or action potential in the soma of the motoneuron (Figure 29c). Stimulation of the soma by current step of 0.5 nA intensity and 5 ms duration also elicited action potential (Figure 29d). Thus modeled spinal motoneurons can be used to simulate electrical behavior.

2.7 Modeling of CFTR inhibitors action on motoneurons input resistance and spike overshoot

The present study suggested the expression of CFTR in neonatal rat spinal motoneurons. Application of CFTR antagonists increased input resistance and spike overshoot, two effects strongly correlated during glibenclamide application. Thus, the motoneuron model was used to simulate sharp electrode current clamp experiments testing changes in input resistance and overshoot. Motoneuron morphology was shown in Figure 29a, while somatic R_m was drastically decreased (166 Ω cm^2) to simulate sharp electrode penetration with resultant fall of input resistance to 22 MΩ as often observed, as a routine, antidromic action potential could still be successfully generated.

First, I simulated a thirty percent somatic R_m enhancement (216 Ω cm^2) in a conductance with a 23% increase in the input resistance (to 27 MΩ) produced by CFTR inhibitors (the experimentally observed increase was 29±10%; Figure 30a). In this case spike overshoot augmentation was observed together with its accelerated rise (Figure 30b). The hyperpolarizing action of a CFTR inhibitor was simulated by shifting the reversal potential of the somatic leakage current to -74 mV, a procedure which *per se* did not change the peak of the action potential (Figure 30c). The combined consequence of the last modification together with increased R_m led to resting potential hyperpolarization (to -74 mV), overshoot increase and longer time to peak (Figure 30d). Figure 30e shows that a simulated injection of 0.15 nA current into the soma of the hyperpolarized motoneuron restored the resting potential to -70 mV and spike rise time. However, a 2 mV overshoot increase was preserved. Similar effects to those obtained by changing of the somatic

properties could be observed with rather larger enhancements of the dendritic and axonal R_m. In particular, this increase had to be more than twice of control values to produce a 25% input resistance augmentation (not shown). Furthermore, faster spike rise time due to R_m increase could not be reversed by current injection into the soma (Figure 30f). Thus, the present model could validate the tight correlation between overshoot augmentation and input resistance rise, when a somatically-placed conductance (similar to CFTR) was suppressed.

***Figure 29**. Passive and active properties of modeled spinal motoneurons*

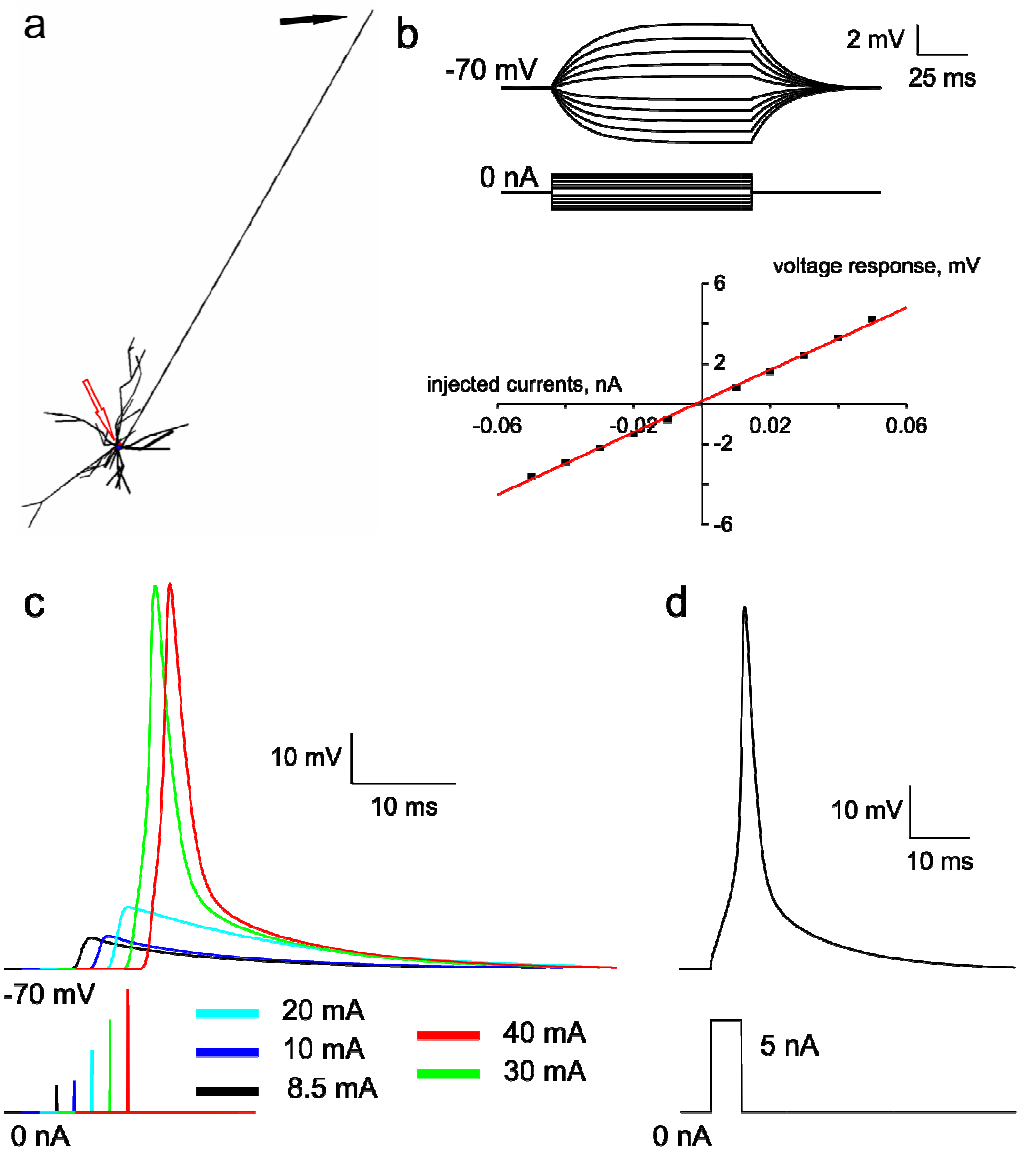

After simulation morphology of motoneuron was exported into NEURON (a; different example from Figure 26 and Figure 28). b, voltage responses to the soma injected (open arrow) currents (0.01 nA step; from -0.05 to 0.05 nA), graph represents I/V curve for exemplified motoneuron. High intensity stimulation (0.1 ms duration) of most distal axonal segment (closed arrow) evoked initial segment of the action potential or full spike (c), while application of the 0.5 nA (5 ms duration) depolarizing current step into the soma was enough to elicit action potential generation.

Figure 30. *Motoneuron model predicts that action potential overshoot amplitude depends on somatic membrane resistance*

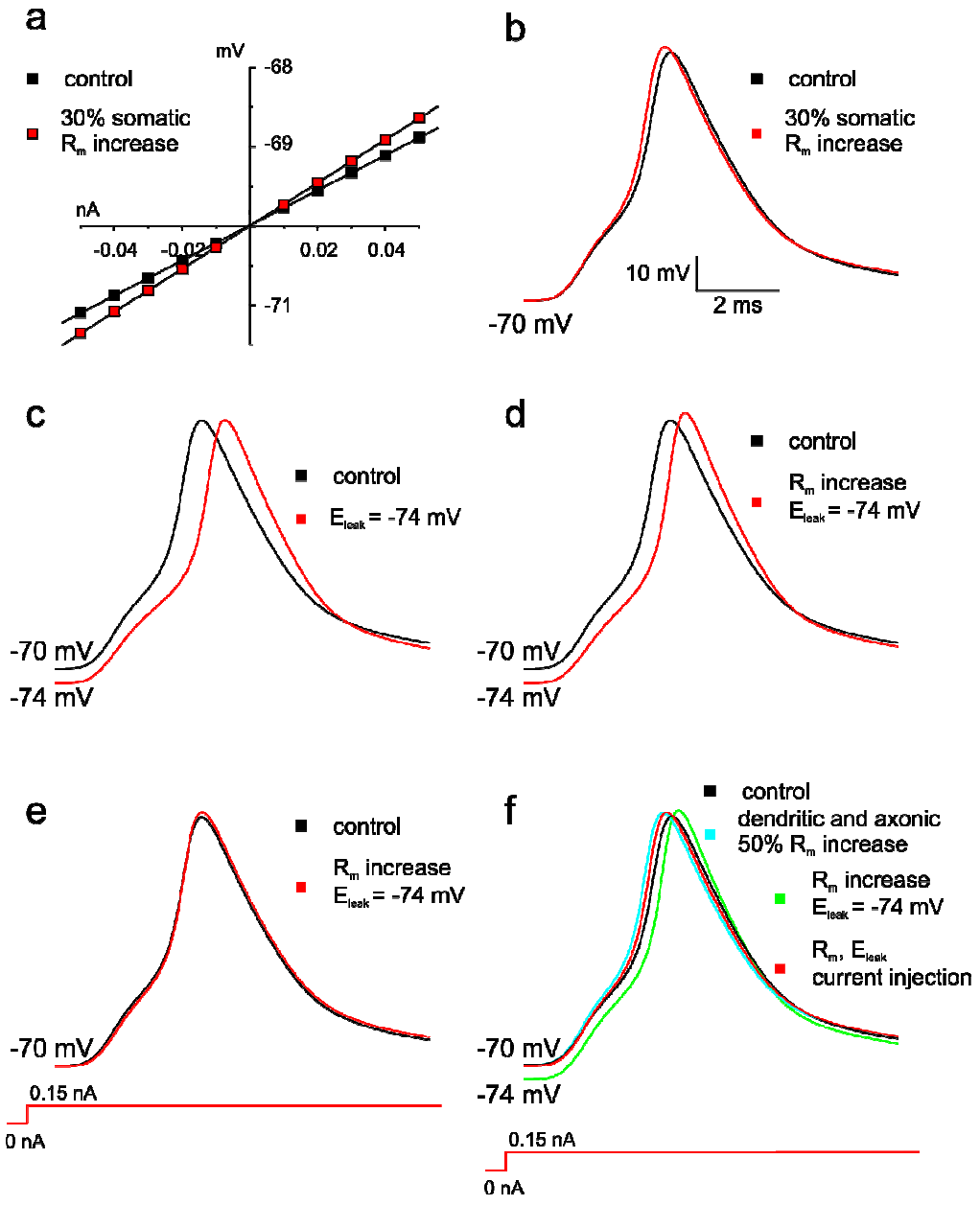

Sharp electrode penetration was modeled by drastic decrease of the somatic R_m followed by input resistance reduction measured as the slope of I/V curve (a, black squares; compare with Figure 29b). Thirty percent increase of the somatic R_m induced input resistance augmentation (from 22 to 27 MΩ; a, red squares) with faster antidromic spikes rise time and overshoot enhancement (b, black is spike in control; red after R_m increase). c, negative shift of the leakage current reversal potential (E_{leak}, from -70 mV to -74 mV) reduced spike peak without changing its amplitude. d, simulated changes in both R_m and E_{leak} led to larger overshoot and peak delay. e, rise time and resting membrane potential could be restored by positive current injection into the soma (current protocol is shown on the bottom), while overshoot rise was preserved. Panel f shows that changes of the dendritic and axonic membrane parameters did not fully reproduce

the experimentally obtained correlation between spike parameters and input resistance rise. Time and voltage scales in b are applicable for all panels.

Discussion

The principal finding of the present report is the demonstration of CFTR expression and function in the neonatal rat spinal cord. Pharmacological block of CFTR led to profound changes in network excitability chiefly due to alterations in the E_{Cl^-}, and thus in the ability of GABA (and glycine) to operate as inhibitory neurotransmitter. The second part of the present study presents one realistic 3D model of spinal motoneurons as the outcome of stochastic processes. This model can be used in the future studies to simulate complex interplay between synaptic inputs, and passive (and active) properties of spinal motoneurons, thus providing an understanding of the complex integration mechanisms. Furthermore, the model might help to analyze the functional consecuences of the motoneuronal excitability of GABA (and glycine) induced depolarization and hyperpolarization.

Action of glibenclamide on the spontaneous activity in the neonatal rat spinal cord can not be explained by K^+ conductance block

At the first stages of the present study, I examined the possibility metabolic regulation of the spinal network activity via ATP-sensitive potassium (K_{ATP}) channels which couple cell metabolism to electrical activity of the plasma membrane by regulating membrane K^+ fluxes (Ashcroft, 1988, 2005; Nichols, 2006). A reduction in metabolism opens K_{ATP} channels, producing K^+ efflux, membrane hyperpolarization, and suppression of electrical activity (Tarasov *et al.*, 2004). Thus K_{ATP} channels provide link between metabolic state of the cell and its excitability. The metabolic state of the neurons is dependent on their electrical activity, so long-lasting burst discharges inducing significant changes in transmembrane ion concentrations require high metabolic efforts for ion concentrations restoration (Yamada *et al.*, 2001; Yamada & Inagaki, 2002).

On cerebellar granule (D'Angelo *et al.*, 2001) or thalamic (Fuentealba *et al.*, 2004) neurones, electrical oscillations have been demonstrated to be paced by cyclic activation of a slow K^+ conductance. While the precise identification of such a K^+ conductance remains to be established, other studies have shown that, on brainstem

respiratory neurons, rhythmic changes in K_{ATP} channel activity take place during oscillations presumably because of cyclic variations in the intracellular ATP concentration in the immediate vicinity of the K_{ATP} channels (Haller *et al.*, 2001). In the motoneurons of the hypoglossal nucleus, electrical oscillations evoked by activation of metabotropic glutamate receptors have been shown to be apparently depended on the operation of K_{ATP} channels (Sharifullina *et al.*, 2005).

Questioning the possible role of the K_{ATP} channels in the regulation of the spontaneous activity of the neonatal rat spinal cord, I applied potent blockers of the K_{ATP} channels such as glibenclamide and tolbutamide (Bryan *et al.*, 2004). In these experimental conditions, the spinal cord excitability was strongly increased. Glibenclamide transformed spontaneous, irregular heterogeneous discharges evoked by application of the $GABA_A$ receptor antagonist bicuculline into more homogeneous bursts characterized by increased regularity of their inter event intervals. This effect might be explained by glibenclamide-dependent block of the tonically active K_{ATP} channels leading to neuronal depolarization which enhanced spinal network excitability. This effect is similar to the changes in bursting by further application of strychnine, an antagonist of glycinergic receptors, which converted asynchronous events into synchronous, regular, slow bursts with intraburst oscillations (Bracci *et al.*, 1996a, b).

The dependence of disinhibited activity on the metabolic state of spinal networks has been shown by application of Na^+/K^+ pump antagonists (Ballerini *et al.*, 1997). My next purpose was to investigate role of K_{ATP} conductances in the disinhibited bursts generation because these longlasting, repeated events are expected to place metabolic strain on cell energy resources to re-establish the correct ionic gradient. Usually depolarization by high extracellular K^+ concentration or increase in spinal network excitability is followed by speeding up of disinhibited bursts with shortened duration. Such an effect is typically observed when applying the K^+ channel blocker 4-aminopyridine (4-AP) during disinhibited bursting evoked by strychnine and bicuculline (Taccola & Nistri, 2005). The same effect is obtained by bath application of excitatory substances such as 5-HT (Bracci *et al.*, 1996a), NMDA, carbachol (Bracci *et al.*, 1996b) and apamin (Ballerini *et al.*, 1997). Conversely, application of glibenclamide or tolbutamide in the presence of bicuculline and strychnine surprisingly perturbed the highly periodic rhythmicity with subsequent increase in burst amplitude and probability of doublets. These phenomena could be reversed by further increasingly network excitability with

high extracellular K^+ or NMDA. All these findings suggested for the first time that sulphonylureas had another action target rather than the K_{ATP} conductances. To check this possibility, the action of glibenclamide on mono- or polysynaptic potentials was investigated.

Changes in electrically or pharmacologically induced network activity evoked by glibenclamide

Although increased network excitability and larger EPSPs in the presence of glibenclamide might have been compatible with pharmacological block of K_{ATP} channels, motoneuron hyperpolarization together with resistance increase was clearly inconsistent with this interpretation and was probably the cause of the larger spike amplitude (without further changes in spike width or decay). Furthermore, the fall in recurrent IPSP amplitude argued against a broad increase in synaptic transmission merely caused by larger neuronal input resistance. It was also difficult to understand why K^+ channel inhibition should have induced differential modulation of effects due to activation of glutamate, GABA or glycine receptors at network level.

It seemed useful to consider whether a unifying hypothesis could account for the complex effects of glibenclamide independently from a K^+ conductance block. Hence, it is suggested that the increase in the mono (and poly) synaptic reflexes as well as the AMPA or NMDA-mediated responses together with the decreased effects of GABA or glycine (and IPSPs), could all be explained by assuming a reduction in a neuronal conductance operating at resting potential and also controlling the action of GABA and glycine. A Cl^- conductance appeared to be a candidate suitable for this role and pointed us to consider CFTR because the action of glibenclamide was produced by a concentration typically blocking this transporter rather than K_{ATP} channels (Schultz *et al.*, 1999).

CFTR as a Cl^- regulator

The cystic fibrosis transmembrane conductance regulator (CFTR), an integral membrane protein controlling Cl^- secretion, is expressed in epithelial cells of intestine, airways, secretory glands, bile ducts, and epididymis (Sheppard & Welsh,

1999; Nilius & Droogmans, 2003) for regulating fluid flow and ion concentrations (Sheppard & Welsh, 1999; Nilius & Droogmans, 2003). Genetic mutations of CFTR underlie cystic fibrosis disease characterized by disrupted epithelial Cl^- transport (Lewis *et al.*, 2003). A potent inhibitor of CFTR function is glibenclamide (Schultz *et al.*, 1999).

Nevertheless, because CFTR is thought to be virtually absent from the central nervous system (Hincke *et al.*, 1995), glibenclamide has been widely used to study the role of K_{ATP} channels in the brain (Mironov *et al.*, 1998; Yamada & Inagaki, 2002). The present report is, therefore, the first suggestion based on electrophysiological and molecular biology data that CFTR was present in the spinal cord of the newborn rat for the purpose of controlling resting membrane potential and Cl^- dependent inhibition mediated by GABA and glycine.

How could CFTR contribute to E_{Cl^-} in newborn spinal neurons?

In the adult brain Cl^- is continuously extruded by the membrane transporter KCC2 to generate a rather negative equilibrium potential for this anion (Ben Ari, 2002; Payne *et al.*, 2003). In the neonatal brain, transporter immaturity is responsible for impaired Cl^- dependent inhibition mediated by GABA and, thus, for lower convulsion threshold (Ben Ari, 2002; Rivera *et al.*, 2005). Conversely, in the newborn spinal cord, KCC2 expression (though not as high as in the adult) is large enough to make unclear the origin of intracellular Cl^- accumulation underlying the GABA or glycine evoked depolarization (Hubner *et al.*, 2001; Ueno *et al.*, 2002; Stein *et al.*, 2004). Because only Cl^- is responsible for the action of GABA or glycine on spinal motoneurons (Hamill *et al.*, 1983; Wu *et al.*, 1992; Cupello, 2003), and the E_{Cl^-} value for passively distributed Cl^- would be very negative (-87 mV), other mechanisms for the depolarized E_{Cl^-} should be sought.

On motoneurons recorded with sharp electrodes, glibenclamide significantly attenuated inhibitory synaptic currents generated by Renshaw cells. The limited current passing ability of sharp electrodes did not allow us to observe the value of E_{Cl^-} directly which was therefore obtained by extrapolation, on the assumption that the inhibitory synaptic current displayed minimal rectification (Gao & Ziskind-Conhaim, 1995). Even if the precise value of E_{Cl^-} could not be obtained, the negative shift in the current/voltage plot plus the increased membrane resistance suggested

glibenclamide-mediated modulation of a Cl^- conductance contributing to the leak conductance of motoneurons. In view of the known blocking action of glibenclamide on CFTR, we suggest this membrane protein to be responsible for the observed changes. Our proposal is supported by the demonstration that analogous results were observed on motoneurons with tolbutamide or DPC, both considered to be CFTR inhibitors (Schultz *et al.*, 1999), and, on interneurons, with $CFTR_{inh}$-172 (Thiagarajah *et al.*, 2004). On interneurons, the use of the whole cell patch clamp technique precluded the normal operation of CFTR as previously reported and made it necessary to use 8-bromo-cAMP as a stable activator of CFTR (Sheppard & Welsh, 1992; Bachmann *et al.*, 2000; Sheppard *et al.*, 2004; Wright *et al.*, 2004). The resulting inward current and resistance decrease were readily antagonized by $CFTR_{inh}$-172, indicating that CFTR expression and function were not confined to spinal motoneurons.

The basic properties of CFTR differ from those of other Cl^- channels or transporters (Sheppard & Welsh, 1999). In fact, although CFTR can form Cl^- channels when expressed in heterologous cells, it has recently been suggested that, in physiological conditions, it mainly acts as a regulator of other membrane channels (Nilius & Droogmans, 2003), a process which is also expected to occur in the neonatal rat spinal cord.

The most obvious target for such an action by CFTR is the NKCC1 transporter that accumulates Cl^- in neonatal brain neurons to reach a value of E_{Cl^-} responsible for the depolarization induced by GABA or glycine (Dzhala *et al.*, 2005). Our hypothesis is that CFTR stimulated NKCCl to increase intracellular Cl^- as previously observed in cell culture (Adam *et al.*, 2005), in accordance with the notion that CFTR enhances the functional expression of NKCC1 (Shumaker & Soleimani, 1999). It should be emphasized that the present report is the first one to apply such a hypothesis to the neonatal spinal cord: future studies will be necessary to conclusively demonstrate this phenomenon in the newborn rat spinal cord, including its precise cellular location once more suitable antibodies become available. Furthermore, it will be necessary to examine the CFTR involvement in the developmental regulation of chloride transporters and whether it might contribute to shift depolarizing GABA (glycine) responses to hyperpolarizing ones.

Despite the preliminary nature of the present study, our electrophysiological results following application of glibenclamide enabled us to outline a functional role of CFTR in controlling E_{Cl^-} and excitability of neonatal spinal neurons.

CFTR transcripts and membrane expression in spinal tissue

The presence of CFTR in the brain is purportedly limited to hypothalamus (Mulberg *et al.*, 1995; Weyler *et al.*, 1999). Nevertheless, our demonstration of CFTR mRNA presence and protein expression by neonatal spinal cord tissue provides a compelling reason to consider that glibenclamide (and tolbutamide, DPC or $CFTR_{inh}$-172) induced their effects by inhibiting CFTR. Because the mature glycosylated form of CFTR (Cheng *et al.*, 1990) was strongly expressed in membrane extracts, this is suggested to be an important regulator of Cl^- transport in the neonatal spinal cord. Immunocytochemical demonstration of rat CFTR-positive neurons was fraught with technical problems due to Ab cross-reactivity and did not allowed us to identify the cell types immunoreactive for CFTR.

Could the effects of glibenclamide be attributed to K_{ATP} channel block?

The two prime candidates for formation of functional K_{ATP} channel in the brain are the Kir6.2 subunit of the K^+ channel family plus the SUR1 element of the glibenclamide-sensitive sulfonylurea receptor (Aguilar-Bryan & Bryan, 1999). Although Kir 6.2 subunits are moderately expressed in the adult rat spinal cord (Thomzig *et al.*, 2005), their expression in the developing spinal cord is unknown. Nevertheless, Kir6.2$^{-/-}$ mice show normal behavioral phenotype (Yamada *et al.*, 2001) indicating their minimal contribution to motor or sensory functions. This finding accords with the fact that most brain K_{ATP} channels operate only in ATP-depleted metabolic states such as hypoxia and are usually closed at resting conditions (Yamada & Inagaki, 2002). For these reasons, it was improbable that the glibenclamide action on neonatal neurons at rest or on synaptic transmission involved K_{ATP} channel inhibition because all the electrophysiological parameters (spike amplitude, input resistance) indicated adequate cell oxygenation and made thus unlikely K_{ATP} activation. The present data thus suggest that care is needed when interpreting effects following sulphonylurea drug application to central nervous system neurons as simply due to K_{ATP} channel block.

Functional implications

In the neonatal rat spinal cord, although GABA and glycine depolarize neurons because their E_{Cl^-} is positive to resting potential, these transmitters exert strong synaptic inhibition (Marchetti *et al.*, 2002). The present data suggest that the CFTR operation contributed to the depolarized E_{Cl^-} by promoting Cl^- intracellular transport. Membrane depolarization evoked by GABA (or glycine)-opened Cl^- channels may inhibit neurons through voltage-dependent inactivation of Na^+ (and Ca^{2+}) conductances necessary for firing action potentials in analogy to GABA-mediated presynaptic inhibition in the adult spinal cord (Rudomin, 2002). Blocking these phenomena with CFTR inhibitors would then hyperpolarize neurons and increase their excitability via voltage-dependent de-inactivation of Na^+ (and Ca^{2+}) channels plus enhanced input resistance.

Construction of neuronal model on the basis of available morphological parameters

There are two main mathematically-different approaches to reconstruction neuronal morphology, necessary for realistic modeling of neuronal activities. The first one attempts to capture biophysical aspects of neurite initiation, elongation and branching. These models usually concentrate either on the intracellular or the extracellular biophysical aspects of the neurite outgrowth as most of them do not consider the actual shape of the neurite in two- or three-dimensional space (reviewed by Kiddie *et al.*, 2005). The second approach combines different non-biophysical stochastic algorithms, which, on the basis of limited number of known parameters can simulate the shape of the dendritic tree realistically (Hillman, 1979; Burke *et al.*, 1992; Ascoli *et al.*, 1999; Ascoli, 2001). While modeling of soma and axon is usually not discussed, the greatest focus concentrated on the dendritic arborization. Hillman (1979) separated two groups of parameters sufficient to describe and model the shape of neurons once their characteristic correlation is known. The first group is needed to define the fundamental aspects of denditic shape, and these parameters (stem diameter, terminal-segment diameter, segment taper, segment length, branch power, ratio between cross-section areas of daughter branches and spatial orientation of segments) are considered as fundamental shape

parameters. The second group (global parameters) provides information about the size and orientation of the tree combining dendritic tree volume, surface area, total dendritic length, orientation and topological type. All of these parameters can be measured during histological reconstruction of neuronal structures. Nevertheless, this goal has never been fully achieved for the developing spinal rat motoneurons since to the best of my knowledge, previous studies considered just global parameters (Westerga & Gramsbergen, 1992; Dekkers *et al.*, 1994; Thurbon *et al.*, 1998). Burke's algorithm, which is also local, stochastic and recursive, but it uses parameters that do not have a direct biophysical meaning (Burke *et al.*, 1992). The recent study of spinal mouse motoneurons during development revealed lack of certain correlations between morphological parameters (Li *et al.*, 2005) present in adults (Lüscher & Clamann, 1992), so the use of recursive algorithms is limited also for reconstructing neurons at early stage of development. That is why Hillman's and Burke's algorithms could not be used to fully reconstruct the dendritic tree of developing motoneuron. Likewise, Ascoli's *L-NEURON* algorithms (Ascoli *et al.*, 2001) could not be used because they are based on these two algorithms. In the present study the reconstruction algorithm was based on the available, albeit limited, number of existing correlations that limited the choice of morphological parameters (number of proximal dendrites, number of branching points and diameters of proximal dendrites) rather than determine them. All other parameters were chosen on the basis of stochastic distributions with experimentally determined mean and standard deviation values. Only one parameter, namely the maximal length of distal dendrites, was selected regardless any experimental data, simply because it is not currently available. Bearing in mind this limitation, the arbitrary parameters concurred to supply a good simulation of the total dendritic path length and relative complexity of dendritic trees. Unfortunately, validation of the proposed model is restricted by the limited availability of experimental data, so that future studies are needed to confirm as realistic the reconstruction of rat spinal motoneurons during development.

Models of spinal motoneurons electrical activity

The compartmental models, which neglect dendritic apparatus or simplified it to separate from the soma compartment or consider it as cylindrical compartments of

different diameters, were used in a relatively large number of studies of rat spinal motoneurons (Lev-Tov *et* al., 1983; Rose & Dagum, 1988; Booth *et al.*, 1997; Safronov *et al.*, 2000; Dai *et al.*, 2002). Since the integrative properties of the neurons are mostly determined by the geometry of their dendritic tree, the distribution of voltage-gated conductances and the localization of synaptic inputs (review Segev & London, 2000), such simple models have limited usefulness. Models of rat spinal motoneurons (in organotipic spinal cord slices) which attempted to consider all these features together, have appeared only during the last decade following the development of computational facilities and improved reconstruction techniques (Ulrich *et al.*, 1994; Larkum *et at.*, 1998; Lüscher & Larkum, 1998). The present study provides a morphological basis for modeling developing motoneurons behavior and shows that this simulated morphology can also be used to model the electrical properties of motoneurons.

One important aspect of modeling of the electrical behavior is the distribution of voltage-dependent channels on the surface of the neuron. Safronov and Vogel (1995) observed that TTX-sensitive Na^+ channels together with transient (A-type) and delayed-rectified (DR-type) K^+ channels form the basis of voltage-activated conductance in the somatic membrane of neonatal rat motoneurones. This study has therefore confirmed the previous findings by Takahashi (1990) who found all of these membrane currents in spinal motoneurons (see also recent Taccola & Nistri, 2006). However, further modeling of the excitability of the spinal motoneurons somata revealed that the density of Na^+ channels observed experimentally is too small to generate action potentials, and that only a four- to eightfold increase in the original density of these channels can make the modeled somata adequately excitable (Safronov *et al.*, 2000). These results are not surprising because the spike initiation in the spinal motoneurons originates from axon hillock and axon initial segment (see references in Lüscher & Larkum, 1998).

Mainen and colleagues (1995) have modeled spike initiation in neocortical pyramidal neurons showing that, when dendritic and somatic Na^+ channels densities compatible with electrophysiological measurements are combined with much higher densities in the axon initial segment, spikes initiated at the initial segment regardless the site of stimulation. Modeling action potential propagation and back-propagation in dendrites of cultured rat motoneurons has been performed by Lüscher & Larkum (1998). Their study has shown that the high Na^+-channel density of g_{Na_max} = 700 mS/cm^2 at the axon hillock/initial segment region is

required to secure antidromic invasion of the somato-dendritic membrane, whereas for the orthodromically directed spike, Na^+-channel density of g_{Na_max} = 1,200 mS/cm^2 is required. Thus, I used the same values for Na^+ currents densities at the axon hillock/initial segments and dendrites, while somatic g_{Na_max} was set equal to the experimental data by Safronov *et al.* (2000). The simulation of antidromic propagation during the present study showed generation of both initial segment and full size all-or-non action potentials, thus validating the use of the model based on the simulated morphology.

Implication of electrical behavior modeling for explaining the effects of CFTR inhibitors

Input resistance increase and action potential overshoot augmentation by CFTR inhibitors were simulated by changing the passive properties of the modeled motoneurons. The augmentation of the action potential overshoot was considered as the epiphenomenon of input resistance rise and, in general, of the increased excitability of the motoneurons. The first step to obtain a relevant modeling situation was to add a somatic shunt like the one produced by the sharp electrode penetration: this was achieved with a drastic reduction in somatic membrane resistance (from 5.3 kΩ cm^2 to 166 Ω cm^2). Such a large change should not be surprising as it was introduced into the model of cat spinal motoneurons by Clements and Redman (1989) who compared sharp electrode experiments data with simulated behavior of histologically reconstructed cells. In this study the value of dendritic R_m was 10-30 times the somatic R_m value. The somatic shunt most probably reflects the experimental conditions (Durand, 1984) because modeling on the basis of data from whole-cell patch clamp recording does not require introduction of a somatic shunt (Ulrich *et al.*, 1994; Thurbon *et al.*, 1998; Larkum *et al.*, 1998; Lüscher & Larkum, 1998).

The application of CFTR antagonists produced input resistance increase. Simulation of this effect was performed by suppression of the somatic or dendritic/axonic leakage membrane conductances. Much higher increase in the dendritic/axonic resistance than in the somatic one was necessary to produce changes comparable with the experimentally observed ones. Furthermore, calculation of the current of CFTR Cl^- channels normalized to cell capacitance,

performed for this discussion, provides value 29 pA/pF closely approaching to one found in pancreatic duct cells (Gray *et al.*, 1994). This calculation is based on change in the somatic membrane conductance required to simulate the CFTR antagonists action (g_{CFTR}=1.4 mS/cm^2), a membrane capacitance value of C_m=2.4 μF/cm^2 (Thurbon *et al.*, 1998), Cl^- reversal potential found to be -20 mV (E_{Cl^-}) and simple equation $g_{CFTR}(V)\cdot(E_{Cl^-}-V_{rest})/C_m$, where V_{rest} is the resting membrane potential (-70 mV).

The other action of CFTR antagonists described in the present study was the slight (3 mV) hyperpolarization of the resting membrane potential. The standard Goldman-Hodgkin-Katz equation provides the value of resting membrane potential when the concentrations of three ions (K^+, Na^+, Cl^-) and their permeability (P_K, P_{Na}, P_{Cl}) are known. Forsythe and Redman (1988) calculated relative conductances equal to 0.13 and 0.25 for P_{Na}/P_K and P_{Cl}/P_K, respectively. Using reversal potentials -87 mV for K^+, +53 mV for Na^+ and -20 mV for Cl^- (Marchetti *et al.*, 2001b, Safronov *et al.*, 2000 and present study, respectively), the resting potential obtained from the Nernst and Goldman-Hodgkin-Katz equations is -41 mV. It is, therefore, 30 mV more positive than that measured experimentally, but this difference is not surprising because active transports are not included. Just the Na^+/K^+ pump contributes ~25 mV of negative shift (Ballerini *et al.*, 1997; present study). Further decrease of the P_{Cl}/P_K to 0.15 resulted in the calculated resting potential shift to -44 mV, thus producing 3 mV hyperpolarization. Thus it can be concluded that CFTR antagonists partly blocked a Cl^- leakage conductance.

While antidromic action potential invasion into the soma was secured by increased axon hillock and initial segment density of Na^+ channels (Mainen *et al.*, 1995; Lüscher & Larkum, 1998), spike shape was dependent on the actual location of leak conductance at somatic or dendritic/axonic level. A decrease in the somatic or dendritic/axonal leak conductance produced rise time acceleration and overshoot increase, most probably due to the increased electrical impedance. However, the appearance of cell hyperpolarization (obtained by shifting the leak current reversal potential) excluded an exclusively dendritic/axonal nature of the input resistance rise. Although resting potential hyperpolarization was reversed by somatic current injection, the accelerated rise time persisted, indicating distinct mechanisms and topology for these two effects.

In should be noted that while the systematic examination of CFTR expression sites on the membrane of motoneurons was not my aim, the model study predicted

somatic expression of CFTR. Mixed somato-dendritic expression of CFTR has been shown in immunocytochemical studies of neurons of the diencephalon, midbrain, pons and medulla oblongata (Mulberg *et al.*, 1994, 1995). Since, the highest expression of the inhibitory glycine and GABA receptors is found on motoneuron somata and more proximal dendrites (Bohlhalter *et al.*, 1996; Alvarez *et al.*, 1997), a somatic expression of CFTR would provide a close topographic link between Cl^- homeostasis and inhibitory transmission in spinal motoneurons.

References

Adam G, Ousingsawat J, Schreiber R, Kunzelmann K (2005). Increase in intracellular Cl^- concentration by cAMP- and Ca^{2+}-dependent stimulation of M1 collecting duct cells. *Pflugers Arch* **449**: 470-478.

Aguilar-Bryan L, Bryan J (1999). Molecular biology of adenosine triphosphate-sensitive potassium channels. *Endocr Rev* **20**: 101-135.

Alvarez FJ, Dewey DE, Harrington DA, Fyffe RE (1997). Cell-type specific organization of glycine receptor clusters in the mammalian spinal cord. *J Comp Neurol* **379**: 150-170.

Alvarez FJ, Dewey DE, McMillin P, Fyffe REW (1999). Distribution of cholinergic contacts on Renshaw cells in the rat spinal cord: a light microscopic study. *J Physiol* **515**: 787-797.

Ascoli GA (1999). Progress and perspectives in computational neuroanatomy. *Anat Rec* **257**: 195-207.

Ascoli GA, Krichmar JL, Nasuto SJ, Senft SL (2001). Generation, description and storage of dendritic morphology data. *Philos Trans R Soc Lond B Biol Sci* **356**: 1131-1145.

Ashcroft FM (1988). Adenosine 5'-triphosphate-sensitive potassium channels. *Annu Rev Neurosci* **11**: 97-118.

Ashcroft FM (2005). ATP-sensitive potassium channelopathies: focus on insulin secretion. *J Clin Invest* **115**: 2047-2058.

Bachmann A, Russ U, Waldegger S, Quast U (2000). Potent stimulation and inhibition of the CFTR Cl^- current by phloxine B. *Br J Pharmacol* **131**:433-440.

Ballerini L, Bracci E, Nistri A (1997) Pharmacological block of the electrogenic sodium pump disrupts rhythmic bursting induced by strychnine and bicuculline in the neonatal rat spinal cord. *J Neurophysiol* **77**: 17-23.

Beato M, Nistri A (1999). Interaction between disinhibited bursting and fictive locomotor patterns in the rat isolated spinal cord. *J Neurophysiol* **82**: 2029-2038.

Beggs S, Torsney C, Drew LJ, Fitzgerald M (2002). The postnatal reorganization of primary afferent input and dorsal horn cell receptive fields in the rat spinal cord is an activity-dependent process. *Eur J Neurosci* **16**: 1249-1258.

Ben-Ari Y (2002). Excitatory actions of GABA during development: the nature of the nurture. *Nat Rev Neurosci* 3: 728-739.

Birinyi A, Viszokay K, Weber I, Kiehn O, Antal M (2003). Synaptic targets of commissural interneurons in the lumbar spinal cord of neonatal rats. *J Comp Neurol* **461**: 429-440.

Bohlhalter S, Weinmann O, Mohler H, Fritschy JM (1996). Laminar compartmentalization of GABAA-receptor subtypes in the spinal cord: an immunohistochemical study. *J Neurosci* **16**:283-297.

Booth V, Rinzel J, Kiehn O (1997). Compartmental model of vertebrate motoneurons for Ca^{2+}-dependent spiking and plateau potentials under pharmacological treatment. *J Neurophysiol* **78**: 3371-3385.

Bracci E, Ballerini L, Nistri A (1996a). Spontaneous rhythmic bursts induced by pharmacological block of inhibition in lumbar motoneurons of the neonatal rat spinal cord. *J Neurophysiol* **75**: 640-647.

Bracci E, Ballerini L, Nistri A (1996b) Localization of rhythmogenic networks responsible for spontaneous bursts induced by strychnine and bicuculline in the rat isolated spinal cord. *J Neurosci* **16**: 7063-7076.

Bracci E, Beato M, Nistri A (1997). Afferent inputs modulate the activity of a rhythmic burst generator in the rat disinhibited spinal cord in vitro. *J Neurophysiol* **77**: 3157-3167.

Bracci E, Beato M, Nistri A (1998). Extracellular K^+ induces locomotor-like patterns in the rat spinal cord in vitro: comparison with NMDA or 5-HT induced activity. *J Neurophysiol* **79**: 2643-2652.

Brown AG, Fyffe RE (1981). Direct observations on the contacts made between Ia afferent fibres and alpha-motoneurones in the cat's lumbosacral spinal cord. *J Physiol* **313**: 121-140.

Bryan J, Vila-Carriles WH, Zhao G, Babenko AP, Aguilar-Bryan L (2004). Toward linking structure with function in ATP-sensitive K^+ channels. *Diabetes* **53**: S104-112.

Burke RE, Marks WB, Ulfhake B (1992). A parsimonious description of motoneuron dendritic morphology using computer simulation. *J Neurosci* **12**: 2403-2416.

Butt SJ, Kiehn O (2003). Functional identification of interneurons responsible for left-right coordination of hindlimbs in mammals. *Neuron* **16**: 953-963.

Butt SJ, Lebret JM, Kiehn O (2002) Organization of left-right coordination in the mammalian locomotor network. *Brain Res Rev* **40**:107–117.

Chen XY, Wolpaw JR (1994). Triceps surae motoneuron morphology in the rat: a quantitative light microscopic study. *J Comp Neurol* **343**: 143-157.

Cheng SH, Gregory RJ, Marshall J, Paul S, Souza DW, White GA, O'Riordan CR, Smith AE (1990). Defective intracellular transport and processing of CFTR is the molecular basis of most cystic fibrosis. *Cell* **63**: 827-834.

Clarac F (2005a). The history of reflexes. Part 1: from Descartes to Pavlov. *Neuroscience History on the Web.* http://www.ibro.info/Pub_Main_Display.asp?Main_ID=421.

Clarac F (2005b). The history of reflexes. Part 2: from Sherrington to 2004. *Neuroscience History on the Web.* http://www.ibro.info/Pub_Main_Display.asp?Main_ID=439.

Clarac F, Pearlstein E, Pflieger JF, Vinay L (2004). The in vitro neonatal rat spinal cord preparation: a new insight into mammalian locomotor mechanisms. *J Comp Physiol* **190**: 343-357.

Clements JD, Redman SJ (1989). Cable properties of cat spinal motoneurones measured by combining voltage clamp, current clamp and intracellular staining. *J Physiol* **409**: 63-87.

Crepel V, Rovira C, Ben-Ari Y (1993). The K^+ channel opener diazoxide enhances glutamatergic currents and reduces GABAergic currents in hippocampal neurons. *J Neurophysiol* **69**: 494-503.

Crockett DP, Harris SL, Egger MD (1987). Plantar motoneuron columns in the rat. *J Comp Neurol* **265**: 109-118.

Cullheim S, Kellerth JO (1978). A morphological study of the axons and recurrent axon collaterals of cat alpha-motoneurones supplying different hind-limb muscles. *J Physiol* **281**: 285-299.

Cupello A (2003). Neuronal transmembrane chloride electrochemical gradient: a key player in $GABA_A$ receptor activation physiological effect. *Amino Acids* **24**: 335-346.

Dai Y, Jones KE, Fedirchuk B, McCrea DA, Jordan LM (2002). A modelling study of locomotion-induced hyperpolarization of voltage threshold in cat lumbar motoneurones. *J Physiol* **544**:521-536.

D'Angelo E, Nieus T, Maffei A, Armano S, Rossi P, Taglietti V, Fontana A, Naldi G (2001). Theta-frequency bursting and resonance in cerebellar granule cells: experimental evidence and modeling of a slow K^+-dependent mechanism. *J Neurosci* **21**: 759-770.

Darbon P, Yvon C, Legrand JC, Streit J (2004). I_{NaP} underlies intrinsic spiking and rhythm generation in networks of cultured rat spinal cord neurons. *Eur J Neurosci* **20**: 976-988.

Dekkers J, Becker DL, Cook JE & Navarrete R (1994). Early postnatal changes in the somatodendritic morphology of ankle flexor motoneurons in the rat. *Eur J Neurosci* **6**, 87-97.

Dennis MJ, Ziskind-Conhaim L, Harris AJ (1981). Development of neuromuscular junctions in rat embryos. *Dev Biol* **81**: 266-279.

Dietz V (2002). Do human bipeds use quadrupedal coordination. *TRENDS in Neurosci* **25**: 462:467.

Dietz V (2003). Spinal cord pattern generators for locomotion. *Clin Neurophysiol* **114**: 1379-1389.

Dourado M, Sargent PB (2002). Properties of nicotinic receptors underlying renshaw cell excitation by alpha -motor neurons in neonatal rat spinal cord. *J Neurophysiol* **87**: 3117-3125.

Durand D (1984). The somatic shunt cable model for neurons. *Biophys J* **46**: 645-653.

Dzhala VI, Talos DM, Sdrulla DA, Brumback AC, Mathews GC, Benke TA, Delpire E, Jensen FE, Staley KJ (2005). NKCC1 transporter facilitates seizures in the developing brain. *Nat Med* **11**: 1205-1213.

Edgley SA (2000). Organisation of inputs to spinal interneurone populations. *J Physiol* **533**: 51-56.

Eide AL, Glover J, Kjaerulff O, Kiehn O (1999). Characterization of commissural interneurons in the lumbar region of the neonatal rat spinal cord. *J Comp Neurol* **403**: 332-345.

Fisher ND, Nistri A (1993). A study of the barium-sensitive and -insensitive components of the action of thyrotropin-releasing hormone on lumbar motoneurons of the rat isolated spinal cord. *Eur J Neurosci* **5**: 1360-1369.

Fitzgerald M (1985). The post-natal development of cutaneous afferent fibre input and receptive field organization in the rat dorsal hord. *J Physiol* **364**: 1-18.

Fitzgerald M, Butcher T, Shortland P (1994). Developmental changes in the laminar termination of A fibre cutaneous sensory afferents in the rat spinal cord dorsal horn. *J Comp Neurol* **348**: 225-233.

Fitzgerald M, Gibson S (1984). The postnatal physiological and neurochemical development of peripheral sensory C fibres. *Neuroscience* **13**: 933-944.

Fitzgerald M, Jennings E (1999). The postnatal development of spinal sensory processing. *PNAS* **96**: 7719-7722.

Fitzgerald M, King AE, Thompson SW, Woolf CJ (1987). The postnatal development of the ventral root reflex in the rat; a comparative in vivo and in vitro study. *Neurosci Lett* **78**: 41-45.

Fitzgerald M, Reynolds ML, Benowitz LI (1991) GAP-43 expression in the developing rat lumbar spinal cord. *Neuroscience* **41**: 187-199.

Forsythe ID, Redman SJ (1988). The dependence of motoneurone membrane potential on extracellular ion concentrations studied in isolated rat spinal cord. *J Physiol* **404**: 83-99.

Fuentealba P, Timofeev I, Steriade M (2004). Prolonged hyperpolarizing potentials precede spindle oscillations in the thalamic reticular nucleus. *PNAS* **101**: 9816-9821.

Fulton BP, Walton K (1986). Electrophysiological properties of neonatal rat motoneurons studied in vitro. *J Physiol* **370**: 651-678.

Gao B, Ziskind-Conhaim L (1995). Development of glycine- and GABA-gated currents in rat spinal cord. *J Neurophys* **74**: 113-121.

Glover JC (2000). Development of specific connectivity between premotor neurons and motoneurons in the brain stem and spinal cord. *Physiol Rev* **80**: 615-647.

Gray MA, Winpenny JP, Porteous DJ, Dorin JR, Argent BE (1994). CFTR and calcium-activated chloride currents in pancreatic duct cells of a transgenic CF mouse. *Am J Physiol* **266**: C213-221.

Haller M, Mironov SL, Karschin A, Richter DW (2001). Dynamic activation of K_{ATP} channels in rhythmically active neurons. *J Physiol* **537**: 69-81.

Hamill OP, Marty A, Neher E, Sakmann B, Sigworth FJ (1981). Improved patch-clamp techniques for high-resolution current recording from cells and cell-free membrane patches. *Pflugers Arch* **391**: 85-100.

Hillman DE (1979). Neuronal shape parameters and substructures as a basis of neuronal form. In: Schmitt F (eds). *The neurosciences fourth study program.* Cambridge, MA: MIT Press. p 477-498.

Hincke MT, Nairn AC, Staines WA (1995). Cystic fibrosis transmembrane conductance regulator is found within brain ventricular epithelium and choroid plexus. *J Neurochem* **64**: 1662-1668.

Hines ML, Carnevale NT (1997). The NEURON simulation environment. *Neural Comput* **9**:1179-1209.

Hubner CA, Stein V, Hermans-Borgmeyer I, Meyer T, Ballanyi K, Jentsch TJ (2001). Disruption of KCC2 reveals an essential role of K^+-Cl^- cotransport already in early synaptic inhibition. *Neuron* **30**: 515-524.

Hultborn H (2006). Spinal reflexes, mechanisms and concepts: From Eccles to Lundberg and beyond. *Prog Neurobiol* **78**: 215-232.

Jankowska E (2001). Spinal interneuronal systems: identification, multifunctional character and reconfigurations in mammals. *J Physiol* **533**: 31-40.

Jentsch TJ, Stein V, Weinreich F, Zdebik AA (2002). Molecular structure and physiological function of chloride channels. *Physiol Rev* **82**: 503-568.

Jessell TM (2000). Neuronal specification in the spinal cord: inductive signals and transcriptional codes. *Nat Rev Genet* **1**: 20–29.

Johansson S, Druzin M, Haage D, Wang MD (2001). The functional role of a bicuculline-sensitive Ca^{2+}-activated K^+ current in rat medial preoptic neurons. *J Physiol* **532**: 625-635.

Johnson SW, Seutin V (1997) Bicuculline methiodide potentiates NMDA-dependent burst firing in rat dopamine neurons by blocking apamin-sensitive Ca^{2+}-activated K^+ currents. *Neurosci Lett* **231**: 13-16.

Kandel ER, Schwartz JH, Jessell TM (2000). Movement. In: Kandel ER (eds). *Principles of neural science*. New York McGraw-Hill, p. 653-873.

Kellerth JO, Berthold CH, Conradi S (1979). Electron microscopic studies of serially sectioned cat spinal alpha-motoneurons. III. Motoneurons innervating fast-twitch (type FR) units of the gastrocnemius muscle. *J Comp Neurol* **184**: 755-767.

Kerai B, Greensmith L, Vrbova G, Navarrete R (1995). Effect of transient neonatal muscle paralysis on the growth of soleus motoneurons in the rat. *Dev Brain Res* **85**: 89-95.

Kerkut GA, Bagust J (1995). The isolated mammalian spinal cord. *Prog Neurobiol* **46**: 1-48.

Kernell D, Zwaagstra B (1989). Dendrites of cat's spinal motoneurones: relationship between stem diameter and predicted input conductance. *J Physiol* **413**: 255-269.

Kiddie G, McLean D, Van Ooyen A, Graham B (2005). Biologically plausible models of neurite outgrowth. *Prog Brain Res* **147**: 67-80.

Kiehn O (2006). Locomotor circuits in the Mammalian spinal cord. *Annu Rev Neurosci* **29**:279-306.

Kiehn O, Butt SJ (2003). Physiological, anatomical and genetic identification of CPG neurons in the developing mammalian spinal cord. *Prog Neurobiol* **70**:347-361.

Kjaerulff O, Barajon I, Kiehn O (1994). Sulphorhodamine-labelled cells in the neonatal rat spinal cord following chemically induced locomotor activity in vitro. *J Physiol* **478**: 265–273.

Kjaerulff O, Kiehn O (1996). Distribution of networks generating and coordinating locomotor activity in the neonatal rat spinal cord in vitro: a lesion study. *J Neurosci* **16**: 5777-5794.

Kobbert C, Thanos S.(2000). Topographic representation of the sciatic nerve motor neurons in the spinal cord of the adult rat correlates to region-specific activation patterns of microglia. *J Neurocytol* **29**: 271-283.

Koo SJ, Pfaff SL (2002). Fine-Tuning Motor Neuron Properties: Signaling from the Periphery. *Neuron* **35**: 823-826.

Kremer E, Lev-Tov A (1998). GABA-receptor-independent dorsal root afferents depolarization in the neonatal rat spinal cord. *J Neurophysiol* **79**: 2581-2592.

Kudo N, Nishimaru H (1998). Reorganization of locomotor activity during development in the prenatal rat. *Ann N Y Acad Sci* **860**: 306-317.

Kudo N, Yamada T (1985). Development of monosynaptic stretch reflex in the rat: an *in vitro* study. *J Physiol.* **369**: 127-144.

Kudo N, Yamada T (1987). Morphological and physiological studies of development of the monosynaptic reflexes in the rat lumbar spinal cord. *J Physiol* **389**: 441-459.

Kullander K, Butt SJ, Lebret JM, Lundfald L, Restrepo CE, Rydstrom A, Klein R, Kiehn O. Role of EphA4 and EphrinB3 in local neuronal circuits that control walking. *Science* **299**: 1889-1892.

Larkum ME, Launey T, Dityatev A, Luscher HR (1998). Integration of excitatory postsynaptic potentials in dendrites of motoneurons of rat spinal cord slice cultures. *J Neurophysiol* **80**: 924-935.

Levinsson A, Holmberg H, Broman J, Zhang M, Schouenborg J (2002). Spinal sensorimotor transformation: relation between cutaneous somatotopy and a reflex network. *J Neurosci* **22**: 8170–8182.

Lev-Tov A, Miller JP, Burke RE, Rall W (1983). Factors that control amplitude of EPSPs in dendritic neurons. *J Neurophysiol* **50**: 399-412.

Lev-Tov A, Pinco M (1992). In vitro studies of prolonged synaptic depression in the neonatal rat spinal cord. *J Physiol* **447**: 149-169.

Lewis MJ, Lewis EH III, Amos JA, Tsongalis GJ (2003). Cystic fibrosis. *Am J Clin Pathol* **120**: S3-13.

Li Y, Brewer D, Burke RE, Ascoli GA (2005). Developmental changes in spinal motoneuron dendrites in neonatal mice. *J Comp Neurol* **483**:304-317.

Light AR (1988). Normal anatomy and physiology of the spinal cord dorsal horn. *Appl Neurophysiol* **51**: 78-88.

Lowrie M, Lawson SJ (2000). Cell death of spinal interneurons. *Prog Neurobiol* **61**: 543-555.

Lüscher HR, Clamann HP (1992). Relation between structure and function in information transfer in spinal monosynaptic reflex. *Physiol Rev* **72**, 71-99.

Lüscher HR, Larkum ME (1998). Modeling action potential initiation and back-propagation in dendrites of cultured rat motoneurons. *J Neurophysiol* **80**, 715-729.

Ma T, Thiagarajah JR, Yang H, Sonawane ND, Folli C, Galietta LJ, Verkman AS (2002). Thiazolidinone CFTR inhibitor identified by high-throughput screening blocks cholera toxin-induced intestinal fluid secretion. *J Clin Invest* **110**: 1651-1658.

Mainen ZF, Joerges J, Huguenard JR, Sejnowski TJ (1995) A model of spike initiation in neocortical pyramidal neurons. *Neuron* **15**: 1427-1439.

Mann D (2006). Peripheral nerves. In: *The nervous system in action.* http://www.unmc.edu/Physiology/Mann/index.html.

Marchetti C, Beato M, Nistri A (2001a). Alternative rhythmic activity induced by dorsal root stimulation in the neonatal rat spinal cord *in vitro*. *J Physiol* **530**: 105-112.

Marchetti C, Beato M, Nistri A (2001b). Evidence for increased extracellular K^+ as an important mechanism for dorsal root induced alternating rhythmic activity in the neonatal rat spinal cord in vitro. *Neurosci Lett* **304**: 77-80.

Marchetti C, Pagnotta S, Donato R, Nistri A (2002). Inhibition of spinal or hypoglossal motoneurons of the newborn rat by glycine or GABA. *Eur J Neurosci* **15**: 975-983.

Marchetti C, Taccola G, Nistri A (2005). Activation of group I metabotropic glutamate receptors depresses recurrent inhibition of motoneurons in the neonatal rat spinal cord in vitro. *Exp Brain Res* **164**: 406-410.

Martin AR, Wallace BG, Fuchs PA, Nicholls JG (2001). Cellular mechanisms of motor control. In: Nicholls JG (eds). *From neuron to brain.* Sunderland, MA Sinauer Associates, p.447-479.

Martinez de Arrieta C, Koibuchi N, Chin WW (2000). Coactivator and corepressor gene expression in rat cerebellum during postnatal development and the effect of altered thyroid status. *Endocrinology* **141**: 1693-1698.

Mentis GZ, Alvarez FJ, Bonnot A, Richards DS, Gonzalez-Forero D, Zerda R, O'Donovan MJ (2005). Noncholinergic excitatory actions of motoneurons in the neonatal mammalian spinal cord. *PNAS* **102**: 7344-7349.

Minami K, Miki T, Kadowaki T, Seino S (2004). Roles of ATP-sensitive K^+ channels as metabolic sensors: studies of Kir6.x null mice. *Diabetes* ***53***: S176-180.

Mirnics K, Koerber HR (1995a). Prenatal development of rat primary afferent fibers: I. Peripheral projections. *J Comp Neurol* ***355***: 589-600.

Mirnics K, Koerber HR (1995b). Prenatal development of rat primary afferent fibers: II. Central projections. *J Comp Neurol* ***355***: 601-614.

Mironov SL, Langohr K, Haller M, Richter DW (1998). Hypoxia activates ATP-dependent potassium channels in inspiratory neurones of neonatal mice. *J Physiol* **509**: 755-766.

Molander C, Xu Q, Grant G (1984). The cytoarchitectonic organization of the spinal cord in the rat. I. The lower thoracic and lumbosacral cord. *J Comp Neurosci* ***230***: 133-141.

Mori S, Stuart DG, Wiesendanger M (2004). *Brain mechanisms for the integration of posture and movement.* Amsterdam Elsevier.

Mulberg AE, Resta LP, Wiedner EB, Altschuler SM, Jefferson DM, Broussard DL (1995) Expression and localization of the cystic fibrosis transmembrane conductance regulator mRNA and its protein in rat brain. *J Clin Invest* **96**: 646-652.

Mulberg AE, Wiedner EB, Bao X, Marshall J, Jefferson DM, Altschuler SM (1994). Cystic fibrosis transmembrane conductance regulator protein expression in brain. *Neuroreport* ***5***: 1684-1688.

Nakayama K, Nishimaru H, Kudo N (2002). Basis of changes in left-right coordination of rhythmic motor activity during development in the rat spinal cord. *J Neurosci* ***22***: 10388-10398.

Nichols CG (2006). K_{ATP} channels as molecular sensors of cellular metabolism. *Nature* **440**: 470-476.

Nicolopoulos-Stournaras S, Iles JF (1983). Motor neuron columns in the lumbar spinal cord of the rat. *J Comp Neurol* **217**: 75-85.

Nilius B, Droogmans G (2003). Amazing *chloride* channels: an overview. *Acta Physiol Scand* **177**: 119-147.

Nishimaru H, Iizuka M, Ozaki S, Kudo N (1996). Spontaneous motoneuronal activity mediated by glycine and GABA in the spinal cord of rat fetuses in vitro. *J Physiol* **497**: 131-143.

Nishimaru H, Kudo N (2000). Formation of the central pattern generator for locomotion in the rat and mouse. *Br Res Bull* **53**: 661-669

Nishimaru H, Restrepo CE, Ryge J, Yanagawa Y, Kiehn O (2005). Mammalian motor neurons corelease glutamate and acetylcholine at central synapses. *PNAS* **102**: 5245-5249.

Nistri A, Ostroumov K, Sharifullina E, Taccola G (2006). Tuning and playing a motor rhythm: how metabotropic glutamate receptors orchestrate generation of motor patterns in the mammalian central nervous system. *J Physiol* **572**: 323-334.

Nornes HO, Das GD (1972). Temporal pattern of neurogenesis in spinal cord: cytoarchitecture and directed growth of axons. *PNAS* **69**: 1962-1966.

Nornes HO, Das GD (1974). Temporal pattern of neurogenesis in spinal cord of rat. I. An autoradiographic study--time and sites of origin and migration and settling patterns of neuroblasts. *Brain Res* **73**, 121-138.

Oppenheim RW (1986). The absence of significant postnatal motoneuron death in the brachial and lumbar spinal cord of the rat. *J Comp Neurol* **246**, 281-286.

Oppenheim RW (1991). Cell death during development of the nervous system. *Annu Rev Neurosci* **14**, 453-501.

Orlovsky GN, Deliagina TG, Grillner S (1999). *Neuronal control of locomotion: from mollusc to man.* Oxford Oxford University Press.

Payne JA, Rivera C, Voipio J, Kaila K (2003). Cation-chloride co-transporters in neuronal communication, development and trauma. *Trends Neurosci* **26**: 199-206.

Pearson K (2000). Motor systems. *Curr Opin Neurobiol* **10**: 649-654.

Peyronnard JM, Charron L (1983). Motoneuronal and motor axonal innervation in the rat hindlimb: a comparative study using horseradish peroxidase. *Exp Brain Res* **50**: 125-132.

Pier GB, Grout M, Zaidi TS (1997). Cystic fibrosis transmembrane conductance regulator is an epithelial cell receptor for clearance of Pseudomonas aeruginosa from the lung. *PNAS* **94**: 12088-12093.

Pierrefiche O, Bischoff AM, Richter DW (1996). ATP-sensitive K^+ channels are functional in expiratory neurones of normoxic cats. *J Physiol* **494**: 399-409.

Pricea SR, Briscoe J (2004). The generation and diversification of spinal motor neurons: signals and responses. *Mec Dev* **121**: 1103-1115.

Prochazka A, Clarac F, Loeb GE, Rothwell JC, Wolpaw JR (2000). What do reflex and voluntary mean? Modern views on an ancient debate. *Exp Brain Res* **130**: 417-432.

Rexed B (1952). The cytoarchitectonic organization of the spinal cord in the cat. *J Comp Neurol* **96**: 415-496.

Rivera C, Voipio J, Kaila K (2005). Two developmental switches in GABAergic signalling: the K^+-Cl^- cotransporter KCC2 and carbonic anhydrase CAVII. *J Physiol* **562**: 27-36.

Rivero-Melian C (1996). Organization of hindlimb nerve projections to the rat spinal cord: a choleragenoid horseradish peroxidase study. *J Comp Neurol* **364**: 651-663.

Rose PK, Dagum A (1988). Nonequivalent cylinder models of neurons: interpretation of voltage transients generated by somatic current injection. *J Neurophysiol* **60**: 125-148.

Rozzo A, Ballerini L, Abbate G, Nistri A (2002). Experimental and modeling studies of novel bursts induced by blocking Na^+ pump and synaptic inhibition in the rat spinal cord. *J Neurophysiol.* 2002 Aug;88(2):676-91.

Rudomin P (1999). Presynaptic selection of afferent inflow in the spinal cord. *J Physiol Paris* **93**: 329-347.

Rudomin P (2002). Selectivity of the central control of sensory information in the mammalian spinal cord. *Adv Exp Med Biol* **508**: 157-170.

Safronov BV, Vogel W (1995). Single voltage-activated Na^+ and K^+ channels in the somata of rat motoneurones. *J Physiol* **487**: 91-106.

Safronov BV, Wolff M, Vogel W (2000) Excitability of the soma in central nervous system neurons. *Biophys J* **78**: 2998-3010.

Saito K (1979). Development of spinal reflexes in the rat fetus studied in vitro. *J Physiol* **294**: 581-594.

Sanes J, Lichtman JW (1999). Development of the vertebrate neuromuscular junction. *Annu Rev Neurosci* **22**: 389-442.

Schultz BD, Singh AK, Devor DC, Bridges RJ (1999). Pharmacology of CFTR chloride channel activity. *Physiol Rev* **79**: S109-S144.

Segev I, London M (2000). Untangling dendrites with quantitative models. *Science* **290**: 744-750.

Sharifullina E, Ostroumov K, Nistri A (2005). Metabotropic glutamate receptor activity induces a novel oscillatory pattern in neonatal rat hypoglossal motoneurones. *J Physiol* **563,** 139-159.

Sheppard DN, Gray MA, Gong X, Sohma Y, Kogan I, Benos DJ, Scott-Ward TS, Chen JH, Li H, Cai Z, Gupta J, Li C, Ramjeesingh M, Berdiev BK, Ismailov II, Bear CE, Hwang TC, Linsdell P, Hug MJ (2004). The patch-clamp and planar lipid bilayer techniques: powerful and versatile tools to investigate the CFTR Cl- channel. *J Cyst Fibros* Suppl **2**:101-108.

Sheppard DN, Welsh MJ (1992). Effect of ATP-sensitive K^+ channel regulators on cystic fibrosis transmembrane conductance regulator chloride currents. *J Gen Physiol* **100**: 573-591.

Sheppard DN, Welsh MJ (1999). Structure and function of the CFTR chloride channel. *Physiol Rev* **79**: S23-S45.

Sherrington C (1906). *The Integrative Action of the Nervous System.* Cambridge University Press (5th ed. 1947), p. 433.

Shik ML, Orlovksy GN (1976). Neurophysiology of locomotor automatism. *Phys Rev* **56**: 465-501.

Shumaker H, Soleimani M (1999). CFTR upregulates the expression of the basolateral Na^+-K^+-2Cl^- cotransporter in cultured pancreatic duct cells. *Am J Physiol* **277**: C1100-1110.

Silos-Santiago I, Jeng B, Snider WD (1995). Sensory afferents show appropriate somatotopy at the earliest stage of projection to dorsal horn. *Neuroreport* **6**: 861-865.

Silos-Santiago I, Snider WD (1992). Development of commissural neurons in the embryonic rat spinal cord. *J Comp Neurol* **325**: 514-526.

Silos-Santiago I, Snider WD (1994). Development of interneurons with ipsilateral projections in embryonic rat spinal cord. *J Comp Neurol* **342**: 221-231.

Snider WD, Zhang L, Yusoof S, Gorukanti N, Tsering C (1992). Interactions between dorsal root axons and their target motor neurons in developing mammalian spinal cord. *J Neurosci* **2**:3494-3508.

Stein V, Hermans-Borgmeyer I, Jentsch TJ, Hubner CA (2004). Expression of the K^+Cl^- cotransporter KCC2 parallels neuronal maturation and the emergence of low intracellular chloride. *J Comp Neurol* **468**: 57-64.

Szucs P, Odeh F, Szokol K, Antal M (2003). Neurons with distinctive firing patterns, morphology and distribution in laminae V-VII of the neonatal rat lumbar spinal cord. *Eur J Neurosci* **17**: 537-544.

Tabak J, Rinzel J, O'Donovan MJ (2001). The role of activity-dependent network depression in the expression and self-regulation of spontaneous activity in the developing spinal cord. *J Neurosci* **21**: 8966-8978.

Tabak J, Senn W, O'Donovan MJ, Rinzel J (2000). Modeling of spontaneous activity in developing spinal cord using activity-dependent depression in an excitatory network. *J Neurosci* **20**: 3041-3056.

Taccola G, Nistri A (2004). Low micromolar concentrations of 4-aminopyridine facilitate fictive locomotion expressed by the rat spinal cord in vitro. *Neuroscience* **126**: 511-520.

Taccola G, Nistri A (2006). Fictive locomotor patterns generated by tetraethylammonium application to the neonatal rat spinal cord in vitro. *Neuroscience* **137**: 659-670.

Takahashi T (1990). Membrane currents in visually identified motoneurones of neonatal rat spinal cord. *J Physiol* **423**: 27-46.

Tarasov A, Dusonchet J, Ashcroft F (2004). Metabolic regulation of the pancreatic beta-cell ATP-sensitive K+ channel: a *pas de deux*. *Diabetes* **53**: S113-122

Thiagarajah JR, Song Y, Haggie PM, Verkman AS (2004). A small molecule CFTR inhibitor produces cystic fibrosis-like submucosal gland fluid secretions in normal airways. *FASEB J* **18**: 875-877.

Thompson WJ, Soileau LC, Balice-Gordon RJ, Sutton LA (1987). Selective innervation of types of fibres in developing rat muscle. *J Exp Biol* **132**: 249-263.

Thomzig A, Laube G, Pruss H, Veh RW (2005). Pore-forming subunits of K-ATP channels, Kir6.1 and Kir6.2, display prominent differences in regional and cellular distribution in the rat brain. *J Comp Neurol*, **484**: 313-330.

Thurbon D, Luscher HR, Hofstetter T, Redman SJ (1998). Passive electrical properties of ventral horn neurons in rat spinal cord slices. *J Neurophysiol* **80**, 2485-2502.

Tran TS, Phelps PE (2000). Axons crossing in the ventral commissure express L1 and GAD65 in the developing rat spinal cord. *Dev Neurosci* **22**: 228-236.

Ueno T, Okabe A, Akaike N, Fukuda A, Nabekura J (2002). Diversity of neuron-specific K^+-Cl^- cotransporter expression and inhibitory postsynaptic potential depression in rat motoneurons. *J Biol Chem* **277**: 4945-4950.

Ulrich D, Quadroni R, Luscher HR (1994). Electronic structure of motoneurons in spinal cord slice cultures: a comparison of compartmental and equivalent cylinder models. *J Neurophysiol* **72**: 861-871.

van der Laan S, Lachize SB, Schouten TG, Vreugdenhil E, de Kloet ER, Meijer OC (2005). Neuroanatomical distribution and colocalisation of nuclear receptor corepressor (N-CoR) and silencing mediator of retinoid and thyroid receptors (SMRT) in rat brain. *Brain Res* **1059**: 113-121.

Vervaeke K, Hu H, Graham LJ, Storm JF (2006) Contrasting effects of the persistent Na^+ current on neuronal excitability and spike timing. *Neuron* **49**: 257-270.

Vinay L, Brocard F & Clarac F (2000). Differential maturation of motoneurons innervating ankle flexor and extensor muscles in the neonatal rat. *Eur J Neurosci* **12**, 4562-4566.

Vinay L, Brocard F, Fellippa-Marques S, Clarac F (1999). Antidromic discharges of dorsal root afferents in the neonatal rat. *J Physiol Paris* **93**: 359-367.

Westbury DR (1982). A comparison of the structures of alpha and gamma-spinal motoneurones of the cat. *J Physiol* **325**, 79-91.

Westerga J, Gramsbergen A (1992). Structural changes of the soleus and the tibialis anterior motoneuron pool during development in the rat. *J Comp Neurol* **319**, 406-416.

Weyler RT, Yurko-Mauro KA, Rubenstein R, Kollen WJ, Reenstra W, Altschuler SM, Egan M, Mulberg AE (1999). CFTR is functionally active in GnRH-expressing GT1-7 hypothalamic neurons. *Am J Physiol* **277**: C563-C571.

Windhorst U (1996). On the role of recurrent inhibitory feedback in motor control. *Prog Neurobiol* **49**: 517-587.

Wright AM, Gong X, Verdon B, Linsdell P, Mehta A, Riordan JR, Argent BE, Gray MA (2004). Novel regulation of cystic fibrosis transmembrane conductance regulator (CFTR) channel gating by external chloride. *J Biol Chem.* **279**: 41658-41663.

Wu WL, Ziskind-Conhaim L, Sweet MA (1992). Early development of glycine- and GABA-mediated synapses in rat spinal cord. *J Neurosci* **12**: 3935-3945.

Yamada K, Inagaki N (2002). ATP-sensitive K^+ channels in the brain: sensors of hypoxic conditions. *News Physiol Sci* **17**: 127-130.

Yamada K, Inagaki N (2005). Neuroprotection by K_{ATP} channels. *J Mol Cell Cardiol* **38**: 945-949.

Yamada K, Ji JJ, Yuan H, Miki T, Sato S, Horimoto N, Shimizu T, Seino S, Inagaki N (2001). Protective role of ATP-sensitive potassium channels in hypoxia-induced generalized seizure. *Science* **292**: 1543-1546.

Yamada K, Ji JJ, Yuan H, Miki T, Sato S, Horimoto N, Shimizu T, Seino S, Inagaki N (2001). Protective role of ATP-sensitive potassium channels in hypoxia-induced generalized seizure. *Science* **292**: 1543-1546.